



Master's thesis

# Fabrication and Characterization of a Dimer Josephson Junction Array Amplifier

Desislava Gancheva Atanasova

November 27, 2020

Supervised by **Univ.-Prof. Dr. Gerhard Kirchmair**

Institute of Experimental Physics

Faculty of Mathematics, Computer Science and Physics

University of Innsbruck

Austria



## Abstract

Reading out the state of a qubit faster than its decay time is crucial for reliable quantum information processing while avoiding errors. Parametric amplifiers allow single-shot measurements making them an indispensable tool in superconducting circuit architectures. This thesis provides a comprehensive theoretical explanation of the general principles of parametric amplification and introduces a special type of non-degenerate amplifiers based on long dispersion engineered Josephson junction arrays called Dimer Josephson Junction Array Amplifiers (DJJAAs). With the aid of superconducting quantum interference devices (SQUIDs) their resonant frequencies can be tuned. The long chains create multiple modes which further enhance the working range of these amplifiers.

A recipe for a standard two-step photolithography process has been developed from scratch and utilized for the in-house fabrication of the amplifiers. Two devices are assembled and fully characterized. Combining the observed flux tunability of 1.6 GHz and the multiple tunable eigenmodes where amplification has been demonstrated, these amplifiers have the potential to cover the entire frequency band between 1 – 12 GHz. The measured bandwidth of up to 13 MHz for 20 dB allows fast operation. With its high dynamic range reaching nearly  $-100$  dBm, the amplifier proves its robustness regarding strong signals. Moreover, for a moderate gain of 20 dB the measured added noise close to the quantum limit, between 1.25 and 4 photons per unit bandwidth, outperforms any available commercial cryogenic semiconductor amplifier.



# Contents

<b>1</b>	<b>Introduction</b>	<b>3</b>
<b>2</b>	<b>Concepts</b>	<b>5</b>
2.1	Principles of quantum-limited parametric amplification . . . . .	5
2.1.1	Parametric amplifier classification . . . . .	6
2.1.2	Quantum limit of noise . . . . .	8
2.2	Superconducting quantum circuits . . . . .	10
2.2.1	LC oscillator . . . . .	11
2.2.2	Josephson junction . . . . .	12
2.3	Input-Output Theory . . . . .	17
2.3.1	Driven coupled non-linear resonators: Bose-Hubbard dimer . . . . .	19
2.4	Dimer Josephson Junction Array Amplifier (DJJAA) . . . . .	22
2.4.1	Josephson junction arrays (JJAs) . . . . .	23
2.4.2	Dispersion engineering: Coupled JJAs . . . . .	27
<b>3</b>	<b>Fabrication</b>	<b>31</b>
3.1	Optical lithography . . . . .	31
3.2	Lift-off . . . . .	33
3.3	Amplifier fabrication . . . . .	33
3.3.1	Design considerations and fabrication calibrations . . . . .	35
3.4	Troubleshooting . . . . .	39
<b>4</b>	<b>Experiment</b>	<b>43</b>
4.1	Devices, sample holder and PCB . . . . .	43
4.2	Setup . . . . .	44
4.2.1	Noise characterization . . . . .	46
4.3	Calibrations . . . . .	48
<b>5</b>	<b>Experimental results</b>	<b>51</b>
5.1	Tunability . . . . .	51
5.1.1	Mode tunability through magnetic flux . . . . .	51
5.1.2	Amplification tunability . . . . .	52
5.2	Gain map . . . . .	54
5.3	Gain-Bandwidth Product . . . . .	55
5.4	1-dB compression point . . . . .	56
5.5	Noise performance . . . . .	58
5.5.1	Noise visibility ratio . . . . .	58
5.5.2	Added photon number . . . . .	59
5.6	Pump cancellation . . . . .	61

---

5.7 Attenuator heating . . . . .	62
<b>6 Conclusions and outlook</b>	<b>65</b>
References . . . . .	67
<b>A Method of nodes</b>	<b>73</b>
<b>B Kerr coefficients</b>	<b>77</b>
<b>C Final recipes for DJJAA fabrication</b>	<b>79</b>
<b>D Setup details</b>	<b>83</b>
<b>E Nyquist model: semi-infinite transmission line</b>	<b>87</b>
<b>F Additional plots</b>	<b>91</b>

# List of Figures

2.1.1	Basic operational principle of an amplifier . . . . .	5
2.1.2	Wave mixing . . . . .	7
2.1.3	Examples of different parametric amplification . . . . .	7
2.1.4	Phase-space representation of phase-sensitive and phase-insensitive amplification schemes . . . . .	9
2.2.1	LC oscillator . . . . .	11
2.2.2	Josephson junction: Illustration and images . . . . .	13
2.2.3	Josephson junction: Lumped-element representation and energy spectrum . . . . .	14
2.2.4	DC-SQUID . . . . .	15
2.3.1	Input-Output theory: system sketch . . . . .	18
2.3.2	Optical representation of two coupled anharmonic resonators . . . . .	20
2.3.3	Phase diagram of driven coupled non-linear resonators for $J = 0.7\kappa$ and $U < 0$ . . . . .	21
2.3.4	Energy level scheme under continuous monochromatic drive . . . . .	22
2.4.1	Josephson junction array: Lumped-element representation . . . . .	23
2.4.2	Standing-wave pattern and dispersion relation for a Josephson junction array with $N = 800$ . . . . .	25
2.4.3	Dispersion engineered Josephson junction arrays . . . . .	27
2.4.4	Standing-wave pattern and dispersion relation for a dimer Josephson junction array with $N = 800$ . . . . .	29
3.1.1	Optical lithography with positive resist . . . . .	32
3.1.2	Resist with undercut profile: expectations vs. reality . . . . .	32
3.2.1	Lift-off . . . . .	33
3.3.1	Schematic of a simplified two-step process for Al/ $\text{AlO}_x$ /Al junction fabrication . . . . .	34
3.3.2	Finished amplifier device with $N = 1800$ fabricated on silicon in QNTZ . . . . .	35
3.3.3	Argon milling calibration . . . . .	37
3.3.4	Critical current density calibration . . . . .	38
3.3.5	Junction aging . . . . .	38
3.4.1	Sticking problems . . . . .	39
3.4.2	Resist profiles with different pretreatments . . . . .	40
3.4.3	SEM images of samples with wrong and right resists profiles . . . . .	41
4.1.1	Assembled amplifiers . . . . .	44
4.2.1	Schematic of the measurement setup . . . . .	45
4.2.2	Two-stage amplification chain . . . . .	48
4.3.1	Output characterization . . . . .	48
4.3.2	Line attenuation . . . . .	49

5.1.1	Flux maps . . . . .	52
5.1.2	DJJAA1: Flux tunability . . . . .	53
5.1.3	DJJAA2: Gain at the sweet spot of different dimers . . . . .	53
5.2.1	DJJAA1: Non-degenerate gain map at $I_{coil} = 0$ mA . . . . .	54
5.3.1	DJJAA1: Gain-bandwidth product for three flux-bias points . . . . .	56
5.4.1	DJJAA1: Saturation power . . . . .	57
5.5.1	DJJAA1: Noise visibility ratio . . . . .	59
5.5.2	Raw data for noise measurements . . . . .	60
5.5.3	DJJAA1: Added photon number at different flux-bias points . . . . .	60
5.5.4	DJJAA2: Added photon number at the sweet spots of different dimers. . . . .	61
5.6.1	DJJAA2: Comparison of the added photon number of the first dimer with and without pump cancellation . . . . .	62
5.7.1	Heating effects . . . . .	63
A.1.1	Branch and node representation . . . . .	73
A.1.2	Josephson junction array with $N = 3$ : Lumped-element representation . . . . .	76
D.1.1	Setup pictures . . . . .	83
D.1.2	Dilution refrigerator . . . . .	84
D.1.3	SolidWorks drawing of the sample holder . . . . .	84
D.1.4	SolidWorks drawing of the coil body . . . . .	85
E.1.1	Generalized Nyquist noise . . . . .	88
F.1.1	Flux maps in magnitude . . . . .	91
F.1.2	DJJAA1: Frequency maps of the gain for $I_{coil} = 0$ mA . . . . .	92
F.1.3	DJJAA2: Added photon number at the sweet spots of dimer 4 . . . . .	92



# Chapter 1

## Introduction

The idea for a quantum computer promising superiority over its classical counterpart dates back to 1982[1]. With the effort of many scientists in the past several decades the final goal of realizing such a machinery becomes feasible. Due to the recent developments in the field[2], superconducting circuits were established as one of the most prominent platforms for constructing a real multi-qubit quantum processor. Compared to other platforms employing microscopic systems, such as ultracold atoms and trapped ions, which rely on encoding the information in the naturally available energy levels, superconducting qubits are macroscopic and easily tailored to the needs of the experiment. Circuit Quantum ElectroDynamics (circuit QED), a study based on cavity quantum electrodynamics, was developed to describe the interaction of these so-called *artificial atoms* with quantized electromagnetic fields in the radio frequency domain.

However, due to the low energies of the microwave photons, their detection is a complicated task. Many strove towards creating a photon multiplier[3], while others focused on frequency conversion to the optical domain[4] but generally the preferred solution remains the use of amplifiers. Any device introduced on the readout chain inevitably adds noise, thus deteriorating the Signal-to-Noise Ratio (SNR). Although low-noise commercial cryogenic amplifiers exist, they add noise which is far bigger than the usual signal power, requiring averaging over several instances to allow extracting the information encoded in the qubit. The noise floor is determined by the first amplification stage, meaning that we need the first amplifier to add virtually close to no noise. Fortunately, superconducting parametric amplifiers have the potential to amplify without adding any noise[5], thus successfully conquering the limitation on the signal-to-noise ratio.

These amplifiers rely on their intrinsic non-linearity which under the influence of a strong pump transfers energy to the signal via wave-mixing. Generally, parametric amplifiers (paramps) are split in two types depending whether the non-linear elements are embedded in a resonator or a transmission line. The former amplify within a close vicinity of the eigenfrequency of the circuit with typical representatives being Josephson Parametric Amplifiers (JPAs)[6, 7, 8, 9], Josephson Parametric Converters (JPCs)[10] and Josephson Bifurcation Amplifiers (JBAs)[11, 12]. The later instead is the microwave analogue of optical fibre amplifiers[13] where the tones interact along the transmission line resulting in a much larger bandwidth usually covering several gigahertz. Those amplifiers are usually referred to as Traveling Wave Parametric Amplifiers (TWPAs) and there are many different ways to realize them[14, 15, 16, 17].

The amplifier presented in this thesis is a standing-wave paramp based on long chains of Superconducting Interference QUantum Devices (SQUIDs) dispersion engineered

by placing a capacitor in the center. As a consequence the pairs of modes hybridize into doublets, denoted dimers, suitable for non-degenerate as well as degenerate amplification. The advantages of this amplifier come from the large working range relying on multiple modes which are flux-tunable in frequency, as well as its high saturation power due to the use of long arrays. This device is called Dimer Josephson Junction Array Amplifier, or shortly DJJAA, and was first realized in Karlsruhe by P. Winkel and I. Takmakov[18, 19] inspired by the pioneering work of C. Eichler[20]. The design was also kindly provided by the developers and completely adopted with small changes to fit the in-house fabrication specifics.

This thesis is split in four main parts. Chapter 2 introduces the fundamentals of parametric amplification needed for the understanding of the subjects later discussed in this thesis. Once the basic building blocks of circuit QED are presented, the chapter continues with input-output theory, a useful tool for predicting the behaviour of any amplifier, including the Josephson Parametric Dimer, reviewed in the same section. Furthermore, the whole concept of Josephson junction arrays is unraveled together with some details on dispersion engineering. Half of the time spent on this work was dedicated on getting the two-step optical lithography process running in the clean room facility of the Quantum-Nano-Zentrum Tirol (QNZT), which is also the topic of Chapter 3. In Chapter 4, a brief overview on the experimental apparatus is given including some calibrations. The results from the detailed characterization of the amplifier are reported in Chapter 5, together with a comprehensive discussion. Naturally, a conclusion and an outlook follow the four main parts. For additional information the reader can refer to the appendices.

# Chapter 2

## Concepts

This chapter contains an introduction on the main concepts of parametric amplification. Starting from the basic building blocks in circuit QED which are used throughout the thesis, we focus on more relevant aspects to the DJJAA, namely input-output theory and its implementation for dimer amplifiers. The theoretical model for Josephson junction arrays is derived and later used together with the dispersion-engineering to describe the device of interest.

### 2.1 Principles of quantum-limited parametric amplification

Generally, amplifiers are two-port devices that use a power source to produce at its output a version of the input signal with increased amplitude. The amount of this increase is called the gain. If the output power  $P_{out}(\omega)$  is proportional to the input  $P_{in}(\omega)$

$$P_{out}(\omega) = G(\omega)P_{in}(\omega) \quad (2.1.1)$$

the amplifiers is *linear*.

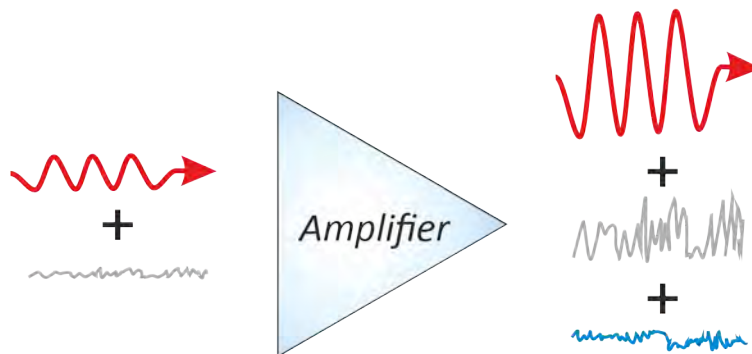


**Figure 2.1.1: Basic operation principle of an amplifier.** The signal (red) which also carries some noise (gray) is amplified by the device. Additionally, the amplifier deteriorates the signal by adding noise (blue).

Ideally, the amplifier is noiseless and has a gain which is time-stable and independent of the frequency and power of the input signal. In reality, the situation is generally different: the linear regime can break down due to the inherent non-linearity,

which is a trait of every amplifier; as seen in Eq. 2.1.1 the gain is frequency dependant; adding noise is inevitable, resulting in reduced signal-to-noise ratio (SNR). The conceptual drawing of a real device can be found in Fig. 2.1.1. A mix of coherent wave and noise associated with the impedance of the wave source at the input is equally amplified by the gain. Moreover, the device also adds noise. For a quantum-limited amplifier the amount of added noise is determined by Heisenberg uncertainty principle, this situation will be further discussed in Section 2.1.2.

Even linear amplifiers will start behaving non-linearly once a certain total power is exceeded. The linear regime determines the *dynamic range* of the device, while the onset of non-linear effects is marked by the *saturation power*, often characterized by its *1-dB compression point*. This point is defined as the signal power at which the maximum gain is reduced by one decibel. Another important parameter of an amplifier is its *instantaneous bandwidth*, usually referred as simply the device bandwidth. This bandwidth is determined by the frequency range where the gain doesn't drop more than three decibels below the maximum gain. The minimum required bandwidth in circuit QED equals the linewidth of the readout resonator, typically a few megahertz. In order to increase the working range of such a device satisfying just the minimum requirements, frequency tunability of the bandwidth is desired. The last two properties determine the total frequency working range of the device.

### 2.1.1 Parametric amplifier classification

The notion of *parametric interaction* as introduced in the field of optics[13] describes the interaction between waves passing through a nonlinear passive medium. Precisely, a strong coherent field (pump) modulates a parameter in the medium which stimulates the population of the system modes detuned from the pump. At microwave frequencies, the modulated parameter is the impedance of the circuit. The type of non-linearity determines the predominant frequency mixing process as shown in Fig. 2.1.2. Second-order nonlinearity  $\chi^{(2)}$  causes a pump photon with frequency  $\omega_p$  to split into a pair of signal  $\omega_s$  and idler  $\omega_i$  obeying the energy relation  $\omega_p = \omega_s + \omega_i$ . This process is called *three-wave mixing*. The third-order nonlinearity  $\chi^{(3)}$  governs the *four-wave mixing* process by converting two pump photons into signal and idler photons with the frequency matching condition  $2\omega_p = \omega_s + \omega_i$ . In order to enhance the process and limit its frequency range, similarly to lasers, the nonlinear medium is placed in a cavity. The conversion is stimulated by the existing fields, i.e. stimulated emission takes place, resulting in parametric amplification.

Once we introduced the phenomena behind amplification, we can proceed with further classification of the devices. While the literature[21, 22] is not completely consistent on the topic of degeneracy, the presented summary follows the definitions from [23, 24]. From this moment on, I will refer to degeneracy as either in space or frequency. *Spatial degeneracy* is regulated by the mode separation in a way that if each mode can be addressed via a separate port, the amplifier is spatially non-degenerate. This specific case is especially relevant for the Josephson Parametric Converter (JPC)[10], where pump, signal and idler are present at different ports. Otherwise, the device is spatially degenerate. Similarly for *frequency degeneracy*, amplifiers utilizing a single mode in frequency are called degenerate, while the amplifier is non-degenerate if two modes are employed.

Amplification schemes are *phase-insensitive* unless  $\omega_s \approx \omega_i$  within the detected band[6]. Phase sensitivity is determined by the response of the device to the input



**Figure 2.1.2: Wave mixing.** A schematic illustration of (a) three-wave mixing and (b) four-wave mixing. Pump photons (purple) are converted to a pair of signal (red) and idler (cyan) photons, obeying energy conservation laws. The phenomena are based on the different order nonlinearity of the medium, namely second order  $\chi^{(2)}$  and third order  $\chi^{(3)}$ , respectively for (a) and (b). If a signal is present at the input, the conversion results in signal amplification, while the excess energy is carried by the idler.

quadratures. A phase-sensitive amplifier treats the signal quadratures differently: one preferred quadrature is amplified while the other one is deamplified. In a phase-insensitive process both quadratures are equally amplified. Phase-sensitive amplification allows achieving interesting non-classical states (squeezed states[7, 25]) due to the interference between the signal and idler. To obtain more intuition about the possible types of amplification several examples are presented in Fig. 2.1.3. Without loss of generality, one can say that as long as the amplification is non-degenerate (right in Fig. 2.1.3), it is always phase-insensitive. If the amplification is degenerate, the phase-sensitivity is only manifested when the signal and idler are spaced within less than one detection bandwidth (left in Fig. 2.1.3). Otherwise, an idler component appears (middle in Fig. 2.1.3) and it carries at least the vacuum noise.

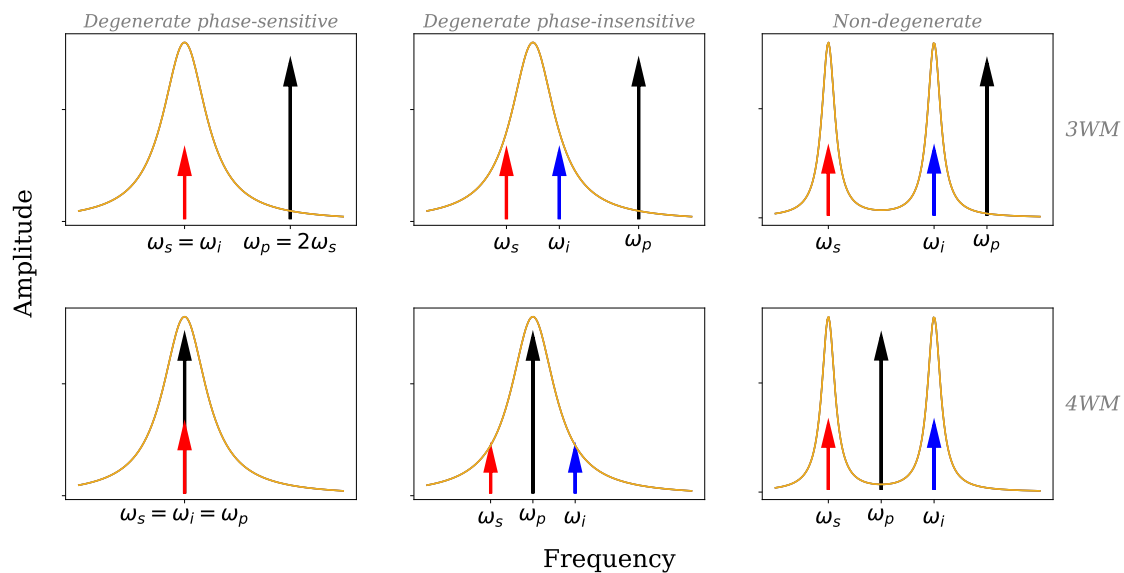


**Figure 2.1.3: Examples of different parametric amplification.** The figures consists of six separate plots, where the device response is colored in yellow, while the coherent tones are illustrated as arrows in black (pump), red (signal) and blue (idler). The first row always represents three-wave mixing (3WM) while the second - four-wave mixing (4WM). Split in columns, one can see configurations for degenerate phase-sensitive, degenerate phase-insensitive, and non-degenerate phase-insensitive amplification.

More thorough explanation is indeed required for phase sensitivity, since it directly influences the quantum limit of noise. For this purpose, the next part is dedicated to quantum limits on noise depending on the phase-sensitivity. It follows the treatment developed in the pioneering work of C. M. Caves [5].

### 2.1.2 Quantum limit of noise

Consider a single bosonic mode obeying the commutation relations  $[a, a^\dagger] = 1$ . The annihilation operator can be expressed as  $a = X_1 + iX_2$ , where  $X_{1,2}$  are the amplitudes of the mode quadratures oscillating  $90^\circ$  out of phase. They do not commute as  $[X_1, X_2] = i/2$ . The commutation relation imposes an uncertainty principle on the square root of the quadrature variances  $\Delta X_1 \Delta X_2 \geq \frac{1}{4}$  which translates into mean square fluctuations for the complex amplitude  $\langle |\Delta a|^2 \rangle = \langle \Delta X_1^2 \rangle + \langle \Delta X_2^2 \rangle \geq \frac{1}{2}$ , so zero-point fluctuations of half a quantum. In phase-space, such a mode  $a$  is represented as a Fresnel lollypop, where the noise disc corresponds to the fluctuations in the amplitudes as depicted in Fig. 2.1.4a.

At this point it's suitable to define *phase-insensitive noise* as one which is randomly distributed in phase, meaning that the noise fluctuations are equal and uncorrelated in both quadratures or equivalently the mode is invariant under arbitrary rotations in phase space. States with phase-insensitive noise are, for example, coherent and thermal states[25].

Now we can proceed to the formal definitions. In order for an amplifier to be called *phase-insensitive*, it must meet the following conditions

- If the input possesses phase-insensitive noise, then also the output shows no phase preference;
- If the input phase is advanced by  $\theta$ , the output is either advanced by the same amount (*phase-preserving*), or retarded by  $\theta$  (*phase-conjugating*).

If any of the two conditions are not satisfied, the amplifier is *phase-sensitive*. If we introduce a linear amplifier with different quadrature gains  $G_{1,2}$  and define the state at the input and output respectively as

$$a_{in} = X_1 + iX_2 \quad (2.1.2a)$$

$$b_{out} = Y_1 + iY_2 \quad (2.1.2b)$$

their quadratures will be connected as

$$Y_{1,2} = \sqrt{G_{1,2}} X_{1,2} + \mathcal{F}_{1,2} \quad (2.1.3)$$

where  $\mathcal{F}_{1,2}$  are the quadrature amplitudes of the operator responsible for the added noise  $\mathcal{F}$ . From here on, we choose to work in units of photon number. The number of quanta in the input is connected to the power per unit bandwidth  $\mathcal{P}_{in}(\omega)$  via  $\langle a_{in}^\dagger a_{in} \rangle = \mathcal{P}_{in}(\omega)/\hbar\omega$ . If we express Eq. 2.1.3 in terms of uncertainties

$$\langle \Delta Y_{1,2}^2 \rangle = G_{1,2} \langle \Delta X_{1,2}^2 \rangle + \langle \Delta \mathcal{F}_{1,2}^2 \rangle \quad (2.1.4)$$

we can interpret the output as a mix of amplified input noise quanta and added noise quanta by the amplifier. For a fair comparison of the noise performance of different

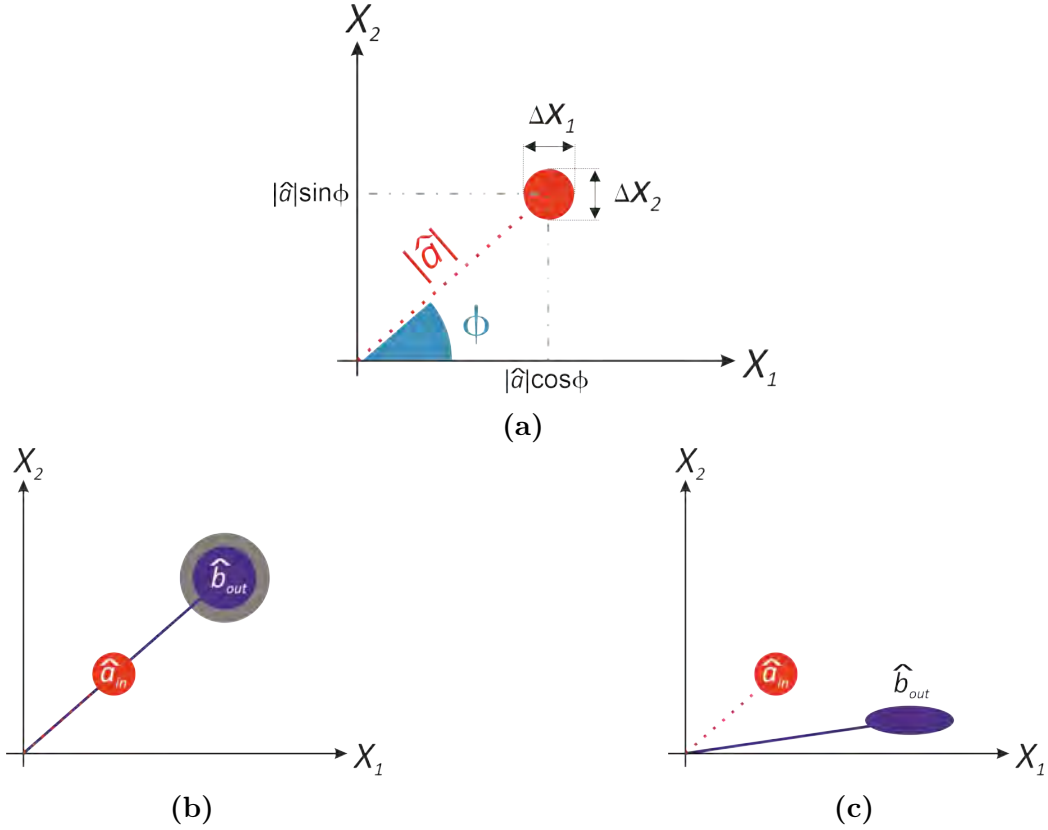


**Figure 2.1.4: Phase-space representation of phase-sensitive and phase-insensitive amplification schemes.** (a) A bosonic mode  $\hat{a}$  in the complex plane is drawn as a disk with its center situated at  $(|\hat{a}|\cos\phi, |\hat{a}|\sin\phi)$ , or in polar coordinates at  $(|\hat{a}|, \phi)$ . The size of the disc  $\Delta X_{1,2}$  is interpreted as the intrinsic noise of the mode. (b) A phase-insensitive scheme amplifies the amplitude and the noise of the input signal  $\hat{a}_{in}$  (orange) equally in both quadratures. However, at least half a photon of noise (grey) is added to the mode at the output  $\hat{b}_{out}$  (purple). (c) Phase-sensitive amplifiers have a preferred quadrature (here  $X_1$ ) which is amplified, while the other is deamplified. The commutation relation does not require the amplifier to add noise.

amplifiers regardless of the gain, the output is referred to the input, meaning simply divided by the gain. Therefore, after referring to the input, Eq. 2.1.4 can be rewritten as

$$\langle \Delta Y_{1,2}^2 \rangle = G_{1,2} \langle \Delta X_{1,2}^{\prime 2} \rangle = G_{1,2} [\langle \Delta X_{1,2}^2 \rangle + A_{1,2}] \quad (2.1.5)$$

where we have defined  $A_{1,2} \equiv \langle \Delta \mathcal{F}_{1,2}^2 \rangle / G_{1,2}$  as the added noise number. To find the minimum for the noise number one should note that the input and output quadratures must satisfy the same commutation relations. This implies the following inequality for the added fluctuations

$$\sqrt{A_1 A_2} \geq \frac{1}{4} \left| 1 - \frac{1}{\sqrt{G_1 G_2}} \right| \quad (2.1.6)$$

if  $[X_1, \mathcal{F}_2] = 0 = [X_2, \mathcal{F}_1]$  i.e. the input field and the internal amplifier mode are uncorrelated.

The relation 2.1.6 sets the limits for both phase-sensitive and phase insensitive amplification. However, it can be simplified for the phase-preserving ( $\sqrt{G_1} = \sqrt{G} = \sqrt{G_2}$ )

and phase-conjugating case ( $\sqrt{G_1} = \sqrt{G} = -\sqrt{G_2}$ )

$$A \geq \frac{1}{2} |1 \mp G^{-1}| \quad (2.1.7)$$

where the upper (lower) sign holds for the phase-preserving (phase-conjugating) case. In this case, the minimum noise added by a high gain amplifier ( $G \gg 1$ ) to both quadratures of the signal (drawn in grey in Fig. 2.1.4b) is exactly half a quantum. Equations 2.1.6 and 2.1.7 are often referred in the literature[7] as Haus-Caves theorem. The amplifier is said to be *quantum-limited* if the added noise equals exactly the quantum limit. An easier way to understand this limit is by remembering the fundamental principle in quantum mechanics that non-commuting variables cannot be measured simultaneously with infinite accuracy. The only reason this is possible while not violating quantum mechanics is the added noise by the amplifier, which forces the variables to commute.

For phase-sensitive amplification, one has the possibility for having the gains connected as  $G_1 G_2 = 1$ , which would result in a lower limit for the added photons being  $A_1 A_2 \geq 0$ . If the input is tailored in a way that only one quadrature carries all information, e.g.  $X_1$ , one can design the amplifier such that  $G_1 \gg 1$  and  $A_1 \ll 1/4$ , i.e. one quadrature is amplified with added noise smaller than the vacuum fluctuations. The accuracy of such measurement would be better than in the phase-insensitive case, but since the quadratures are conjugate variables, this comes at a price of reduced precision for  $X_2$  ( $A_2 \gg 1/4$ ). It is important to stress that adding no noise in a phase-sensitive process is only possible if the initial internal-mode noise and input field noise are correlated. In such case, the output state will be squeezed in one quadrature, e.g.  $\langle \Delta X_2^2 \rangle < 1/4$  (as illustrated in Fig. 2.1.4c). First experimental realization of squeezed states in the circuit QED field was done with a Josephson Parametric Amplifier (JPA)[26]. Nowadays, JPAs are still used for generating squeezed states[9], but the design of the device has evolved since the first implementation.

## 2.2 Superconducting quantum circuits

The principles introduced in the previous section are fundamental to all implementations with small exceptions regarding the amplifier classification. In order to relate them to the field of microwave physics, we introduce the basic building components used for designing the complex circuitry needed for quantum-limited amplification. The big advantage of the circuit QED field is that most of the elements for building elaborate systems are already familiar from electronics, but dissipation has vanished in the superconducting state. The simple circuit elements and the vast diversity of superconductors are the reason for the high flexibility for designing the system parameters.

For a brief reminder of Bardeen-Cooper-Schrieffer (BCS) theory[27], in conventional superconductors the electrons condensate below certain temperature into Cooper pairs which are described by a common wavefunction  $\Phi(r, t) = \sqrt{N(r, t)} e^{i\phi(r, t)}$ . The amplitude of this macroscopic wavefunction is proportional to the number of pairs  $\hat{N}$ , while the phase determines the phase coherence within the superconductor. These variables are conjugate  $[\hat{N}, \hat{\phi}] = -i$  and they are generally related to the material properties and the topology of the superconductor. The collection of Cooper pairs is called superconducting condensate and its motion is described by currents and voltages. Since they are related to  $\hat{N}$  and  $\hat{\phi}$ , current and voltage do not commute and cannot be measured simultaneously. This leads to the discreteness of the energy levels in the circuits.

We will begin with the realization of a harmonic oscillator with superconducting circuits and later introduce the non-linear element which is the reason why we can use superconductors for encoding quantum information.

## 2.2.1 LC oscillator

The harmonic oscillator is an extremely important building block in circuit QED, realized as an LC resonator. A lumped element representation of the circuit is shown in Fig. 2.2.1a. The lumped element approximation[28] is relevant in this case since the spatial dimensions of our circuit components (typically a few hundred microns) are much smaller than the wavelengths in the microwave range. The energy oscillates between magnetic energy in the inductor  $L$  and the electric energy in the capacitor  $C$  with the resonance appearing exactly when the energies stored in both fields are equal. In order to determine the degrees of freedom (DOF) for this circuit, we will be following the method of nodes (Appendix A). Purely classically, the node flux is defined from Faraday's induction law:

$$\Phi(t) = \int_{-\infty}^t v(t') dt' \quad (2.2.1)$$

where the lower time limit is taken sufficiently far in the past when current and voltage were zero. The node flux becomes the position coordinate in the system. The instantaneous time-dependent energy in each element is given by

$$E(t) = \int_{-\infty}^t i(t')v(t') dt'. \quad (2.2.2)$$

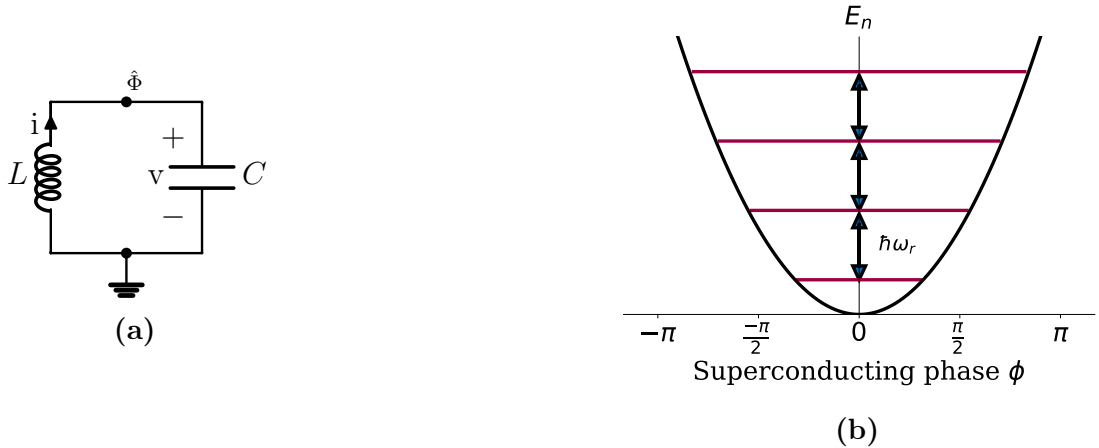


**Figure 2.2.1: LC oscillator.** (a) Lumped-element representation of the resonator, (b) Energy spectrum of the harmonic oscillator with resonance frequency  $\omega_r = (LC)^{-1/2}$ .

Knowing the current-voltage relations for inductors and capacitors  $v = L(di/dt)$ ,  $i = C(dv/dt)$ , we can derive the Lagrangian of the system:

$$\mathcal{L} = \frac{1}{2}C\dot{\Phi} - \frac{1}{2L}\Phi^2. \quad (2.2.3)$$

The momentum conjugate of the flux is the charge through the capacitor

$$Q = \frac{\partial \mathcal{L}}{\partial \dot{\Phi}} = C\dot{\Phi}. \quad (2.2.4)$$

Finally, via Legendre transformation we derive the Hamiltonian of the system

$$H_{LC} = Q\dot{\Phi} - \mathcal{L} = \frac{Q^2}{2C} + \frac{\Phi^2}{2L}. \quad (2.2.5)$$

Up to this point the whole treatment was purely classical. We proceed with canonical quantization by promoting the charge and flux to non-commuting operators satisfying the commutation relation

$$[\hat{\Phi}, \hat{Q}] = i\hbar. \quad (2.2.6)$$

In order for these variables to be treated quantum-mechanically, the energy levels of the oscillator must be well separated. Only then, the node flux and charge observables can be expressed in terms of creation and annihilation operators

$$\hat{\Phi} = \Phi_{ZPF}(\hat{a} + \hat{a}^\dagger) \quad , \quad \hat{Q} = -iQ_{ZPF}(\hat{a} - \hat{a}^\dagger) \quad (2.2.7)$$

where  $\Phi_{ZPF}$  and  $Q_{ZPF}$  are the zero-point fluctuations of the observables. They are dependant on the characteristic impedance  $Z_r = \sqrt{L/C}$  of the LC circuit

$$\Phi_{ZPF} = \sqrt{\frac{\hbar Z_r}{2}} \quad , \quad Q_{ZPF} = \sqrt{\frac{\hbar}{2Z_r}}. \quad (2.2.8)$$

The operator  $\hat{a}^\dagger$  creates excitation in the system which is equivalent to creating a photon of frequency  $\omega_r$  because of the underlying electromagnetic field. Together with the annihilation operator  $\hat{a}$  they satisfy the bosonic commutation relation  $[\hat{a}, \hat{a}^\dagger] = 1$ . Inserting the equations from 2.2.7 in the Hamiltonian 2.2.5 yields the more compact form of the quantum harmonic oscillator Hamiltonian in second quantization

$$\hat{H}_{LC} = \hbar\omega_r \left( \hat{a}^\dagger \hat{a} + \frac{1}{2} \right) \quad (2.2.9)$$

where  $\omega_r = 1/\sqrt{LC}$  is the resonance frequency. The eigenstates are the Fock states satisfying  $\hat{a}^\dagger \hat{a} |n\rangle = n |n\rangle$ , where  $n = 0, 1, 2, \dots$  represents the number of photons in the states. The resulting energy spectrum consists of equidistant levels as shown in Fig. 2.2.1b.

## 2.2.2 Josephson junction

Even though harmonic oscillators are extremely relevant circuits used for the readout of quantum bits (qubits), in order to encode information or amplify a signal, a non-linearity is required. The most successful candidate providing this nonlinearity for our circuits is the Josephson junction[29]. Its flexibility regarding design and fabrication, as well as the lack of dissipation make it an irreplaceable part in our experiments.

In its core, the Josephson junction consists of two superconducting islands

(S) connected by a weak link (I), see Fig. 2.2.2. This connection locally weakens the superconducting condensate, meaning that the critical current  $I_c$  of the junction, which is the maximum current that can be carried before resistance appears, is lower than that of the two superconducting regions alone, hence the name. Depending on the type of weak link we can distinguish several types of junctions, e.g. tunnel junctions (Fig. 2.2.2a) where the superconducting regions are separated by a thin insulating layer, and constriction junctions (Fig. 2.2.2b) with the weak coupling achieved via a narrow superconducting bridge. In each type, the non-linearity has a different origin and the equations describing them are generally very different. Since the amplifier in this thesis is built with tunnel junctions, a treatment of the other types is beyond the scope of this thesis.

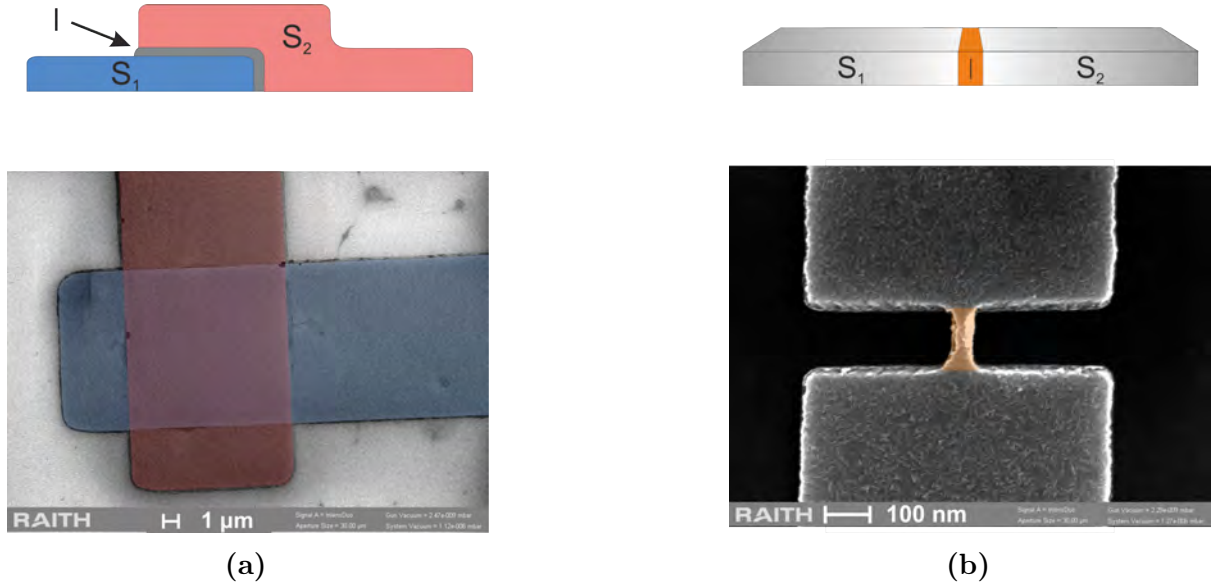


**Figure 2.2.2: Josephson junction: Illustration and images.** In the upper part of (a) and (b) one can see conceptual drawings of a tunnel (a) and a constriction (b) Josephson junctions, consisting of two superconducting regions (S) connected with a weak link (I). In the lower part of the figures false-colored Scanning Electron Microscopy (SEM) pictures of the respective junction types are shown. The tunnel junction (a) is fabricated with optical lithography on a silicon wafer, while the constriction junction (b) is fabricated with electron beam lithography on a sapphire wafer. Both samples from (a) and (b) were fabricated in the Quanten-Nano-Zentrum Tirol (QNZT).

The reason why these elements are lossless is that when two superconductors are placed close to each other, their phases become related. Due to the macroscopic phase difference in the islands  $\hat{\phi} = \hat{\phi}_1 - \hat{\phi}_2$ , supercurrent flows by means of Cooper pairs tunneling through the barrier. The *first Josephson equation* gives the relation between the supercurrent and the phase difference

$$\hat{I}(\hat{\phi}) = I_c \sin \hat{\phi}. \quad (2.2.10)$$

The time-evolution of the phase difference given by the *second Josephson equation*

$$\hat{V}(t) = \frac{\hbar}{2e} \frac{d\hat{\phi}}{dt} \quad (2.2.11)$$

where  $\hat{V}$  is the voltage drop across the junction. The first equation is a direct consequence of the current dependence on the time derivative of the Cooper pair number[30].

It is useful to rewrite expression 2.2.11 in terms of the node flux as defined in Eq. 2.2.1

$$\hat{\phi}(t) = \frac{\hat{\Phi}(t)}{\phi_0} \pmod{2\pi} \quad (2.2.12)$$

where we introduce the reduced magnetic flux quantum  $\phi_0 = \hbar/2e$ . The  $\pmod{2\pi}$  reflects the periodicity of the phase, while allowing the flux variable to take arbitrary real values. This is equivalent to adding a  $2\pi k$  term to the equation, where  $k$  is a non-negative integer.

We can precisely see how this element shifts the energy levels forming an non-uniform spectrum. By inserting the first and second Josephson equations in Eq. (2.2.2) one can derive the energy associated with the Josephson junction

$$E_{pot} = -\phi_0 I_c \cos \hat{\phi} = -E_J \cos \hat{\phi}. \quad (2.2.13)$$

The energy  $E_J$  is called Josephson energy and it is a measure of the tunnelling rate across the barrier. For small phase differences  $\hat{\phi} \ll 1$  we can expand the Josephson potential energy

$$-E_J \cos \hat{\phi} = -E_J + \frac{E_J}{2} \hat{\phi}^2 - \frac{E_J}{24} \hat{\phi}^4 + \mathcal{O}(\hat{\phi}^6). \quad (2.2.14)$$

The second term represents a harmonic potential associated with a linear inductor with  $L_J = \phi_0/I_c$ , often referred to as Josephson inductance. The non-linearity comes from the higher terms in the expansion. For this reason, the Josephson element is often treated as a non-linear inductor.

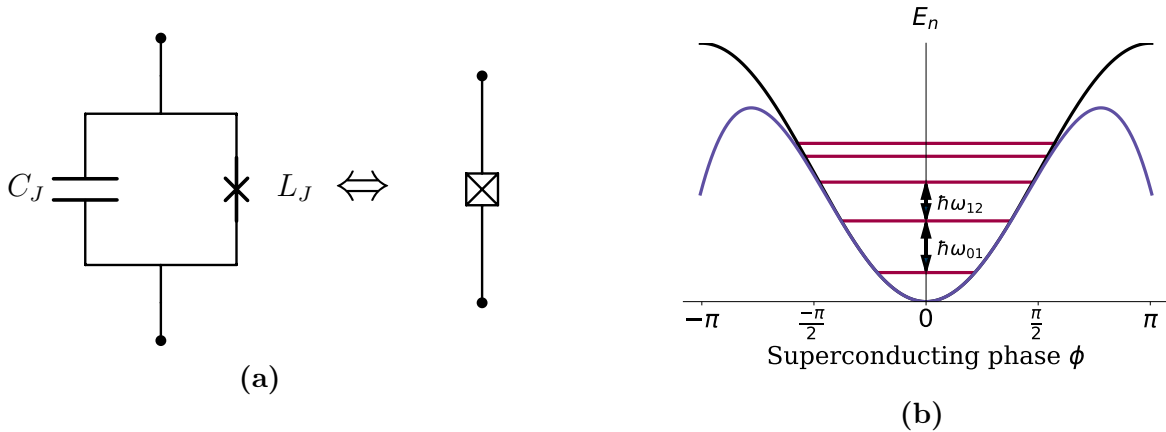


**Figure 2.2.3: Josephson junction: Lumped-element representation and energy spectrum.** (a) The Josephson junction consists of a capacitive  $C_J$  and a non-linear inductive  $L_J(\phi)$  contribution in parallel (left). The square with a cross (right) is the equivalent circuit symbol for a junction. (b) The Josephson potential shown as a full cosine function (black) and expanded up to third order (purple). For a truncated Taylor expansion to the third order, the first few energy levels are shown in magenta.

The superconducting islands with insulator in between form an effective capacitor  $C_J$ , creating the circuit from Fig. 2.2.3a. Notably, it resembles the resonant circuit from Fig. 2.2.1a, where the linear inductor has been replaced by a Josephson element. Therefore, we can define the resonant frequency of the Josephson junction as  $\omega_p = 1/\sqrt{L_J C_J}$ , which

is called the *plasma frequency*. At higher frequencies the circuit behaves as a normal LC resonator. Including the capacitive contribution, the Hamiltonian of the Josephson junction reads

$$\hat{H}_J = \frac{\hat{Q}^2}{2C_J} - E_J \cos \hat{\phi} = 4E_C \hat{N}^2 - E_J \cos \hat{\phi} \quad (2.2.15)$$

where for the kinetic term we have used the charge operator  $\hat{Q} = 2e\hat{N}$  in units of Cooper pairs and defined the charging energy  $E_C = e^2/2C_J$ .

The diagonalization of this Hamiltonian is analytically possible but this task is not a subject of this thesis. For some insight, the expansion up to second order (harmonic approximation) results in equidistant levels, similar to the harmonic oscillator with  $C_J$  and  $L_J$ . The quadratic term carries the non-linearity which shifts the spectral lines in a way that each energy level is individually addressable, see Fig. 2.2.3b. The charging energy determines the frequency difference between the ground and first excited states.

## Superconducting Quantum Interference Device (SQUID)

As already mentioned, tunability is a desired property not only in amplifiers but also in qubits. For this purpose, a single Josephson junction is replaced by a loop interrupted by two junctions (see Fig. 2.2.4), forming a DC Superconducting QUantum Interference Device (SQUID). If an external magnetic field is applied to the DC-SQUID, the effective critical current will be decreased due to the interference between the arms of the device. Just the magnetic field of the Earth passing through the area of a typical SQUID (a few  $\mu\text{m}^2$ ) is enough to achieve several flux quanta, justifying the need of magnetic shielding.

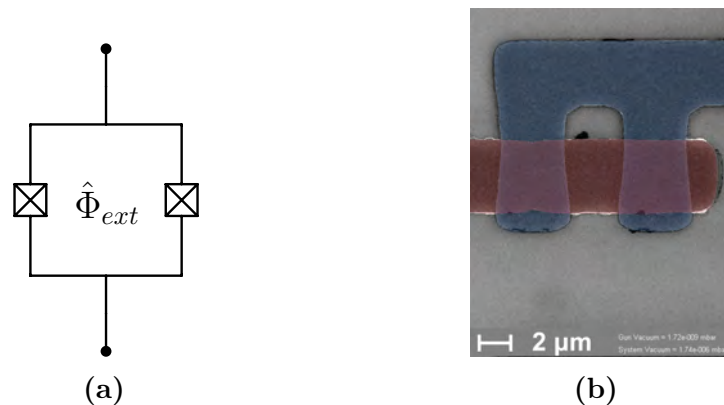


**Figure 2.2.4: DC-SQUID.** (a) Lumped-element representation consisting of two Josephson junctions connected by superconducting leads. The inductance of the device is regulated via the external flux  $\hat{\Phi}_{ext}$  threading the loop. (b) False-colored SEM image of a DC SQUID fabricated in QNZT with optical lithography on silicon. The overlaps between the first (blue) and the second (red) layers form two tunnel junctions in parallel.

Note that superconducting leads also act as inductors and an external magnetic field induces circulating (screening) current in the loop. This current creates a magnetic field to counteract the external influence so the total enclosed magnetic flux remains zero. In the limit of negligible geometric inductance from the loop compared to the Josephson inductance, the external magnetic field is approximately equivalent to the total flux. Once the external field exceeds half a flux quantum, it becomes more favourable for the screening

currents to inverse direction and compensate the difference to one flux quantum. This periodicity is a manifestation of the flux quantization.

In order to emphasise the flux tunability, we write the Hamiltonian for the DC-SQUID by employing the Hamiltonian 2.2.15

$$\hat{H}_{SQUID} = 4E_C \hat{N}^2 - E_{J_1} \cos \hat{\phi}_1 - E_{J_2} \cos \hat{\phi}_2 \quad (2.2.16)$$

where we include the energy contributions from the two junctions  $E_{J_i}$  and their phase differences  $\hat{\phi}_i$ . The flux quantization requires that the flux sum over all branches along a superconducting ring must be an integer number of flux quanta, imposing the relation  $\hat{\phi}_1 - \hat{\phi}_2 = \hat{\phi}_{ext} \pmod{2\pi}$ , where  $\hat{\phi}_{ext} = \hat{\Phi}_{ext}/\phi_0$  with  $\hat{\Phi}_{ext}$  being the total external flux including offsets due to stray fields. This condition eliminates one DOF and by using the average phase difference  $\hat{\phi} = (\hat{\phi}_1 + \hat{\phi}_2)/2$ , we can rewrite the SQUID Hamiltonian[31]

$$\hat{H}_{SQUID} = 4E_C \hat{N}^2 - E'_J(\hat{\phi}_{ext}) \cos \left[ \hat{\phi} - d \tan(\hat{\phi}_{ext}/2) \right]. \quad (2.2.17)$$

The parameter  $d = (E_{J_2} - E_{J_1})/(E_{J_1} + E_{J_2})$  is a measure of how symmetric the SQUID is. We can neglect the terms proportional to it in case the two junctions are completely identical  $d = 0$ .

As can be seen from the Hamiltonian above, a SQUID can be treated as a single junction with flux-dependant energy

$$E'_J(\hat{\phi}_{ext}) = E_{J,\Sigma} \cos(\hat{\phi}_{ext}/2) \sqrt{1 + d^2 \tan^2(\hat{\phi}_{ext}/2)} \quad (2.2.18)$$

where  $E_{J,\Sigma} = E_{J_1} + E_{J_2}$ . Therefore, we can tune the resonance frequencies of devices which utilize DC-SQUIDS. For a symmetric device, we have a flux-tunable inductor with inductance

$$L(\hat{\phi}_{ext}) = \frac{\phi_0}{2I_c \left| \cos(\hat{\phi}_{ext}/2) \right|} \quad (2.2.19)$$

where  $I_c$  is the critical current for a single junction in the SQUID. However, the price is paid by being susceptible to flux noise. With this in mind, it is worth noticing that a larger asymmetry  $d$  leads to continuous tunability in a smaller frequency range, which in turn reduces the sensitivity to flux noise[32]. Another option for reducing the flux noise without compromising with the tunability range is to optimize the geometric design[33].

## Wave mixing

Josephson junctions and SQUIDS are the main nonlinear elements used in circuit QED. As mentioned in Subsection 2.1.1, in order to achieve amplification via wave-mixing, the non-linearity needs to be placed in a resonant circuit. In the circuit context, this would be equivalent to placing a Josephson element or a DC SQUID into a resonant circuit, forming a non-linear resonator with frequency  $\omega_r = 1/\sqrt{CL(t)}$ . Due to the non-linear inductance, we can modulate the effective impedance and achieve wave-mixing. Notably, varying the capacitive elements in time would lead to the same effect.

To gain some insight how to vary the Josephson inductance in time, we investigate the behaviour under different drives[34, 35]. By simply applying an AC current  $I(t) \ll I_c$  through a junction around its resonance frequency, the inductance is modulated as

$L \approx L_J \left[ 1 + \frac{1}{6} \left( \frac{I(t)}{I_c} \right)^2 \right]$ . If we have a monochromatic pump  $I(t) \approx \cos \omega_p t$ , up to the first non-linear term the inductance will be modulated at twice the pump frequency. Because of this quadratic dependence, four-wave mixing can be achieved. Similarly to the Duffing oscillator, the Hamiltonian consists of a harmonic term and a forth-order non-linear term

$$\hat{H}_{JJ}^{RWA} \approx \hbar \omega_r \hat{a}^\dagger \hat{a} + \hbar K (\hat{a}^\dagger)^2 \hat{a}^2 \quad (2.2.20)$$

where  $K$  is known as Kerr coefficient.

On the other hand, by varying the magnetic field enclosed by the SQUID loop the inductance in the unit is modulated proportionally to the screening current  $L \approx L_J \left( 1 + \frac{I(t)}{I_0} \right)$ , where  $I_0$  depends on the DC flux bias through the SQUID. As a consequence, under the same drive used for the current pumping, the first non-linear order is proportional to the pump frequency, meaning that three-wave mixing takes place. For a flux-pumped system, the first non-linear term is of third order, yielding the Hamiltonian

$$\hat{H}_{SQUID}^{RWA} \approx \hbar \omega_r \hat{a}^\dagger \hat{a} + \hbar K [\hat{p}(\hat{a}^\dagger)^2 + \hat{p}^\dagger \hat{a}^2] \quad (2.2.21)$$

where  $\hat{p}$  represents the pump mode. For both Hamiltonians we have used the rotating-wave approximation (RWA) which is valid for weakly non-linear devices, namely for  $|K|/\omega_r \ll 1$ .

The current pumping scheme is widely used in most amplifiers. However, it comes with some disadvantages: in most cases there is no spectral or spatial separation between pump and signal, making it hard for the pump to be filtered. In a flux-driven SQUID, the pump is well separated from the signal. Another main difference is the pump-induced frequency shift regarding the bare resonance which is low in the flux-pumped case while for a current drive the shift increases with the photon population. For three-wave mixing and a  $\lambda/4$  resonator, there is no resonance at  $\omega_p$  reducing the spurious population in higher modes which usually leads to saturation.

## 2.3 Input-Output Theory

Up to this point, every system was described assuming they were completely decoupled from the environment. In fact, controlled coupling to external DOFs allows us to manipulate as well as read the system state. At the same time, the system couples uncontrollably to other degrees of freedom (losses), which results in noise and decoherence. In order to capture all these aspects, the Hamiltonian needs to be expanded with the terms describing the external baths and the coupling to them. There are different ways to describe this interplay between the internal and external DOFs: either from the point of an external observer sending in a signal and analyzing the reflected output (input-output theory[36]), or through the evolution of the system itself under the influence of the bath (master equation formulation[25]). While they all have their advantages depending on the desired information to be extracted, here the focus falls on the first treatment, namely input-output theory (IOT). The results directly give the response of the system under strong (classical) pump and weak (quantum) signals used in the amplification process.

The approach is valid for any system but for simplicity let's consider the harmonic oscillator, as already quantized in Subsection 2.2.1. The total Hamiltonian is a sum of all contributions

$$\hat{H} = \hat{H}_{sys} + \hat{H}_{bath} + \hat{H}_{int}. \quad (2.3.1)$$

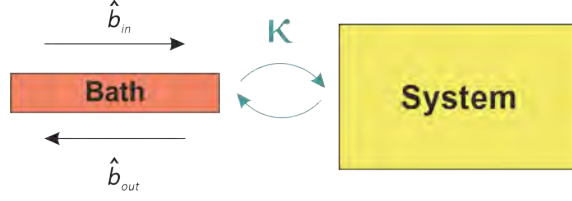


**Figure 2.3.1: Input-Output theory: open-system sketch.** The system couples to an external bath (or a port) with a rate  $\kappa$ . With input-output theory, the output can be predicted for a known input.

Typically the bath is realized as a semi-infinite transmission line. Therefore, we can express the bath and interaction Hamiltonians respectively as

$$\hat{H}_{bath} = \hbar \int \omega \hat{b}^\dagger(\omega) \hat{b}(\omega) d\omega \quad (2.3.2a)$$

$$\hat{H}_{int} = i\hbar \int \bar{\kappa}(\omega) \left[ \hat{b}^\dagger(\omega) \hat{a} + \hat{b}(\omega) \hat{a}^\dagger \right] d\omega \quad (2.3.2b)$$

Here, rotating-wave approximation is used allowing us to neglect counter-rotating terms such as  $\hat{a}^\dagger \hat{b}^\dagger(\omega)$ . The bath operators obey the bosonic commutation relation  $[\hat{b}(\omega), \hat{b}^\dagger(\omega')] = \delta(\omega - \omega')$ . Similarly, one can introduce different ports for losses and input signals. Two-photon loss channels can also be included in the treatment, for more details refer to [37].

Another simplification appears if the coupling rate is frequency independent  $\bar{\kappa}(\omega) \equiv \sqrt{\frac{\kappa}{2\pi}}$  and small  $\kappa \ll \omega_r$ , meaning that the input modes interact with the system only in a small region around the resonant frequency  $\omega_r$  and the interaction is localized in space around the end of the transmission line at  $x = 0$ . This approximation is known as first Markov approximation. In Heisenberg picture, the equations of motion for the bath and system field operators  $\hat{b}(\omega)$  and  $\hat{a}$  read

$$\dot{\hat{b}}(\omega) = -i\omega \hat{b}(\omega) + \sqrt{\frac{\kappa}{2\pi}} \hat{a} \quad (2.3.3)$$

$$\dot{\hat{a}} = -\frac{i}{\hbar} [\hat{a}, \hat{H}_{sys}] - \sqrt{\frac{\kappa}{2\pi}} \int \hat{b}(\omega) [\hat{a}, \hat{a}^\dagger] d\omega \quad (2.3.4)$$

respectively. We solve the equation of motion for the bath modes by simply integrating Eq. 2.3.3, which gives

$$\hat{b}(\omega) = e^{-i\omega(t-t_0)} \hat{b}_0(\omega) + \sqrt{\frac{\kappa}{2\pi}} \int_{t_0}^t e^{-i\omega(t-t')} \hat{a}(t') dt' \quad (2.3.5)$$

where  $\hat{b}_0(\omega) = \hat{b}(\omega, t = t_0)$  is the initial state of the bath mode at time  $t_0 < t$  assumed to be in the remote past. The first term of the equation describes the free evolution of the operator, while the second term describes the evolution due to the interaction with the system.

Inserting this solution in Eq. 2.3.4 yields the Langevin equation for driven and

damped harmonic oscillator

$$\dot{\hat{a}}(t) = -\frac{i}{\hbar}[\hat{a}, \hat{H}_{sys}] - \frac{\kappa}{2}\hat{a}(t) - \sqrt{\kappa}\hat{b}_{in}(t) \quad (2.3.6)$$

where we have defined the input field as

$$\hat{b}_{in}(t) = \frac{1}{\sqrt{2\pi}} \int e^{-i\omega(t-t_0)} \hat{b}_0(\omega) d\omega. \quad (2.3.7)$$

Normally, this input field is connected to a forward travelling field operator  $\hat{A}_{in}(t-x/v_p) \sim \int d\omega [e^{-i\omega(t-t_0)} e^{-ix/v_p} \hat{b}_0(\omega) + \text{h.c.}]$  defined by the initial conditions  $b_0(\omega)$ , where  $v_p$  is the phase velocity in the transmission line. At the point of interaction  $x=0$ , namely the interface between the end of the transmission line and the system, and after employing RWA the field reduces to the expression above[38, 24].

The forward Langevin equation 2.3.6 describes the evolution of the quantum system in a presence of an external drive. Moreover, as mentioned before one can see that coupling to any port, regardless of the type (input or loss), always results in damping of the system modes. Similar considerations apply to the output field, which is linked to an outward travelling field operator  $\hat{A}_{out}(t+x/v_p)$ . If we define the output field as

$$\hat{b}_{out}(t) = \frac{1}{\sqrt{2\pi}} \int e^{-i\omega(t-t_1)} \hat{b}_1(\omega) d\omega \quad (2.3.8)$$

where  $\hat{b}_1(\omega) = \hat{b}(\omega, t=t_1)$  is the final state of the bath operator at time  $t_1 > t$  in the remote future. This yields another Langevin equation for the intra-cavity mode in terms of the output field. By comparing the two, we reach the main equation in the IOT connecting the incident to the outgoing field via the system modes

$$\hat{b}_{out}(t) - \hat{b}_{in}(t) = \sqrt{\kappa}\hat{a}(t). \quad (2.3.9)$$

This relation holds for all incident fields, regardless of the source. Causality is preserved, meaning that only the future state of the system is affected by the present input and that only the future output is influenced by the present state of the system.

### 2.3.1 Driven coupled non-linear resonators: Bose-Hubbard dimer

The amplifier in this thesis can be treated effectively as two coupled non-linear oscillators as depicted in Fig. 2.3.2. Such a system is very intuitive to understand the phenomena behind the amplification, while avoiding the complex lengthy mathematical expressions. Qualitatively, the results apply to the DJJAA case.

The system is described by the so-called Bose-Hubbard Hamiltonian

$$H = \hbar\omega_R a_R^\dagger a_R + \hbar\omega_L a_L^\dagger a_L + \hbar J(a_R a_L^\dagger + a_L a_R^\dagger) + \hbar \frac{U}{2} \left[ (a_R^\dagger)^2 a_R^2 + (a_L^\dagger)^2 a_L^2 \right] \quad (2.3.10)$$

where we assume that the on-site interaction is of the same strength for both modes  $U_R = U_L = U$ . Because the cavities are identical, their resonant frequencies are also the same  $\omega_L = \omega_R = \omega_0$ . We limit the description to the case where only the left resonator is

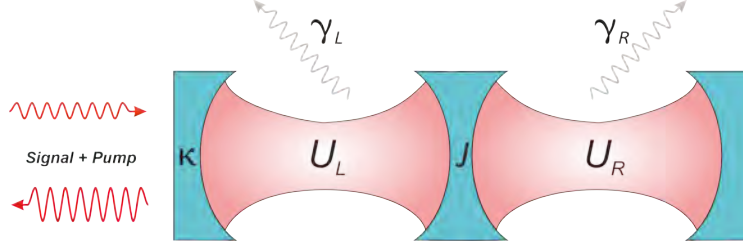


**Figure 2.3.2: Optical representation of two coupled anharmonic resonators.** A first dimer from the amplifier in its core is similar to two cavities with on-site interaction  $U_L, U_R$  and hopping rate  $J$ . Only the left cavity is coupled to the input field with rate  $\kappa$  while both cavities are characterized by the loss rates  $\gamma_L, \gamma_R$ . Figure is adopted from [20].

coupled to the input port, while the right cavity is only coupled to the left. In order to achieve amplification, we choose to work in the regime where the hopping rate is of the same order as the input coupling, while the non-linearity is weak, namely  $|U| \ll J \lesssim \kappa$ . The last approximation involved is that the loss rates are identical and much smaller than the coupling rate to the input port  $\gamma_L = \gamma_R = \gamma \ll \kappa$ , therefore, we can neglect the losses in the left cavity.

With all aforementioned consideration, we can proceed to the Langevin equations

$$\dot{a}_L = \left[ -i(\omega_0 + Ua_L^\dagger a_L) - \frac{\kappa}{2} \right] a_L - iJa_R + \sqrt{\kappa}a_{in} \quad (2.3.11a)$$

$$\dot{a}_R = \left[ -i(\omega_0 + Ua_R^\dagger a_R) - \frac{\gamma}{2} \right] a_R - iJa_L \quad (2.3.11b)$$

For amplification a strong coherent pump is required. We decompose the fields into a classical part  $\alpha$  and a weak quantum signal  $b$

$$a_i = (\alpha_i + b_i)e^{-i\omega_p t} \quad (2.3.12a)$$

$$a_{in} = (\alpha_{in} + b_{in})e^{-i\omega_p t} \quad (2.3.12b)$$

where we chose to work in a frame rotating at the pump frequency  $\omega_p$ .

First we solve the stationary equations for the classical field part, neglecting the quantum corrections, obtaining a single or many steady state solutions depending on the pump parameters  $\langle \alpha_L, \alpha_R \rangle = f(\omega_p, \alpha_{in})$ . To determine the stability of the solutions, one needs to take into account the quantum fluctuations around the classical stationary solutions. If we replace the classical fields in Eq. 2.3.12a and 2.3.12b with their steady state solutions and insert the expressions in Eq. 2.3.11a and 2.3.11b, we can derive the forward Langevin equations for the quantum fluctuations yielding the following linear system of equations

$$\dot{\vec{b}} = \tilde{M}\vec{b} + \sqrt{\kappa}\vec{b}_{in} \quad (2.3.13)$$

where we introduced the vectors  $\vec{b} = (b_L, b_L^\dagger, b_R, b_R^\dagger)^T$  and  $\vec{b}_{in} \stackrel{\gamma \ll \kappa}{\approx} (b_{in}, b_{in}^\dagger, 0, 0)^T$ . The terms which are only proportional to the classic fields are omitted in the derivation. The exact form of the matrix  $\tilde{M}$ [20] is irrelevant for the understanding of the stability problem.

This matrix  $\tilde{M}$  is sometimes referred as stability matrix. If the real parts of all its eigenvalues are negative, i.e.  $\text{Re}(E_\beta) < 0$ ,  $\beta = 1, \dots, 4$ , the fluctuations are damped out and the steady state is unique and stable (S). On the other hand, if at least one is non-

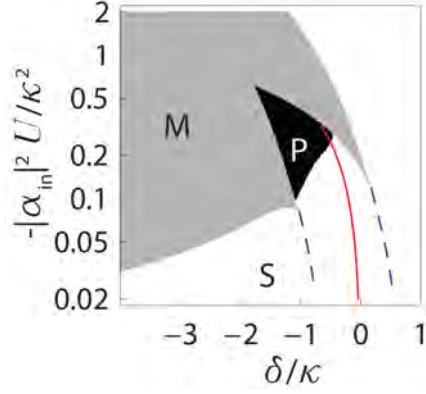


**Figure 2.3.3: Phase diagram of driven coupled non-linear resonators for  $J = 0.7\kappa$  and  $U < 0$ .** The graph is plotted as a function of the pump detuning from the bare cavity frequency  $\delta = \omega_p - \omega_0$  and the pump induced frequency shift  $-|\alpha_{in}|^2 U$ , both normalized to the coupling. The quantum fluctuations around the steady states determine the stability of the solutions: S - unique and stable, P - unique, but parametrically unstable, and M - multiple stable solutions. For phase-sensitive amplification, the pump parameters follow the blue dashed lines, while phase-insensitive amplification occurs for pump parameters tracking the solid red line. Taken from [20].

negative  $\text{Re}(E_\beta) \geq 0$ , the solution is unstable. The latter case is split in two, depending on the imaginary part of the eigenstates: for  $\text{Im}(E_\beta) = 0$  we enter into one-mode unstable solution (M), while for  $\text{Im}(E_\beta) > 0$  the solution is parametrically unstable (P). With this information, the phase-diagram of the system can be extracted as seen in Fig. 2.3.3.

In Fig. 2.3.4 examples are given for each solution at moderate pump amplitude ( $U_j |\alpha_j|^2 < J, \gamma$ ) depending only on the pump frequency. A brief introduction to the notation: because of the linear coupling, the two oscillators hybridize into symmetric  $a_+$  and antisymmetric  $a_-$  modes with the energy splitting depending linearly on the hopping rate  $\omega_+ - \omega_- = 2J$ . In a real device, this splitting is not constant but depends on the mode number. Since in our case  $U < 0$ , the resonances are red-shifted, a drive would shift down the resonance frequencies with an amount proportional to the drive strength. If the pump is applied above the resonances (Fig. 2.3.4a), the energy levels are pushed further off resonance and the solution remains stable no matter the power. When the pump is just below the higher frequency resonance (Fig. 2.3.4b), the red shift pushes the level into resonance and gives rise to one-mode instability, analogous to a driven anharmonic oscillator. This phase shows bistabilities[39, 20], hence the multiple classical solutions. For a pump in between the resonances (Fig. 2.3.4c), because of the red shift of the symmetric mode combined with the linewidth increase of the antisymmetric one, the field becomes resonant to both modes. The quantum fluctuations create entangled signal and idler photons as soon as the amplitude overcomes the losses, i.e.  $U_j |\alpha_j|^2 > \gamma$ . This regime corresponds to phase-insensitive parametric amplification. From this point on, the focus will be on this regime. For a more thorough analysis on the stability, the reader should refer to [39].

The gain can also be inferred from input-output theory after utilizing the Fourier transform for all fields[20]

$$b_j(t) = \frac{1}{\sqrt{2\pi}} \int b_j(\Delta) e^{-i\Delta t} d\Delta \quad (2.3.14)$$

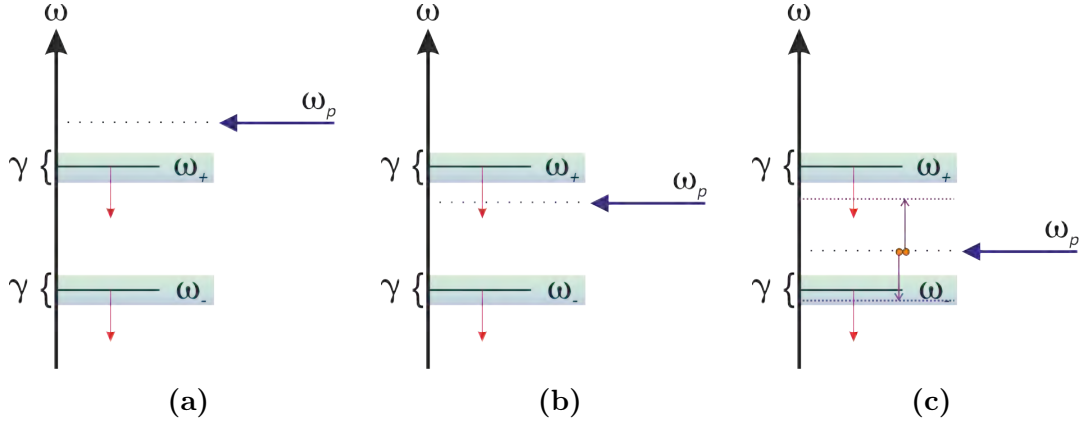


**Figure 2.3.4: Energy level scheme under continuous monochromatic drive.** (a) Stable: The pump frequency is above the modes and never comes into resonance for any power, (b) One-mode unstable: the pump comes in resonance with the mode above a certain threshold due to the non-linear red shift, (c) Parametrically unstable: starting from stable solution once the losses are surpassed, the pump comes in resonance with the red-shifted anti-symmetric and broadened symmetric mode, generating entangled photon pairs in the resonator modes. Figure adopted from [39].

where  $\Delta = \omega_p - \omega_i$  is the detuning between the pump and the signal. If we insert this expression in Eq. 2.3.13, we get a new set of equations

$$\vec{\dot{b}}(\Delta) = \sqrt{\kappa}(-i\Delta\mathbf{1} - \tilde{M})^{-1}\vec{b}_{in}(\Delta) = \sqrt{\kappa}\tilde{G}(\Delta)\vec{b}_{in}(\Delta) \quad (2.3.15)$$

where we define  $\tilde{G}(\Delta)$  as the gain matrix.

The input-output relation 2.3.9 links the quantum part of the output to the input such that

$$b_{out}(\Delta) = g_s(\Delta)b_{in}(\Delta) + g_i(\Delta)b_{in}^\dagger(-\Delta) \quad (2.3.16)$$

meaning that the output is a mix of amplified input waves with equal and opposite detunings from the pump. The gains are respectively

$$g_s(\Delta) = \kappa\tilde{G}_{11}(\Delta) - 1 \quad (2.3.17a)$$

$$g_i(\Delta) = \kappa\tilde{G}_{22}(\Delta) \quad (2.3.17b)$$

where  $\tilde{G}_{11,22}$  are the diagonal components from the gain matrix  $\tilde{G}$ . Thus, if pump and system parameters are known, the gain can be predicted.

## 2.4 Dimer Josephson Junction Array Amplifier (DJJAA)

The Dimer Josephson Junction Array Amplifier, or shortly DJJAA, is based on a dispersion-engineered array of SQUIDs. The device can be operated in both degenerate and non-degenerate mode offering a broad horizon for various applications. In contrast to the travelling wave amplifiers, amplification in DJJAA is only possible within a small vicinity around the eigenfrequencies of the circuit due to the standing-wave character. This

drawback is minimized by utilizing long SQUID arrays on the order of  $10^3$  units. Hence, we get a multi-mode tunable amplifier in the frequency domain up to the plasma frequency which has an increased dynamic range in contrast to the single-junction case.

As we already know, the SQUID can be thought of as a single Josephson junction with tunable energy. In this context, the terms Josephson junction array and SQUID array will be used interchangeably in this section. In order to get insight in the working principle of the DJJAA, we first derive the Hamiltonian for Josephson junction arrays which is easily generalized for the DJJAA case once dispersion engineering is included.

### 2.4.1 Josephson junction arrays (JJAs)

Josephson junction arrays by definition are two-dimensional lattices consisting of multiple ( $N \geq 3$ ) Josephson elements connected by superconducting leads[40]. When expanded to three dimensions, the model becomes suitable for describing granular superconductors, such as granular aluminum (grAl[41]). In the span of this thesis, we will limit the description to the one-dimensional chain of Josephson junctions and use the name interchangeably.

The number of unit elements  $N$  determines the number of eigenmodes, while the dependence of the eigenfrequencies  $\omega_k(k)$  on the mode number  $k$  is called *dispersion relation*. In general, the dispersion relation is influenced mainly by the circuit parameters and the boundary conditions, which depend on the type of coupling: galvanic or capacitive. Notably, the boundary conditions also determine the standing wave pattern. For galvanic coupling, the current exhibits antinodes at both ends of the array, while in a capacitively coupled array the voltage antinodes are located at the end of the array.

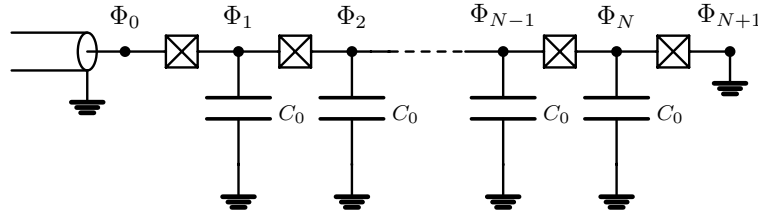


**Figure 2.4.1: Josephson junction array: Lumped-element representation.** Circuit diagram of a one-dimensional chain of  $N$  Josephson junctions coupled galvanically to a transmission line for controlling the system. The superconducting islands connecting the junctions possess a capacitance to ground  $C_0$ .

Let us consider the galvanically coupled array from Fig. 2.4.1, consisting of  $N$  junction connected in series. SQUIDs are usually the preferred unit element since they allow frequency tunability of the device. The boundary conditions impose  $\Phi_0 = 0 = \Phi_{N+1}$  since the voltage, related to the time derivative of the node flux, has to vanish at the galvanic connection in the absence of drives. The stray capacitances  $C_0$  between the superconducting leads connecting the units and the ground are taken into account. For simplicity the inductive contributions from the superconducting islands are neglected.

In order to find the eigenfrequencies for the dispersion relation, we write the Lagrangian by using the method of nodes

$$\mathcal{L} = \sum_{i=1}^{N-1} \frac{C_0}{2} \dot{\Phi}_i^2 + \sum_{i=0}^{N-1} \left[ \frac{C_J}{2} (\dot{\Phi}_{i+1} - \dot{\Phi}_i)^2 - E_J \cos(\phi_{i+1} - \phi_i) \right] \quad (2.4.1)$$

where we have assumed all units are perfectly identical. The first two terms are related to the kinetic energies from the superconducting leads and the junctions, while the last term represents the potential energy from the Josephson elements. The conversion to SQUIDS can be executed by taking into account the flux dependence of the Josephson energies  $E_J \rightarrow E_J(\phi_{ext})$ . The sums run up to  $N - 1$  because the boundary conditions eliminate two DOFs.

In the limit of small currents  $I \ll I_c$  we can expand the cosine  $E_J \cos(\phi_{i+1} - \phi_i) \approx E_J - \frac{1}{2L_J}(\Phi_{i+1} - \Phi_i)^2$ . If we can neglect the constant energy offset from the expansion and introduce the node flux vector  $\vec{\Phi} = (\Phi_0, \Phi_1, \dots, \Phi_N)^T$ , the Lagrangian is simplified to the matrix form

$$\mathcal{L} = \frac{1}{2} \dot{\vec{\Phi}}^T \tilde{C} \dot{\vec{\Phi}} - \frac{1}{2} \vec{\Phi}^T \tilde{L}^{-1} \vec{\Phi} \quad (2.4.2)$$

where the capacitance and inverse inductance matrices read respectively

$$\tilde{C} = \begin{pmatrix} 2C_J + C_0 & -C_J & 0 & \dots & & \\ -C_J & 2C_J + C_0 & -C_J & 0 & \dots & \\ 0 & -C_J & 2C_J + C_0 & -C_J & 0 & \dots \\ \vdots & \vdots & \vdots & \vdots & \vdots & \ddots \end{pmatrix} \quad (2.4.3a)$$

$$\tilde{L}^{-1} = \begin{pmatrix} \frac{2}{L_J} & -\frac{1}{L_J} & 0 & \dots & & \\ -\frac{1}{L_J} & \frac{2}{L_J} & -\frac{1}{L_J} & 0 & \dots & \\ 0 & -\frac{1}{L_J} & \frac{2}{L_J} & -\frac{1}{L_J} & 0 & \dots \\ \vdots & \vdots & \vdots & \vdots & \vdots & \ddots \end{pmatrix}. \quad (2.4.3b)$$

In this treatment we neglect the long-range Coulomb interactions mediated via the substrate[42]. This would give a model fitting the experimental results better, but leading to more intricate expressions for the capacitance matrix.

We follow the recipe from [43] and use the following transformation in order to diagonalize the Lagrangian

$$\vec{\xi} = \tilde{C}^{1/2} \vec{\Phi} \quad (2.4.4)$$

where we introduces the square root of the capacitance matrix in a way that  $\tilde{C}^{1/2} \tilde{C}^{1/2} = \tilde{C}$ . If we solve the following eigenvalue problem

$$\tilde{C}^{-1/2} \tilde{L}^{-1} \tilde{C}^{-1/2} \vec{\Psi}_k = \omega_k^2 \vec{\Psi}_k \quad (2.4.5)$$

we find the needed information for the standing wave pattern and the dispersion relation. The eigenvectors are related to the node flux vectors in the following way

$$\vec{\Phi}_k = \sqrt{\frac{\hbar}{2\omega_k}} \tilde{C}^{1/2} \vec{\Psi}_k \quad (2.4.6)$$

where the link to the flux vector  $\vec{\Phi}$  from the Lagrangian in Eq. 2.4.2 is simply given by  $\vec{\Phi} = \sum_k \vec{\Phi}_k$ .

With this information and plugging in realistic values, the standing-wave pattern and the dispersion relation for a JJA with  $N = 800$  are plotted for the first six modes in Fig. 2.4.2. From the coupling type, we expect the current to reach its maximum at both ends of the array. With the current being proportional to the gradient of the node flux, our expectations are fulfilled since the standing waves are zero at these points. In

fact, the current and voltage behaviour along the array is a direct consequence of the standing-wave pattern. It is worth mentioning that the amplitudes always reduce with increasing the mode number.

In the dispersion relation, the linear regime is prominent up to the third mode where the frequencies are approximately equally detuned from each other. Once the wavelength of the modes approaches the distance between circuit elements the dispersion becomes non-linear as the eigenfrequencies start bunching below the plasma frequency. The range of the linear regime is controlled by the ratio  $C_J/C_0$ , in a way that increasing it results in a higher slope and hence smaller linear range. For more junctions the dispersion flattens and the linear regime extends over a bigger range. Moreover, the number of units is inversely proportional to the frequency difference between two adjacent modes. Notably, because of the additional capacitive contribution to ground  $C_0$ , the plasma frequency is altered  $\omega_{pl} = \frac{1}{\sqrt{L_J(C_J+C_0/4)}}$  but the parameter regime we are in ( $C_J \gg C_0$ ) allows us to neglect this modification.

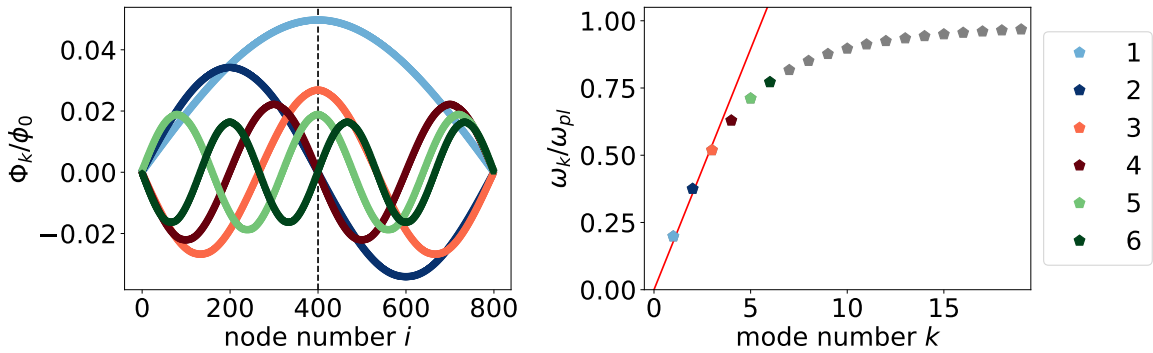


**Figure 2.4.2: Standing-wave pattern and dispersion relation for a Josephson junction array with  $N = 800$ .** Left plot illustrates the standing-wave pattern of the first six magnetic flux eigenvectors normalized by the reduced flux quantum  $\phi_0$  as a function of the node number. The corresponding eigenfrequencies are plotted on the right with the color legend for the respective mode number. The higher modes are colored in gray up to  $k = 18$  where the dispersion relation is truncated for clarity purposes. The first three modes are fitted linearly (red).

In order to quantize the system, we express the coordinate  $\xi$  in terms of its Fourier components  $\vec{\Psi}_k$

$$\vec{\xi}(t) = \sum_k \vec{\Psi}_k (\psi_k^* e^{i\omega_k t} + \psi_k e^{-i\omega_k t}) \quad (2.4.7)$$

where each pair  $\vec{\Psi}_k, \omega_k$  corresponds to the solutions from the eigenvalue problem 2.4.5. Then we introduce bosonic single mode annihilation operator as  $\hat{a}_k = \sqrt{\frac{2\omega_k}{\hbar}} \psi_k$ , which allows us to express the linear Hamiltonian in second quantization

$$\hat{H}_L = \sum_{k=0}^{N-1} \hbar\omega_k \left( \hat{a}_k^\dagger \hat{a}_k + \frac{1}{2} \right). \quad (2.4.8)$$

Note that all classical vectors have been promoted to quantum operators with the inherent

uncertainty relations.

## Kerr-nonlinearity as perturbation

So far in the treatment all non-linearities have been neglected by taking just the harmonic approximation, resulting in equations describing a chain of linear oscillators. However, while sufficient for extracting the standing wave pattern and the frequencies for low input powers, the harmonic approximation fails to capture the intrinsic nonlinearity of the Josephson junctions present in the chain. The higher orders in the expansion of the cosine term in Eq. 2.4.1 allow us to treat this non-linearity perturbatively[43, 42]. Hence, we can expand the Hamiltonian in the following way

$$\hat{H}_{JJA} = \hat{H}_L + \hat{H}_{NL} \quad (2.4.9)$$

where the second term can be expressed as

$$\hat{H}_{NL} = \frac{E_J}{24} \sum_{i=0}^{N-1} (\hat{\phi}_{i+1} - \hat{\phi}_i)^4 \quad (2.4.10)$$

This additional term gives rise to the following second quantization Hamiltonian:

$$\hat{H}_{JJA} = \sum_{k=0}^{N-1} \left[ \hbar\omega'_k \hat{a}_k^\dagger \hat{a}_k - \frac{\hbar}{2} K_{kk} (\hat{a}_k^\dagger \hat{a}_k)^2 \right] - \frac{\hbar}{2} \sum_{\substack{k,l=0 \\ k \neq l}}^{N-1} K_{kl} \hat{a}_k^\dagger \hat{a}_k \hat{a}_l^\dagger \hat{a}_l \quad (2.4.11)$$

where the rotating-wave approximation has been utilized and the higher terms describing interaction between more than two modes, even a pairwise interaction via a third mode, have been neglected.

The coefficient  $K_{kk}$  is called self-Kerr coefficient and gives the frequency shift of the  $k$ -th mode depending on its photon population. This is the main culprit for the bistability in resonators[44, 45] but it is also responsible for the gain in these devices. The so-called cross-Kerr coefficient  $K_{kl}$  causes a frequency shift in the  $k$ -th mode, which scales linearly with the photon number in mode  $l$ . The cross-Kerr shifts is the main ingredient of two-tone spectroscopy[46, 45]. The exact expressions for  $K_{kk}$  and  $K_{kl}$  can be found in Appendix B.

In general, the Kerr shifts grow with increasing the mode number but similarly to the dispersion relation they saturate once the plasma frequency is approached. However, because of the perturbative nature of those shifts they are small compared to the eigenfrequencies, i.e.  $|\sum_l K_{kl}| \ll \omega_k$ . Moreover, in a chain of  $N$  junctions they are reduced by a factor of  $N$  compared to the single junction case since the wave function amplitude scales as  $N^{-1/2}$ [6]. Therefore, the total nonlinearity is reduced and we profit in higher saturation powers[47]. Finally, the renormalized eigenfrequencies are given by

$$\omega'_k = \omega_k - \frac{K_{kk}}{2} - \frac{1}{4} \sum_{l=0}^{N-1} K_{kl}. \quad (2.4.12)$$

Due the non-linear nature of JJAs, they are commonly used in a class of degenerate amplifiers called Josephson Parametric Amplifiers (JPAs)[9, 8]. The implementation usually includes embedded JJA in a coplanar waveguide and when

a pump tone is applied on resonance with an array mode, degenerate amplification is achieved. Bear in mind that there are JPAs, consisting of a single DC SQUID[48]. For non-degenerate amplification, we need dispersion engineering as explained in the following section.

### 2.4.2 Dispersion engineering: Coupled JJAs

We have worked through all ingredients required for building a tunable amplifier with high 1-dB compression point and optimized for non-degenerate operation. As already mentioned in Subsection 2.3.1, an easy way to do that is by using a system similar to the Bose-Hubbard dimer and achieve the same phenomena. If we have to make a link between the platforms, a single JJA can be thought of a non-linear resonator, where the self-Kerr is equivalent to the effective on-site interaction and depends on the charging energy  $E_C$  and the number of SQUIDs. In order to build a dimer amplifier, we need to couple two arrays, where the coupling  $J$  between the resonators can be achieved via the central capacitor  $C_c$ .

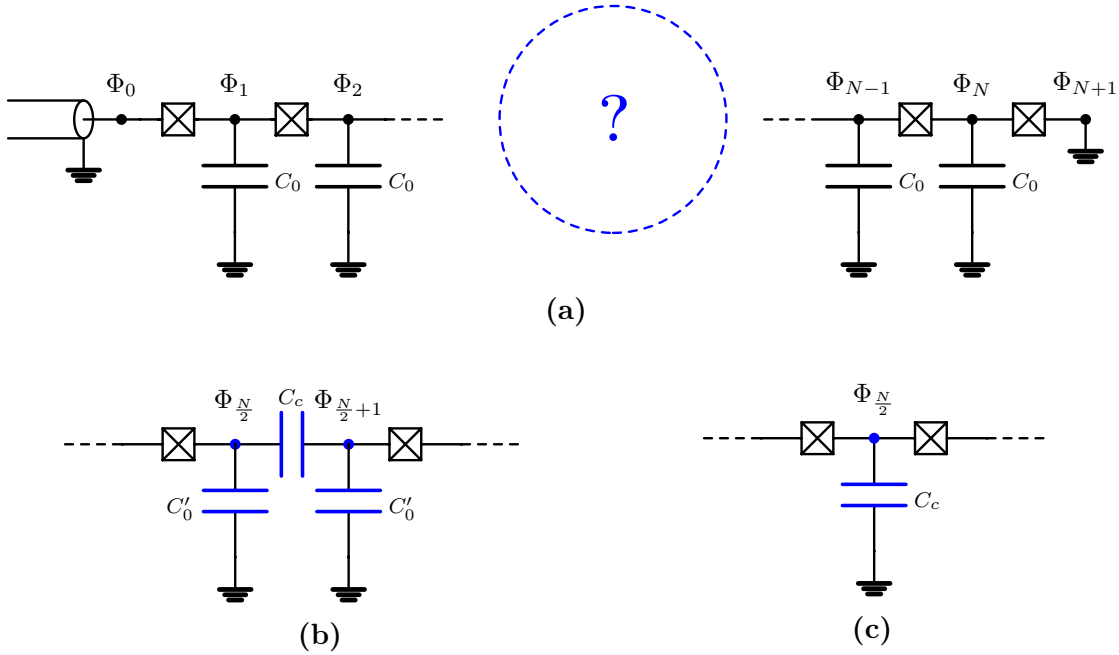


**Figure 2.4.3: Dispersion engineered Josephson junction arrays.** If we take a JJA of size  $N$  (a), interrupt it effectively creating two smaller arrays of size  $N/2$  and couple them via a capacitor  $C_c$  we can engineer the dispersion relation. In fact, this coupling can be implemented by either connecting the capacitor in series (b) or introducing a big capacitor to ground (c). Note that due to the big capacitor plates of  $C_c$  in (b), the neighbouring capacitors to ground are  $C'_0$  enhanced as well.

Consider the JJA from the previous section. If a capacitor is placed in the center of the array (see Fig. 2.4.3), it is effectively split in two shorter arrays coupled capacitively. There are two ways to engineer the arrays: either placing the capacitor in series with the JJAs or coupling them through the ground. The two cases are displayed in figures 2.4.3b and 2.4.3c, respectively, where the modified parts are highlighted in blue. In Fig. 2.4.3b the neighbouring capacitive contributions to the ground are coming from the plates in the



matrix entries due to the dispersion engineering are highlighted in blue consistent with the coloring in the circuit diagram from Fig. 2.4.3b, while the rest has the same shape as in the case for a simple Josephson junction array.

Solving the eigenvalue problem from before (Eq. 2.4.5) but using instead the newly introduced matrices, one can obtain the new standing wave pattern together with the eigenfrequencies of the modes in the low-power regime as seen in Fig. 2.4.4 (left). Analogous to two coupled oscillators in classical mechanics, the arrays hybridize into symmetric (even) and anti-symmetric (odd) modes. Notably, the charge distribution is altered owing to the big capacitor in the center, causing discontinuities in the odd flux modes at that point. Compared to the simple JJA, the odd modes have their maxima at the central node position, which is the reason why they are influenced the most by the interruption through the capacitor.

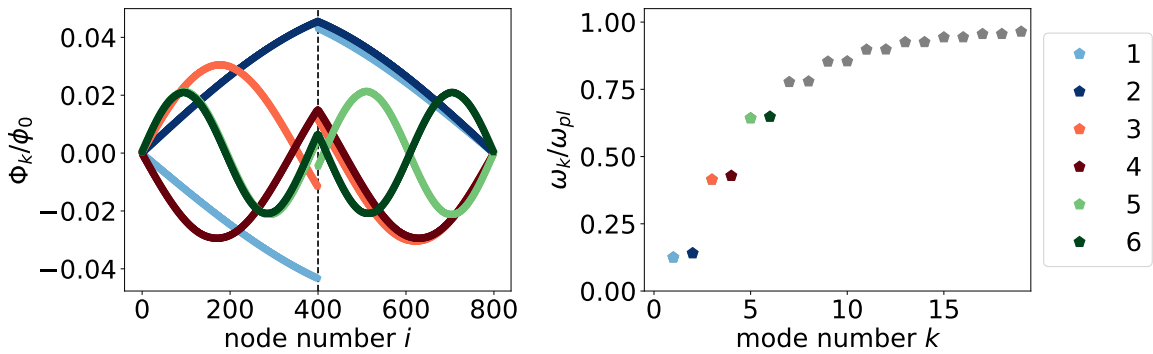


**Figure 2.4.4: Standing-wave pattern and dispersion relation for a dimer Josephson junction array with  $N = 800$ .** Left plot illustrates the standing-wave pattern of the first six magnetic flux eigenvectors normalized by the reduced flux quantum  $\phi_0$  as a function of the node number. The odd modes experience a jump at the center because of the central capacitor. Because of that, the eigenfrequencies hybridize in pairs as plotted in the dispersion relation on the right. The higher modes are colored in gray up to  $k = 18$  where the dispersion relation is truncated for clarity.

As a consequence of this symmetry breaking, each pair of neighbouring modes hybridizes into a so-called dimer (see Fig. 2.4.4, right). Each dimer obeys similar physics as the Bose-Hubbard model from Subsection 2.3.1 but the frequency splitting between the dimer modes now depends on the mode number and the coupling capacitance  $J(k, C_c)$  which we can engineer as wished. The small detuning within one dimer allows the two modes to couple to a single monochromatic drive, leading to non-degenerate amplification.

In the harmonic approximation we obtain the linear Hamiltonian as a sum of linear oscillators  $\hat{H}_L = \sum_{k=0}^{N-1} \hbar\omega_k \left( \hat{a}_k^\dagger \hat{a}_k + \frac{1}{2} \right)$ . We can again introduce the non-linearity as a perturbation. The jump experienced by the odd modes at the center causes artificially large values for the Kerr coefficients due to numerical instabilities. We can evade this problem if instead we use a symmetrized version of the flux eigenvectors only for the odd modes, namely

$$\vec{\Phi}_k^{(s)} = \vec{\Phi}_m^T \cdot \text{diag}(1, 1, \dots, 1, 1, -1, -1, \dots, -1, -1) \quad (2.4.15)$$

where the sign change in the diagonal matrix appears at the index  $\frac{N}{2} + 1$ . Consequently,

the symmetrized phase eigenvectors  $\vec{\Psi}_k$  are calculated from

$$\vec{\Psi}_k^{(s)} = \sqrt{\frac{2\omega_k}{\hbar}} \tilde{C}^{1/2} \vec{\Phi}_k^{(s)} \quad (2.4.16)$$

With the quantum symmetrized flux vectors, we can express the Hamiltonian in second quantization language

$$\hat{H}_{DJJAA} = \sum_{k=0}^{N-1} \left[ \hbar\omega'_k \hat{a}_k^\dagger \hat{a}_k - \frac{\hbar}{2} K_{kk} \left( \hat{a}_k^\dagger \hat{a}_k \right)^2 \right] - \frac{\hbar}{2} \sum_{\substack{k,l=0 \\ k \neq l}}^{N-1} K_{kl} \hat{a}_k^\dagger \hat{a}_k \hat{a}_l^\dagger \hat{a}_l \quad (2.4.17)$$

where the resonant frequencies are shifted by the non-linearity in the same way as for the Josephson junction array (Eq. 2.4.12). The Kerr coefficients, although given by the same equations, are entirely different from the ones of the JJA enhancing the cross-Kerr interaction, which is the reason why non-degenerate amplification is possible.

Each dimer can be exploited for non-degenerate amplification if a pump is applied between the two modes comprising the dimer. Moreover, degenerate amplification is attainable in the same way as for JPAs, i.e. by pumping at the mode frequency itself. Potentially, breaking the symmetries in a similar manner can lead to other interesting applications different than non-degenerate amplification, e.g. single-shot readout circumventing the need of a quantum-limited amplifier[45].

# Chapter 3

## Fabrication

The amplifiers characterized in this thesis are fabricated with optical lithography. In fact, more than half of the time spent on this project was dedicated to getting the optical lithography running in the QNTZ clean room. This chapter starts with a short introduction on the photo-lithography process and emphasizes the main differences between the two systems used for patterning the circuits, namely laser writer and mask aligner. Since the fabrication process for the in-house amplifier production has been developed from scratch, we proceed with all required calibrations which were executed to reach a reliable recipe. Because of the complications that appeared constantly throughout the process development, the fabrication was prolonged and in the end the devices were fabricated at the place where they were originally developed: Karlsruhe Institute for Technologies (KIT). However, the problems are worth mentioning, together with some ways how to possibly combat them.

### 3.1 Optical lithography

The light-sensitivity of some materials is the foundation of photo-lithography[49]. Such materials are called *photoresists*, which consist of long-chained polymers. Upon exposure to a certain wavelength, usually in the near-UV spectrum, the resists change their chemical composition, resulting in different solubility of the exposed and unexposed parts in a specific chemical called developer. Depending on that, we can distinguish between two types of resist: negative and positive. In the positive resist the exposed part is developed while in the negative resist the exposed part stays on the wafer. One should note the existence of an image-reversal resist, which can be used as both positive and negative. This allows us to pattern an arbitrary structure onto the resist.

The fabrication of the amplifiers involved the use of a positive resist and the basic process is shown in Fig. 3.1.1. From left to right, the substrate of choice is spin-coated with the resist and then baked to evaporate the solvent contained in the resist. The sample is then exposed with the wavelength the resist is sensitive to with a proper energy dose. Usually, a dose test is required and the doses vary significantly for different patterns. As a last step, the sample is put into a developer, where the exact type of developer, the dilution rates (if required) and the development times are usually taken from the data sheet and slightly altered according to the required results. In this way, we obtain a certain design created by the resist on the substrate which can be further processed.

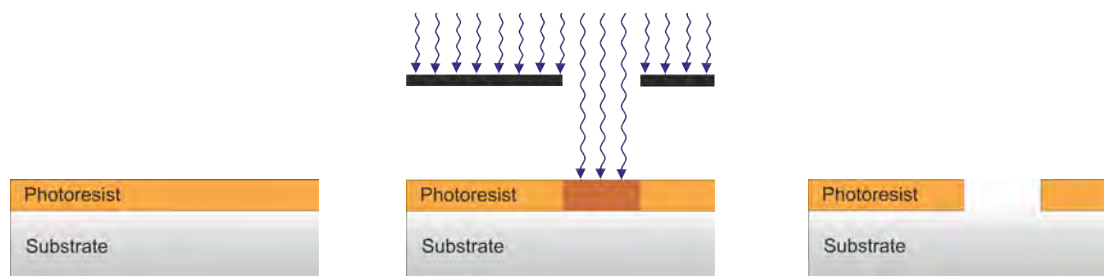


**Figure 3.1.1: Optical lithography with positive resist.** From left to right: a substrate is coated with resist and baked, the sample is then partially exposed with near-UV light. The exposed areas are then dissolved while the unexposed areas remain.

Two main systems are usually exploited in research clean rooms to expose the photoresist: laser writer and mask aligner. We will now discuss their working principle and specificities. The laser writer uses the on/off state of a focused laser, usually a diode laser[13]. The laser goes through the substrate area pixel by pixel and creates the pattern loaded in the software. The mask aligner uses transparent materials with opaque patterns on top, called masks, which can be produced with laser writer technologies. The provided mask is placed onto the sample and a parallel light from a mercury vapor lamp exposes the whole area at once with the light going through only the transparent parts of the mask. Both technologies have their advantages and disadvantages, e.g. the mask aligner is fast and reliable, but the laser writer is flexible regarding designs.

The fabrication in the clean room facility of QNTZ utilizes a laser writer from *Microtech* equipped with a 405 nm laser with a maximum resolution of 0.8  $\mu\text{m}$  or better depending on the resist. The resist chosen for the process is *AR-P 5350*[50] from *Allresists*. The profile of the resist as exposed by the laser writer can be seen in Fig. 3.1.2. We can observe that this resist possesses a undercut profile suited for lift-off processes. The choice of the resist was made to fit the exposure technology since the required flood exposure[51] for image-reversal resists is not supported by the laser writer and inverting the design to be suitable for negative resists would prolong the exposure time leading to probable stage drifts. Another advantage is that the recommended developer barely etches aluminum, in contrast to *TMAH*-containing developers.



**Figure 3.1.2: Resist with undercut profile: expectations vs. reality.** A schematic of a resist with undercut profile (left), where the developed area looks like a trapezoid. Instead, a real undercut profile (right) has rounder edges. The SEM picture shows a cleaved sample viewed under a 90° angle with silicon substrate and *AR-P 5350* resist, whose profile is false colored in orange for clarity.

## 3.2 Lift-off

There are two ways to proceed after the lithography: either with etching into the substrate or a metal film deposited before the lithography, or with lift-off. Only the lift-off will be discussed here as a main step in the amplifier fabrication. The basic lift-off process is shown in Fig. 3.2.1. A metal is evaporated on top of the developed resist. In the subsequent actual lift-off the resist is removed by putting the sample in a solvent. This strips away the resist from the substrate leaving behind metal structures covering the parts that were unprotected by the resist.



**Figure 3.2.1: Lift-off.** After the resist has been developed, a thin film of metal is evaporated on top (left). During the lift-off the leftover resist is removed leaving just the patterned metal structures of the substrate (right).

The illustration makes it obvious to see why undercut resists are favoured for reliable lift-off processes. The metal deposition via evaporation is very directional but the sidewalls will be always coated in case other resists are used. This could lead to problems during the lift-off, leaving the structures from the sidewalls, often referred as "wings", "ears" or "fences", attached to the film. Upon another metal deposition on top, these wings might interrupt the second layer (see Section 3.4).

## 3.3 Amplifier fabrication

Once we gained some insight on how optical lithography and lift-off work, understanding the whole process for amplifier fabrication is crucial for proceeding with this chapter. For this purpose, we utilize a two-step optical lithography process. A simplified version of this process can be found in Fig. 3.3.1. Once the first layer, including most of the structures forming the SQUIDs, the transmission line and the central capacitor, is patterned and developed, the sample is prepared for aluminium deposition by being loaded in the load lock of an electron beam evaporator *Plassys MEB550S* which is pumped to high vacuum. The sample is then cleaned with a plasma mix of argon and oxygen, where the argon is mainly used for charging the oxygen plasma. This cleaning step is called plasma descum and removes thin residual organic layers left over after the development (scum). The chamber is then pumped and a gettering process follows in which titanium is evaporated with the shutter closed. In this step, the titanium is exploited for sorption of leftover molecules in the chamber which enhances the sticking between the metal film and the substrate. Finally, an aluminium layer is deposited under zero angle. For better uniformity, the stage on which the sample is mounted is rotated during both descum and metal evaporation.

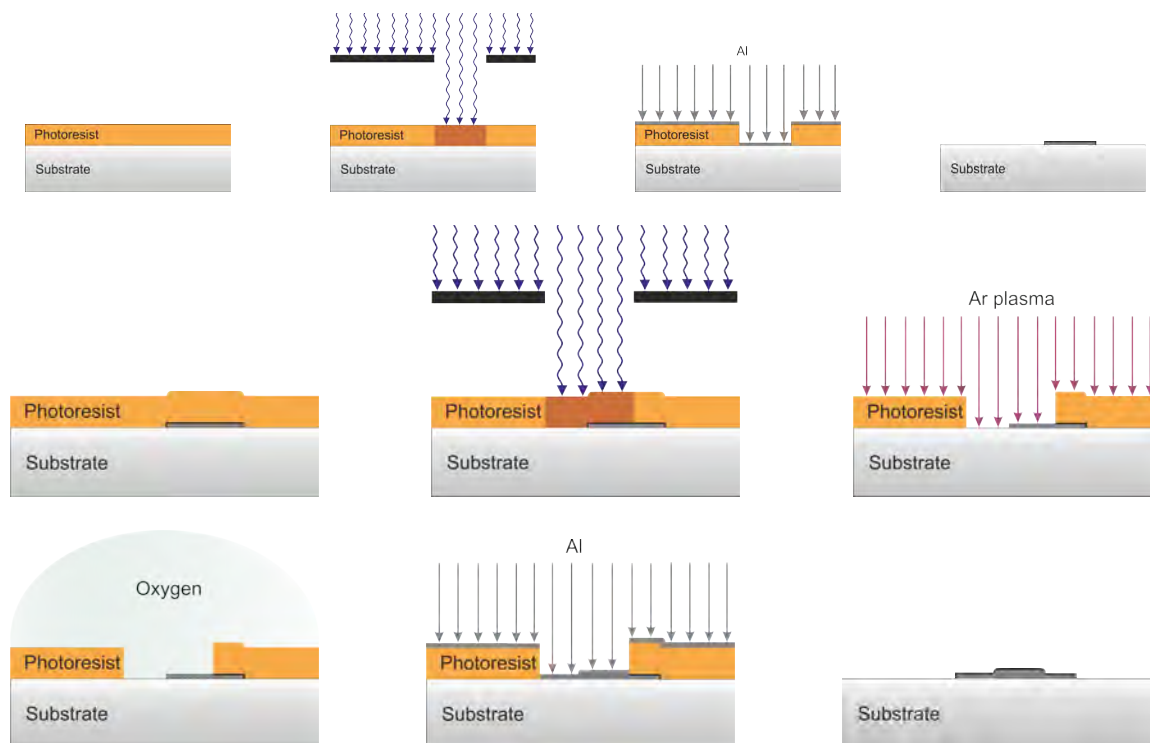


**Figure 3.3.1: Schematic of a simplified two-step process for Al/AlO<sub>x</sub>/Al junction fabrication.** The first row represents the first layer including exposure, development, evaporation and lift-off. The rest illustrates the second layer fabrication including the following steps from left to right: spinning the resist, exposure, development and plasma etching of the native oxide layer, controlled static oxidation, metal deposition and lift-off.

After evaporation, we proceed with the lift-off by placing the wafer in a beaker with a resist-removing substance, which can be acetone or a special remover as recommended in the data sheet of the resist. What should be left at the end are aluminum leads, resembling the amplifier. Yet, we need a second layer to form the tunnel junctions. The lithography process is similar, although care needs to be taken for aligning the two layers, special aligning marks are required for the two-layer processes. Moreover, there are usually drifts for long distances, due to the lack of interferometric stabilization of the stage, that need to be taken into account.

Once developed, the sample is ready for the evaporation of the second layer. This time the descum is skipped to avoid further oxidation of the aluminium leads and instead we proceed to the *Ti* gettering. Aluminium forms an uncontrolled oxide layer due to the atmosphere exposure. Because of its chemical and thickness variability we remove it with the aid of an argon milling process[52]. This time we use pure argon plasma, where the argon removes the oxide via momentum transfer.

There are two ways for creating the barrier in the tunnel junction: via static or dynamic oxidation. While the former oxidation is performed by fixing the oxygen partial pressure in the chamber, in the latter case a constant oxygen flow is used. We use static oxidation while varying the time and pressure in order to achieve the desired critical currents. However, there have been studies that dynamic oxidation can improve the critical current variation from wafer to wafer and also within a single wafer[53]. Aluminum evaporation follows immediately after the oxygen has been pumped away with the second

layer being slightly thicker to ensure good contact. During both milling and evaporation the sample holder is rotated. After a second lift-off the sample is almost ready. An optical microscope image of a device fabricated with laser writer technology on silicon can be seen in Fig. 3.3.2.



**Figure 3.3.2: Finished amplifier device with  $N = 1800$  fabricated on silicon in QNTZ.** From left to right: on-chip microstrip, SQUID array, coupling capacitor, SQUID array, ground plane.

In order to provide a well-defined ground plane for keeping the lead capacitance to ground  $C_0$  constant along the array, a 200 nm thick layer of silver is evaporated on the backside of both wafers (details in App. C). To prepare the sample, a thick protection layer of resist is spun on top of the amplifiers and baked at low temperature. The wafers are then mounted upside down in the Plassys. Similarly to the first layer, the recipe includes descum and  $Ti$  gettering. The additional step is the evaporation of 5 nm of  $Ti$  to enhance the sticking of the following silver layer. After this process, the wafers are diced into individual chips and then cleaned from the resist.

### 3.3.1 Design considerations and fabrication calibrations

Although the design for the DJJAA was readily provided by KIT, it is worth stressing the importance of several parameters when developing such a device. As already mentioned, increasing the number of SQUIDs dilutes the non-linearity, yielding higher dynamic ranges. However, one needs to take several other parameters in consideration: the central capacitor and the coupling rates. As a rule of thumb, the array length scales linearly with the central capacitor, where for the used interdigitated capacitor we adjust the capacitance by the length and the number of the fingers, rather than changing the gap. In addition, increasing the array length lowers the coupling rates which has a negative influence on the instantaneous bandwidth. Therefore, a trade-off needs to be found. In general, the lower modes have higher coupling rates and the resonant frequencies scale inversely with the number of SQUIDs in the amplifier.

With these design consideration, we can proceed with the parameters that are solely fabrication dependant. In order to achieve the desired frequencies where amplification appears, the critical current needs to be picked accordingly. For tunnel junctions, it can be achieved by changing the junction size or adjusting the resistance via the tunnel barrier. The Ambegaokar-Baratoff relation[54] gives an estimate for the

critical current from the normal state resistance  $R_n$

$$I_c(T) = j_c(T)A = \frac{\pi\Delta(T)}{2eR_n} \tanh \frac{\Delta(T)}{2k_B T} \underset{T \rightarrow 0}{=} \frac{\pi\Delta(0)}{2eR_n} \quad (3.3.1)$$

where  $j_c(T)$  is the critical current density,  $A$  - the junction area, and  $\Delta(T)$  is the temperature dependant energy gap of the superconductor. According to BCS theory, it is related to the critical temperature  $\Delta(0) = 1.76k_B T_c$ [40], where for thin film aluminum  $T_c = 1.4$  K.

Since the resistance is measured at room temperature, but the normal state resistance is defined just above the critical temperature, the conversion is executed via  $R_n = 1.15R_n(T_R)$ , where the scaling factor is determined experimentally[19]. Another consideration to be made is the additional contribution to the resistance from the aluminum leads. The lead resistance is given by

$$R_l = \rho \frac{L}{Wt} \quad (3.3.2)$$

with  $L, W, t$  being the length, width and thickness of the film, respectively, and  $\rho$  - the resistivity of the material. When subtracted from the total resistance, the obtained value represents only the room temperature resistance of the junction(s).

Another common way to take the lead resistance into account is by using the so-called *sheet resistance*  $R_{\square}$  as the resistance of square sheet of metal ( $L = W$ ). For the DJJAA parameters we have  $R_{\square, Al} = 1.1 \Omega/\square$  and there are six such sheets belonging to each SQUID, meaning that in order to extract the bare resistance of all SQUIDS in the amplifier, we use the following expression

$$R_{SQUID} = R_n(T_R) - 6NR_{\square, Al} \quad (3.3.3)$$

where  $N$  is the number of SQUIDS in the measured device.

## Argon milling

Aluminum forms a native oxide layer of a few nanometers upon exposure to the atmosphere. However, the thickness and chemical composition of this layer varies greatly, rendering it unsuitable for reliable junction fabrication. Therefore, this layer needs to be replaced by a pure  $AlO_x$  layer with controlled thickness.

The insulating native oxide layer is removed with the aid of an argon ion beam with a radius of 2 cm, generated by a *Kaufman* ion source in the *Plassys*. The parameters for the source are chosen to sustain a stable ion beam. A first rough calibration was executed with a recycled sapphire wafer containing some *Al* wires. Thick drops of resist were placed on top of the wires and baked. The sample was subjected to 30 min of argon milling, after which the resist was removed with a solvent and the formed step was measured with a profiler. The milled amount added up to a milling rate of 0.8 nm/min. With this information and a rough estimate for the native oxide thickness of 2 nm, we would expect that the layer is removed after 2.5 min.

A precise calibration is required since the etching rate for aluminum is ten times faster[52]. We use JJAs constituted of ten  $5 \times 5 (\mu m)^2$  junctions in series milled for 2, 3 and 4 minutes. As a reference point, we create geometrically identical structures but evaporated in one step so no junctions are created, giving us the lead resistance.

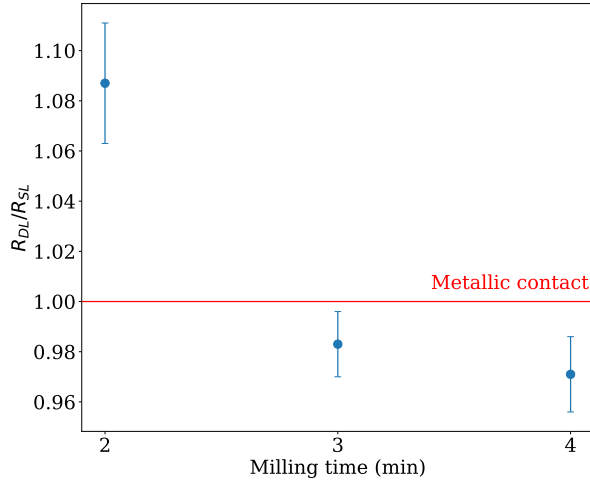


**Figure 3.3.3: Argon milling calibration.** The plot shows the resistance ratio between junction arrays fabricated with two-step lithography over the resistance of the same geometric structure evaporated within a single lithography step versus the time of  $Ar$  milling. The ratio of one marks the onset of metallic contact between the two layers.

The resistance of the two-layer chains are normalized by the single layer structure and plotted as a function of the milling time in Fig. 3.3.3. Indeed, we see metallic contact is achieved after between 2 and 3 minutes of milling time when resistance of the overlap contact disappears. The ratio goes lower than one as the milling widens the leads which reduces the sheet resistance of the two-layer structures with respect to the single-layer one. Notably, if extended to higher times, the thickness of the film will decrease due to milling into the aluminum, counteracting the effect of the lead widening on the resistance.

### Critical current density

The usual way for fitting the critical current to the desired value is to fix the critical current density with the oxidation parameters and vary the junction area to adapt the current precisely. Note that, a reliable fabrication without shorts in the oxide layer sets an upper limit on the critical current density. The lower limit on the critical current density is set by the self-limiting nature of the controlled growth of  $AlO_x$ [55]. Similarly to the native oxide, the controlled oxide-layer growth saturates.

For the calibration we use JJAs comprising of 10 junctions in series as test structures. The total number of arrays is ten: five with junction size  $5 \times 5 (\mu m)^2$  and five with  $10 \times 10 (\mu m)^2$ . From the resistance measurements the critical current is extracted. The sheet resistance is taken into account by subtracting the resistance of the single layer analogues placed on the same chip. Due to the lithography process junction areas come out  $1 - 2 (\mu m)^2$  bigger than designed which is measured under an SEM. The critical currents are then normalized to the real junction area, giving the final values for the densities.

In Fig. 3.3.4, we have extracted four different densities by varying the oxidation parameters. Similarly to the  $Nb/AlO_x/Nb$  tunnel junctions[56], it is evident that the density has a power-law dependence on the product of the oxidation time and pressure. The target value of  $154 nA/(\mu m)^2$  would result in  $I_c = 5 \mu A$  for the amplifier SQUIDs, yielding many dimers in the range 1 – 10 GHz. The parameters coming closest to this value are  $t = 6$  min and  $p = 30$  mbar. Both the rising and falling times for reaching the

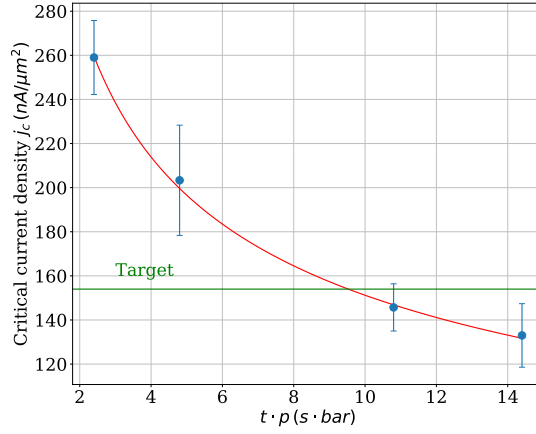


**Figure 3.3.4: Critical current density calibration.** The critical current density (blue) as calculated from the Ambegaokar-Baratoff formula 3.3.1 as a function of the oxidation time  $t$  and pressure  $p$ . The points are fitted with a power law function  $a(t \cdot p)^b$  (red), where the resulting fitting parameters are  $a = 362(8)$ ,  $b = -0.38(1)$ . The target value (green) is the critical current density for which  $I_c = 5 \mu\text{A}$  for the SQUIDS in the amplifier.

respective pressure and pumping back to high vacuum are included in  $t$ .

## Junction aging

The tunnel junction barrier changes over time and this process is called *junction aging*. As a consequence, the resistance grows. The main culprits for this are two phenomena[57]: diffusion of oxygen from the barrier to the electrodes and chemical change of the barrier itself due to absorption and/or desorption of atoms and/or molecules different than oxygen. It is believed that the second mechanism dominates in the process of aging while the first is only noticeable on long time scales. Additionally, the oxide starts crystallizing in contrast to its usual amorphous structure.

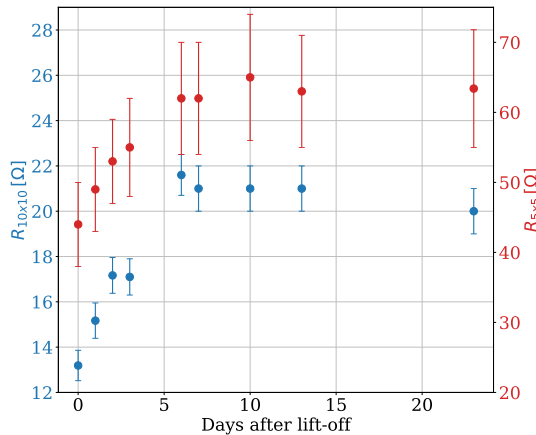


**Figure 3.3.5: Junction aging.** The resistances of JJAs consisting of 10 junctions each have been observed over the span of 24 days. There were two types of arrays, five from each type, depending on the junction size:  $5 \times 5 (\mu\text{m})^2$  (red) and  $10 \times 10 (\mu\text{m})^2$  (blue).  $R_{5 \times 5}$  and  $R_{10 \times 10}$  are the averaged resistances over the five arrays, where the subscript denotes the junction size.

The calibration for the critical current density cannot be executed without knowing first how long it takes for the junction resistances to settle down. For this we took the sample from the previous calibration with oxidation parameters  $t.p = 14.4 \text{ s.bar}$  and observed the resistances over the span of 24 days (see Fig. 3.3.5). We found out that the junctions age between 43 – 62% of their initial resistances, where the higher value corresponds to the bigger junction area. After approximately 6 days, the junctions are settled, giving the correct information to proceed with other calibrations.

## 3.4 Troubleshooting

A big part of this work was dedicated to overcoming fabrication problems arising constantly during the process development. Despite the promising start, several months into the development sticking issues started appearing, as shown in Fig. 3.4.1a, rendering our initial recipe unreliable. Step-by-step we started excluding the possible reasons. The first suspicion was that the undercut is too big, making the structures mechanically unstable. After a discussion with the resist producer, the baking temperature was increased by  $3^\circ \text{C}$  in order to reduce the undercut, but the results were unsatisfactory since the problems persisted.

Because of technical limitations the resist was stored at room temperature which is higher than recommended according to the data sheet. The suspicion of premature aging of the resist due to the improper storage was dropped when a newly opened bottle of resist gave similar results in terms of adhesion. However, in order to delay this process, the resist was moved to a refrigerator at  $5^\circ \text{C}$  imposing a certain thermalization time before the lithography until the dew point is passed. Otherwise, if water condensates on the surface, the resist needs to be thrown away. Another reason for this extra step is that the viscosity of the resist in general changes with the temperature resulting in different thickness of the resist film, which alters the lithography process. When stored at colder temperature, the light-sensitive substance might precipitate on the bottle, making the stirring while thermilizing essential for the quality of the lithography.

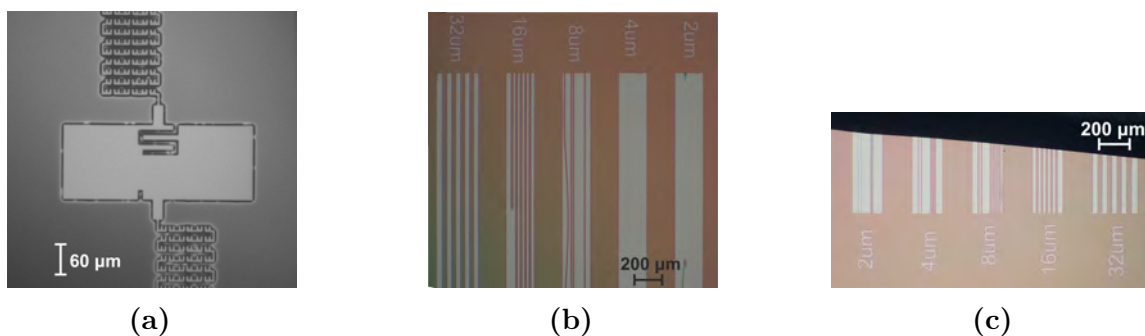


**Figure 3.4.1: Sticking problems.** Optical images of developed samples (a) without pretreatment, (b) with prebaking at  $200^\circ \text{C}$  for 5 min, and (c) with  $\text{O}_2$  RF plasma cleaning for 400 s. In (a) the first appearance of this problem in a DJJAA sample is illustrated. The pattern in (b) and (c) was developed specially for a sticking test.

For the sticking test a special pattern was designed, including long ridges of resist with varying well-defined widths, spaced differently. Such structures are extremely sensitive to sticking issues. The ridge length of 5 mm was chosen for easier cleaving

through the lines on the sample for imaging purposes. Five of the ridges with widths 2, 4 and 6  $\mu\text{m}$  were positioned close to each other and two were standing far away from any other structures to ensure that proximity effects are taken into account. All 16 and 32  $\mu\text{m}$  wide lines were spaced equally separated by their respective widths.

For good adhesion, photoresists need *hydrophobic* surfaces. The following step was to exclude the excessive humidity causing inferior adhesion. Due to the capacity of the dehumidifier in the clean room, the room humidity depends on the outside conditions. An optimum of 40% relative humidity is required. A sample was prebaked at 200 °C for five minutes and then left for a moment to thermalize before the resist was spun. The lithography result is shown in Fig. 3.4.1b. From the resist ridges only the 32  $\mu\text{m}$  lines consistently survived during the development. To verify that humidity was not the main reason for the bad resist adhesion, two runs of fabrication with high and low humidity were made. Both of them resulted in the resist peeling during the development, but this test was inconclusive due to the possibility of different handling of the testers. To completely exclude humidity as the main cause of the inferior adhesion, a change of the dehumidifier of the clean room is necessary to achieve a constant relative humidity.

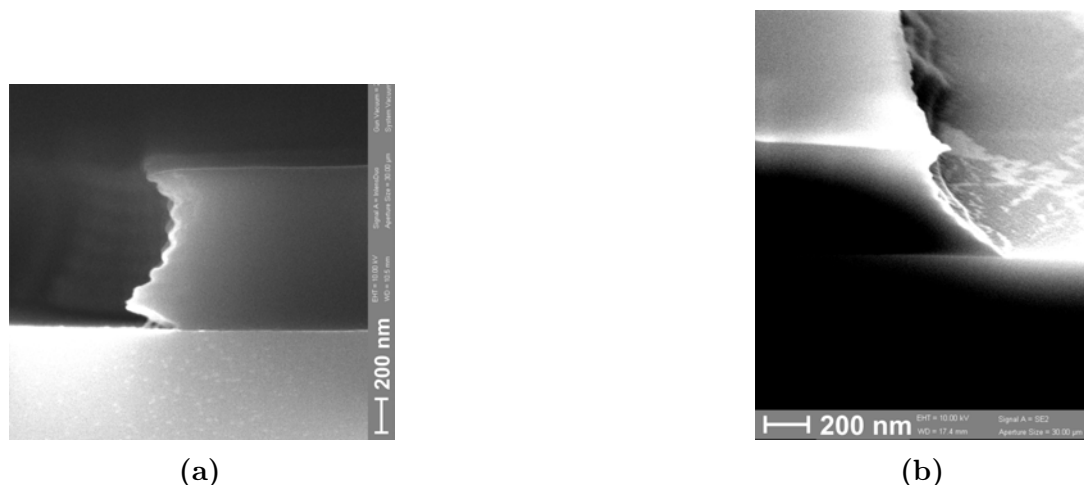


**Figure 3.4.2: Resist profiles with different pretreatment.** SEM images of developed and cleaved samples (a) with prebaking at 200 °C for 5 min, and (c) with adhesion promoter *AR 300-80*.

An additional step of  $O_2$  RF plasma cleaning in the *Sentech ICP SI 500* was incorporated immediately before spinning the resist, temporarily solving the sticking issues (see results in Fig. 3.4.1c). Unfortunately, with time the cleaning time and powers needed to be gradually increased in order to achieve the same results as initially obtained. The last resort was to use an adhesion promoter *AR 300-80* as recommended in the data sheet.

Although this solved the sticking problems, due to the additional incorporated chemical and the changed interface with the substrate, a big part of the recipe needed to be adapted including the doses and the development time. In Fig. 3.4.2 one can see the difference of resist profiles depending on the pretreatment. Only the prebake is insufficient for good sticking, the resist starts peeling, making the patterned structures mechanically unstable. On the other hand, the sample with adhesion promoters shows perfect sticking properties, but the resist profile is not suitable for lift-off anymore.

If, however, the recipe is not adapted and aluminum is deposited on top, the walls of the resist are covered as Fig. 3.4.3a shows. In general, during lift-off those parts

remain, forming "wings" which point upwards. Upon second layer evaporation, these wings can cause discontinuities in the upper layer (Fig. 3.4.3c) making the resistance readings untrustworthy. Unexpectedly high resistances are a sign of such problem. If the exposure doses and development times are adapted, an undercut resist profile can be achieved (Fig. 3.4.3b), yielding clean edges and a continuous second layer (Fig. 3.4.3d).

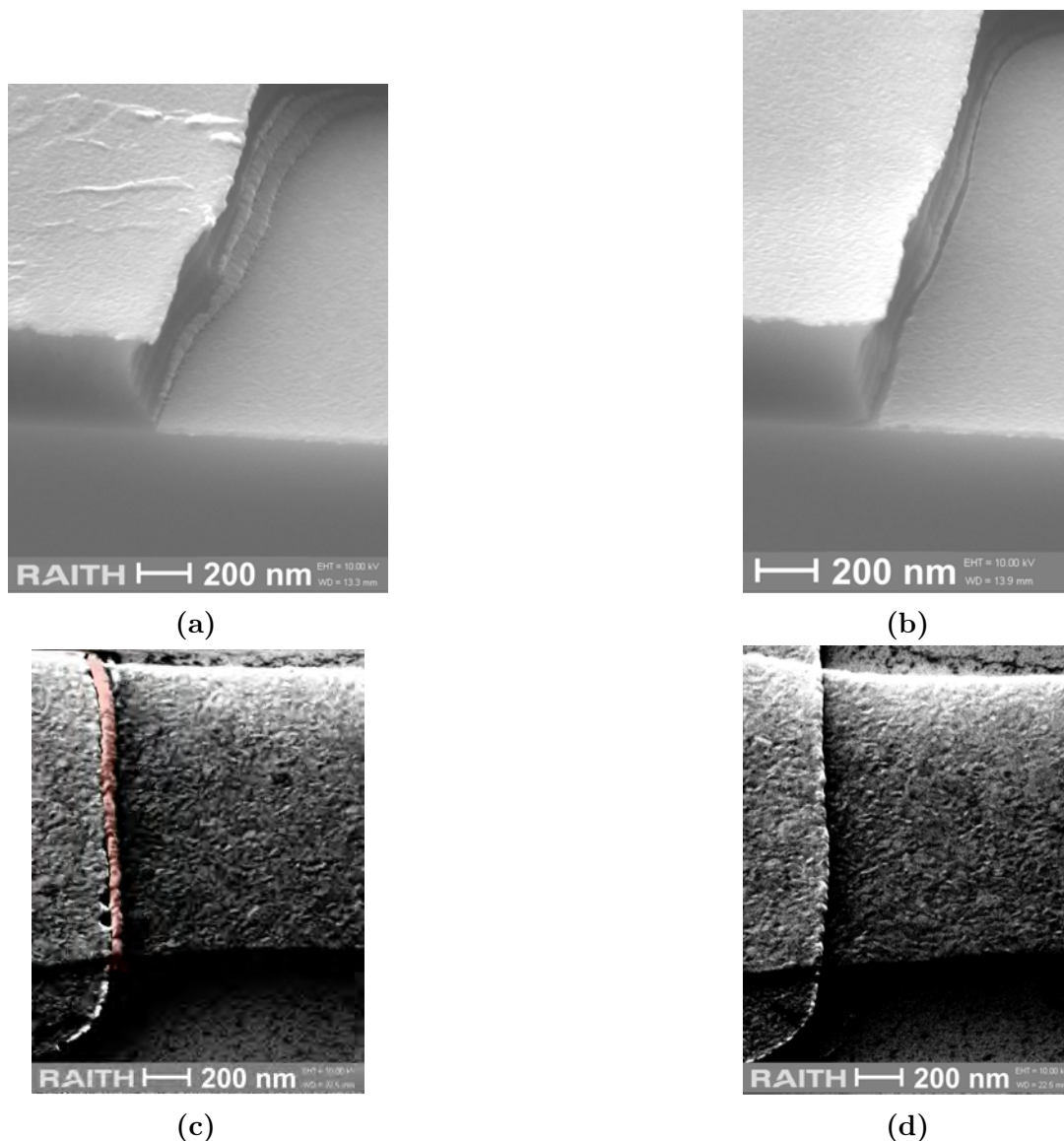


**Figure 3.4.3: SEM images of samples with wrong and right resist profiles.** (a) and (b) Exposed, developed and evaporated samples before lift-off; (c) and (d) The resulting junctions. The first column presents an example for a wrong resist profile (a) where the sidewalls of the resist are covered with Al. The lift-off would result in "wings" which may interrupt the second layer of the junction. Not well defined junction edges, as highlighted in red color in (c), are a clear sign of such wings. The right column illustrates a sample with good resist profile (b), yielding a continuous second layer (d).

The increased doses lead to other problems with overexposure of some SQUIDs, changing their loop area. This could be avoided by rotating the pattern by 90 degrees so only leads are overexposed and not SQUIDs. Despite the good progress in combating the appearing issues, the final fabrication was moved to KIT owing to time limitation. The

final fabrication processes in both facilities can be found in Appendix C.

A suggested improvement for the in-house fabrication is incorporating a dehumidifier with a higher capacity to eliminate any possible problems connected to humidity. Perhaps switching to other photoresist process, e.g. negative/image-reversal resists if flood exposure is supported, would be beneficial since negative resists are known to have excellent adhesion to silicon, compared to fair adhesion of positive resists[51]. Moreover, negative resists have natural undercut in contrast to the positive resists where complex chemistry is involved to achieve the undercut. Developing a bilayer process would be another way for fabricating DJJAAs.

# Chapter 4

## Experiment

In the span of this thesis, the properties of two amplifiers were investigated. This chapter provides the general information on those devices and the experimental apparatus used for determining their properties (see next chapter). It can be split in three main parts. The first section focuses on each DJJAA, giving some details on assembling the finished device. The next section describes the experimental setup and gives an insight on Y-factor measurements and their application in a multi-stage amplification chain. In the final part, the reader can find the calibrations of the setup which are later used in the experimental results.

### 4.1 Devices, sample holder and PCB

Two devices were investigated in this work. The first one, to which we will refer as *DJJAA1*, has  $N = 1400$  SQUIDs while the second one, *DJJAA2*, has  $N = 1700$  SQUIDs. The chips with size  $7.5 \times 3.6 \text{ mm}^2$  belong to two different wafers with slight differences in the fabrication, particularly in the ultrasonication time during the lift-off of the second layer. Those chips were chosen so the asymmetry factor  $m = \frac{R_{in} - R_{gnd}}{R_{in} + R_{gnd}}$  of the normal resistances of the array between the input and the central capacitor  $R_{in}$  and the array between the central capacitor and the ground plane  $R_{gnd}$  is smaller than 2% to ensure good hybridization.

The chips are embedded in a copper sample box, a picture of which can be found in Appendix D. The microwave connection between the transmission line on the chip and the SMA connector is created by a printed circuit board (PCB) with a patterned microstrip transmission line, manufactured by our electrical workshop. For the PCB *RO3003* panel from *Rogers Corporation* was used with a  $508 \mu\text{m}$  thick dielectric material with relative permittivity  $\epsilon_r = 3$ , enclosed between two  $35 \mu\text{m}$  copper sheets. A dedicated slot for the chip is created in the PCB. The bottom sheet remains on the panel and serves as ground plane. Meanwhile, the top is split in two parts: half of the metal sheet is removed, leaving behind only a transmission line, while the other half remains to connect the ground plane of the chip. To electrically connect the top ground to the bottom vias (through-plated holes) are used, avoiding stray modes between the plates.

The microstrip is soldered from the outer side of the PCB to the center pin of an SMA connector. The pin and the microstrip must have similar widths do avoid reflections, hence the choice of the panel used. The board with the connector is glued with silver epoxy to a copper sample holder, made in-house by our mechanical workshop,

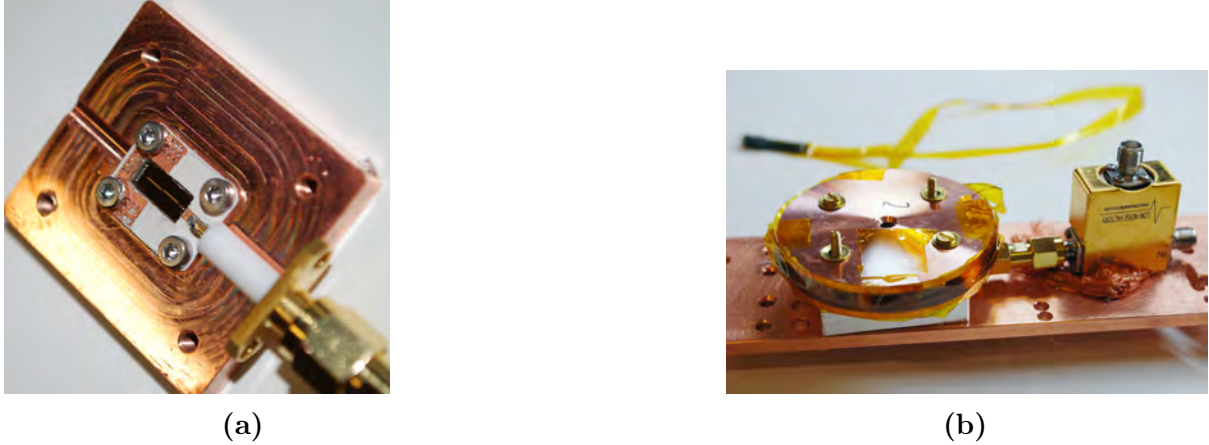


**Figure 4.1.1: Assembled amplifiers.** (a) The PCB and chip are glued with silver epoxy to the bottom part of the sample holder and bonded to each other. The microstrip on the PCB is soldered to an SMA connector, forming the input port of the amplifier. (b) The sample box is closed and a coil is installed on top. The box is wrapped on the sides with aluminum tape to cover the edges for isolation. The coil is taped with kapton to protect the wires. Finally, a circulator from *Low Noise Factory* is attached directly to the DJJAA.

and additionally secured with four screws. Once completely dry, the chip is also glued and left to dry. The on-chip microstrip is then wire-bonded to the PCB transmission line with *Al* wires, their ground planes are also bonded together. A picture of the device at this point of the assembling can be found in Fig. 4.1.1a. The height difference between the chip and the PCB is less than  $200 \mu\text{m}$  ( $t_{\text{chip}} = 330 \mu\text{m}$ ) and is not compensated. Note that the aluminum transmission line (chip), the copper microstrip (PCB) and the SMA connector are all matched to  $50 \Omega$ .

In order to tune the resonant frequencies of the amplifiers, each sample holder is equipped with a coil on top of the lid. The coil is designed to obtain a homogeneous magnetic field over all SQUIDs in the DJJAA and the windings are picked to achieve one to two flux quanta through the loops without heating the fridge with high currents (typical values do not exceed 1 mA). To separate the input from the output fields, a commercial 4 – 12 GHz circulator is attached directly to the SMA port (see Fig. 4.1.1b), thus hindering the creation of standing waves in the measurement band.

## 4.2 Setup

Once fully assembled, the sample holders are mounted to the base plate of a dilution refrigerator from *Oxford Instruments*. They are enclosed in a magnetic shield can with several protective layers of niobium and mu-metal. Two lines are connected to each circulator, one for input and one for output. The outputs lead to a microwave switch, which allows performing radio-frequency calibrations. The total number of used input lines are 3: two of them address the amplifiers and the third one goes directly to the switch without a sample in between. There are six different ports incident on the switch, where two loads, two DJJAAs and the aforementioned input line are connected. The switching is achieved via DC pulses. Another set of DC lines with a DC–5 kHz filter are

connected to the coil. The wires are twisted to avoid picking up stray fields.

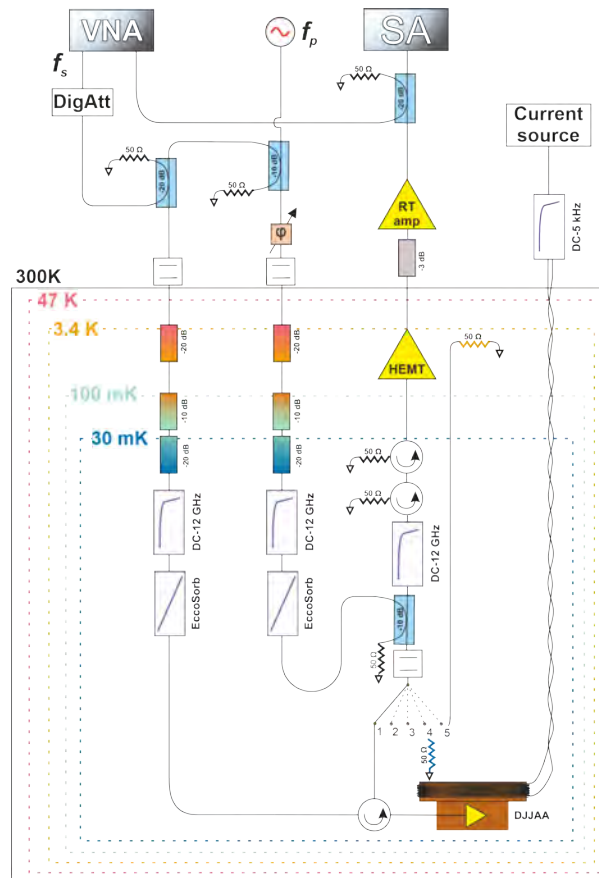


**Figure 4.2.1: Schematic of the measurement setup.** The abbreviations are as follows: VNA - Vector Network Analyzer, SA - Spectrum Analyzer, DigAtt - digital attenuator, HEMT - High-Electron-Mobility Transistor (low-noise cryogenic amplifier), RT amp - room temperature amplifier. At the free inputs of the switch an input line without a sample and another DJJAA are connected but not shown in the figure. The DC lines for the switch control are also not illustrated.

The full setup is illustrated in Fig. 4.2.1. The signal is generated by a Vector Network Analyser (VNA) and its power is adjusted via a digital attenuator (DigAtt). A following directional coupler combines the signal connected to the  $-20$  dB port with the pump as generated by a signal generator. The signal then goes through a DC block, filtering any DC offset, and into the fridge. The apparatus outside the fridge is fixed, by connecting different input lines in the fridge and turning on the corresponding switch port, one can address the different devices. Several attenuators thermalize the input field to the temperature of the plate to which they are fixed. After going through several filters, low-pass to filter high-frequency noise and EccoSorb filtering infrared radiation, the input signal finally reaches the sample through a 4 – 12 GHz circulator.

After being reflected, the signal is deflected by the circulator to the switch, then passing through another DC block, a  $-10$  dB directional coupler for pump cancellation, a low-pass filter and two isolators, which are essentially circulators with one terminated port used for blocking the thermal radiation back to the sample. Up to this point, all elements on the line are associated with attenuation. In order to make the signal detectable again, we use two amplifiers: a High-Electron-Mobility Transistor (HEMT) at the 4 K stage and

a room temperature amplifier (RT amp). The  $-3$  dB attenuator in between is placed to avoid the saturation of the latter amplifier and to diminish standing waves due to poor amplifier matching. The output signal is then split by another  $-20$  dB directional coupler with the coupled port connected to the VNA, while the transmitted wave is detected by a Spectrum Analyzer (SA) which allows measuring transmission and power emission simultaneously.

## Pump cancellation scheme

A pump cancellation scheme has been implemented by placing two  $-10$  dB directional couplers, one between the DC block and the low-pass filter on the output line and one outside the fridge, just after the signal generator. The pump is split with the coupled port going directly in the fridge while the transmitted port is connected to a mechanical phase shifter. This part of the pump is used for the cancellation and is sent into the fridge by another input line, directly connected to the coupled port of the second  $-10$  dB directional coupler. In this way the attenuation is roughly matched once the two pump tones are combined, leaving the phase difference between them as the main knob to turn. They cancel each other before reaching the HEMT. The essential role of the pump cancellation is to avoid saturation of the consecutive amplification stages by the strong pump. Notably, if the pump cancellation is not used, the directional coupler splitting the pump is removed and the microwave generator is directly combined with the signal tone.

### 4.2.1 Noise characterization

The basic equations describing the behavior of a single bosonic mode passing through a linear amplifier were already derived in Section 2.1.2. However, we need to consider our limited frequency resolution and accuracy in practice. In fact, what we measure is a power spectral density (PSD) with a precision set by the resolution bandwidth. Therefore, we can generalize Eq. 2.1.5 as

$$S_{out}(f, T) = G(f)(S_{in}(f, T) + S_{add}(f, T)) \quad (4.2.1)$$

where  $S(f, T)$  is generally temperature and frequency dependent and has units W/Hz. In order to obtain this density for our setup, the raw noise power as measured by the SA needs to be normalized by the resolution bandwidth used in the measurement. Notably, other spectrum analyzers can perform this normalization automatically. The subscripts denote the input, output and added spectral densities.

For noise characterization we use a common *Y-factor* technique[9, 58, 3] relying on two matched loads thermally anchored at different temperature stages.  $Y$  is the ratio of the measured noise power at the output with the input connected to the hot load versus the input connected to the cold load. A  $50\ \Omega$  load at fixed temperature behaves as a blackbody, which not only absorbs the incident radiation but also emits thermal noise. There are many ways to derive the power spectral density of a blackbody[30], one of which can be found in Appendix E, but they all lead to the same result. For a matched load the power spectral density (PSD) can be written as:

$$S_e(f, T) = \frac{hf}{2} \coth\left(\frac{hf}{2k_B T}\right). \quad (4.2.2)$$

The expression is known as generalized Nyquist noise and it includes the zero point fluctuations. Since we can predict the power spectrum if the temperature is well known, such a matched thermalized load is well suited as a calibrated noise source ( $S_{in}(f, T) = S_e(f, T)$ ).

Usually, if the noise power is weakly dependant on frequency in the bandwidth of interest, the noise source can be modelled as equivalent thermal noise source at temperature  $T_N$ . Typically this characteristics, referred as *noise temperature*  $T_N$ , is quoted for commercial amplifiers like the ones used in the amplification chain of the measurement setup. Therefore, in order to determine the noise temperature of our amplification chain, we can approximate its added PSD from Eq. 4.2.1 as  $S_{add} = k_B T_N$ . Notably, the noise temperature is less suitable for parametric amplifiers because of their quantum nature being incompatible with the purely classical definition of  $T_N$ . Moreover, they posses highly frequency dependent noise. Instead, the spectral density is usually divided by  $hf$  yielding the noise in dimensionless units of noise quanta.

In our case, the  $Y$  factor is the ratio of the measured noise power at the output with the hot source "switched on"  $S_m(f, T_h)$  to the noise power with the cold source  $S_m(f, T_l)$  incident on the switch, both already normalized by the resolution bandwidth. Using the expression for the added spectral density and combining it with Eq. 4.2.1, we can extract the gain and the noise temperature of the whole amplification chain after the switch:

$$G(f) = \frac{S_m(f, T_h) - S_m(f, T_l)}{S_e(f, T_h) - S_e(f, T_l)} \quad (4.2.3a)$$

$$T_N(f) = \frac{S_e(f, T_h)S_m(f, T_l) - S_e(f, T_l)S_m(f, T_h)}{k_B [S_m(f, T_h) - S_m(f, T_l)]} \quad (4.2.3b)$$

where  $S_e(f, T)$  is the expected spectral density from Eq. 4.2.2 for the high and low temperature loads thermalized at  $T_h \approx 3.43$  K and  $T_l \approx 29$  mK, respectively.

## Multi-stage amplification chain

Once we have the information for the amplification chain, we can characterize the noise performance of the parametric amplifier of interest. For a two-stage amplification chain as illustrated in Fig. 4.2.2, at the output we will measure

$$\begin{aligned} S_{m,tot}(f, T) &= G_2(f) \{G_1(f)[S_{in}(f, T) + S_{1,add}(f, T)] + S_{2,add}\} \\ &= G_2(f)G_1(f) \left[ S_{in}(f, T) + S_{1,add}(f, T) + \frac{S_{2,add}(f, T)}{G_1(f)} \right] \end{aligned} \quad (4.2.4)$$

where the subscripts correspond to the amplifier position in the chain.

This equation reveals the importance of high-gain and low-noise amplifier as the first part of the chain since the predominant noise comes from it. All subsequent amplifiers will contribute to the gain but their noise will be reduced by the gain of the previous amplifiers.

For this particular setup as shown in Fig. 4.2.1, we consider the second part of the chain as the whole output line from the switch to the SA  $S_2 = S_{chain}$ ,  $G_2 = G_{chain}$ , while the first stage is just the parametric amplifier  $S_1 = S_{DJJAA}$ ,  $G_1 = G_{DJJAA}$ . Another assumption we make is that the input is well thermalized to the base plate temperature  $T_B \approx 29$  mK, meaning that in general  $S_{in} \ll S_{DJJAA,add}$  for the used frequency range. All

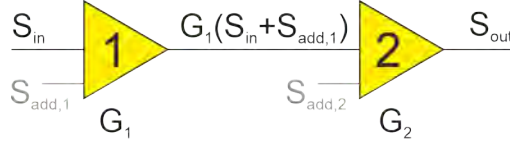


**Figure 4.2.2: Two-stage amplification chain.** For a chain of two amplifiers if the second stage is fully characterized and the input is known, we can determine the gain and the noise performance of the first stage. The frequency and temperature dependence are left out for clarity.

these assumptions lead to the final equation used in the experiment:

$$S_{m,tot}(f, T) \approx G_{chain}(f)G_{DJJAA}(f) \left[ k_B T_{N,DJJAA} + \frac{k_B T_{N,chain}}{G_{DJJAA}(f)} \right]. \quad (4.2.5)$$

Therefore, if we have the information for the amplification chain as deduced from the  $Y$ -factor measurement, we can measure directly  $G_{DJJAA}(f)$  and extract the noise of the investigated DJJAA.

## 4.3 Calibrations

A few measurements were made to characterise the experimental setup, excluding the parametric amplifiers. Using the  $Y$ -factor measurement scheme as already described, we can extract the gain and the noise temperature of the whole chain after the switch using Eq. 4.2.3. Such measurements require low video bandwidth (VBW) for smoothing the signal and thus reducing the noise while the resolution bandwidth (RBW) is picked to achieve reasonable measurement times while keeping the resolution sufficient for the chosen frequency range of [3.5, 12.5] GHz.

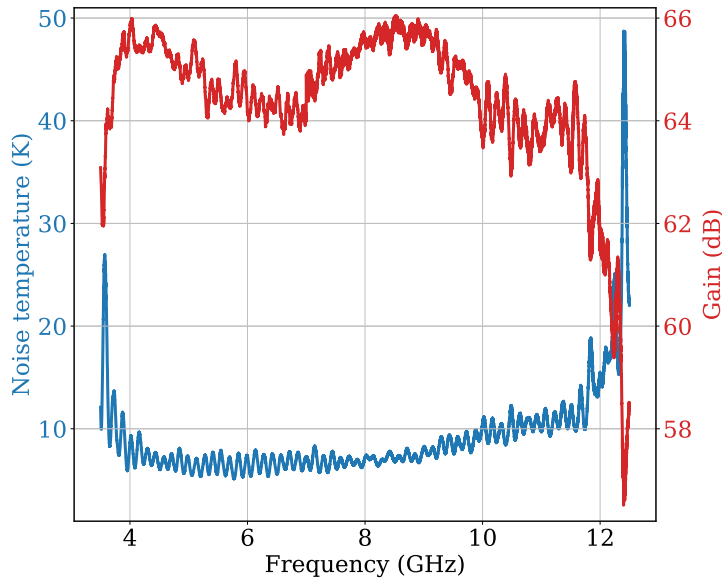


**Figure 4.3.1: Output characterization.** The gain and temperature of the amplification chain on the output are extracted from  $Y$ -factor measurement and plotted against the frequency.

For this purpose two measurements of the noise power are executed: with the hot load and with the cold load connected to the switch. Both of them are not averaged and the video and resolution bandwidths set on the analyzer are 10 Hz and 5 MHz, respectively. The noise powers are then manually divided by the resolution bandwidth to obtain  $S_m(f, T_h)$  and  $S_m(f, T_l)$ . The noise temperature and gain are plotted in Fig. 4.3.1.

The extracted gain is approximately 10 dB lower than the expected value of  $\approx 76$  dB because of the losses from the additional elements on the output line such as circulators, directional couplers, the attenuator etc. The gain plummets after 12 GHz and before 4 GHz because of the low pass filter and the working range of the HEMT[59] and the room temperature amplifier[60]. As already mentioned, the total noise temperature in a two-stage amplification chain is dominated by the first stage, namely the HEMT. However, the measured noise is significantly higher than the  $\approx 3$  K specified in the HEMT data sheet. This discrepancy can be explained from the additional attenuation from the microwave components and the cables before the HEMT which can accumulate up to 3 dB resulting in doubling the noise temperature. The rest  $\approx 1$  K can be attributed to the noise coming from the second amplifier and the attenuation from the other elements on the line.

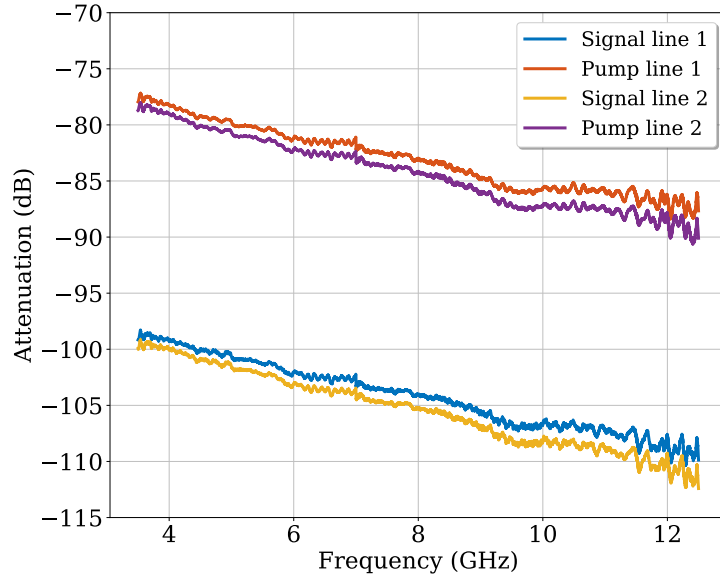


**Figure 4.3.2: Line attenuation.** If the gain chain is already characterized, we can obtain the attenuation along the lines, used for probing DJJAA1 (blue and red) and DJJAA2 (yellow and purple).

Thanks to the auxiliary feedline directly connected to the switch, we could measure the attenuation along the input lines with the VNA. Once the output line is completely calibrated, we measure all available input lines: two lines in the fridge each of which splits outside in signal and pump line. The gain from Fig. 4.3.1 is subtracted from the raw data in order to obtain the attenuation across the frequency range as plotted in Fig. 4.3.2. The difference of 1 dB between the lines for the two amplifiers comes from the length of the cables outside the fridge. Expectedly, the signal line for each amplifier lies approximately 21 dB lower than the respective pump line because of the directional coupler and the insertion loss from the digital attenuator. This information is essential for the calibration of the saturation power of the parametric amplifier. Keep in mind that because of the extra cabling on the DJJAA input line and the circulator, the actual powers that reach the sample are further attenuated by 1 – 2 dB more than the value

extracted from Fig. 4.3.2. This additional attenuation could be estimated by measuring the signal reflected by the amplifier and comparing it with the transmission without the amplifier.

# Chapter 5

## Experimental results

In this chapter the experimental results are presented and discussed. In the first part, three flux-bias points in the first dimer of DJJAA1 are fully characterized including flux tunability, gain-bandwidth product, saturation power and noise performance. Amplification is shown in all dimers of DJJAA2 and the respective added noise number is determined. Finally, for more accurate results a pump cancellation is implemented and the background radiation is analyzed.

### 5.1 Tunability

#### 5.1.1 Mode tunability through magnetic flux

When we probe the amplifier or any one-port device under test with a VNA, we measure the reflection coefficient  $\Gamma(\omega) = S_{11}(\omega)$ , namely the ratio between the outgoing and incoming voltages, while sweeping the probe frequency. The term  $S_{11}(\omega)$  is the first element in the scattering matrix, used to characterize multi-port systems. In general, the reflection coefficient is a complex number defined by a phase and an amplitude. Although not always revealed by the amplitude, the phase undergoes a  $2\pi$  phase roll in the vicinity of a resonance which makes their detection possible.

In order to determine the present resonances and confirm that they belong to the connected amplifier, we probe the devices while sweeping both the probe frequency and the external flux through the SQUIDs via the coil current. The power of the probe signal is low to remain in the linear regime. The reflection phase for *DJJAA1* and *DJJAA2* can be found respectively in (a) and (b) of Fig. 5.1.1. Their reflection magnitudes can be found in Appendix F. As expected, in both devices the resonant frequencies decrease when the external flux through the loops is increased because of the inductance dependence of the SQUIDs (Eq. 2.2.19). The maximal inductance, or so-called full frustration, is reached when  $|\phi_{ext}/\phi_0| \approx 0.5$ , these points can be used to convert coil current to flux quanta. Note that in both cases there is one more dimer below the measured frequency range but both couldn't be measured due to setup limitations. However, the dimer numbering will address only the mode doublets inside this frequency range.

While the map of *DJJAA2* (Fig. 5.1.1b) is very symmetric around zero current through the coil, the phase response of *DJJAA1* reveals peculiar features. The general response is shifted with respect to zero coil current due to the circulator, mounted in a way that its magnetic field threads the SQUID loops, causing this constant offset. Another

irregularity is the feature similar to an avoided crossing observed between the modes in the two higher frequency dimers. Its origin remains unknown. According to the simulations, the lowest frequency mode of the triplets does not belong to the amplifier. Since the box design is the same for both amplifiers, the coupling to a box mode is unlikely. However, the box of *DJAA1* was recycled still leaving some suspicion about it. Another possible source would be an unknown issue with the chip itself either in the substrate or the patterned structures. In any case, the triplet doesn't react to strong pump tones in the modes themselves or between pairs. Because of these observations, only the first dimer was investigated.

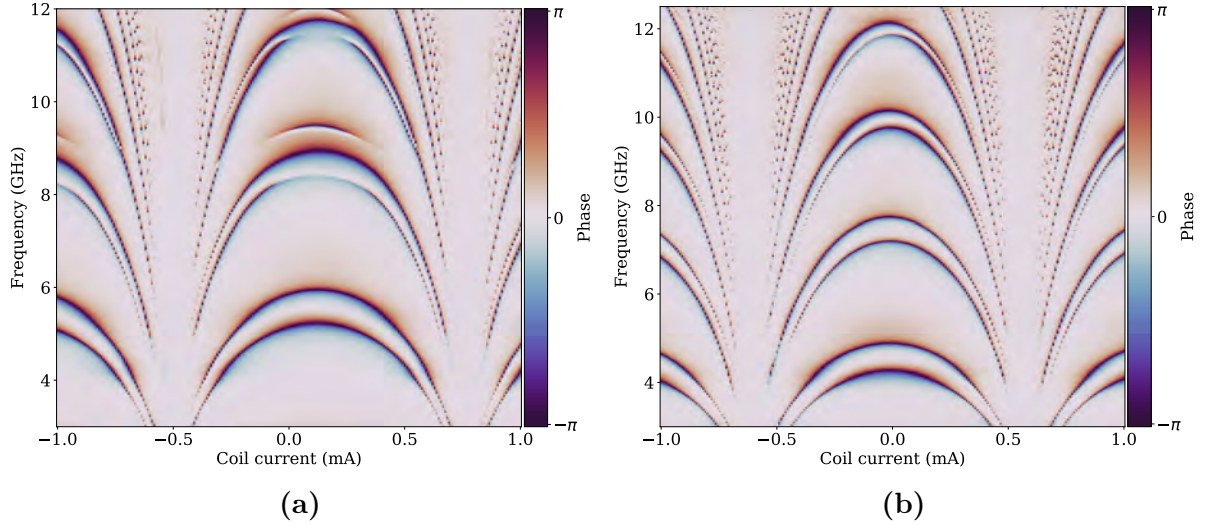


**Figure 5.1.1: Flux maps.** The phase response of (a) *DJAA1* and (b) *DJAA2* as already introduced in the previous chapter. Apart from further differences in the maps, discussed in details in the main text, the number of modes within the same frequency range is proportional to the number of SQUIDs in the device ( $N = 1400$  in (a) and  $N = 1700$  in (b)).

## 5.1.2 Amplification tunability

Once the resonance frequencies are inferred from the maps, we can look into the limits of the devices in terms of amplification tunability. The final goal would be to engineer the device such that the tunable ranges of consecutive dimers overlap with each other making the amplifier smoothly tunable across several gigahertz range.

The gain is obtained when a coherent pump tone is applied between the two resonance modes within one dimer. The power gain is deduced from the reflection coefficients taken with two VNA measurements: a main measurement with the pump on and a calibration measurement with the pump off and the amplifier detuned with the coil usually around the full frustration point, namely  $G(\omega) = |S_{11,on}|^2 / |S_{11,off}(I_{coil,cal})|^2$ . The power 2 comes from the definition of the scattering matrix which uses voltage instead of power. If the amplifier is not detuned, its resonances would appear as artificial gain after the normalization due to their slightly lossy properties.

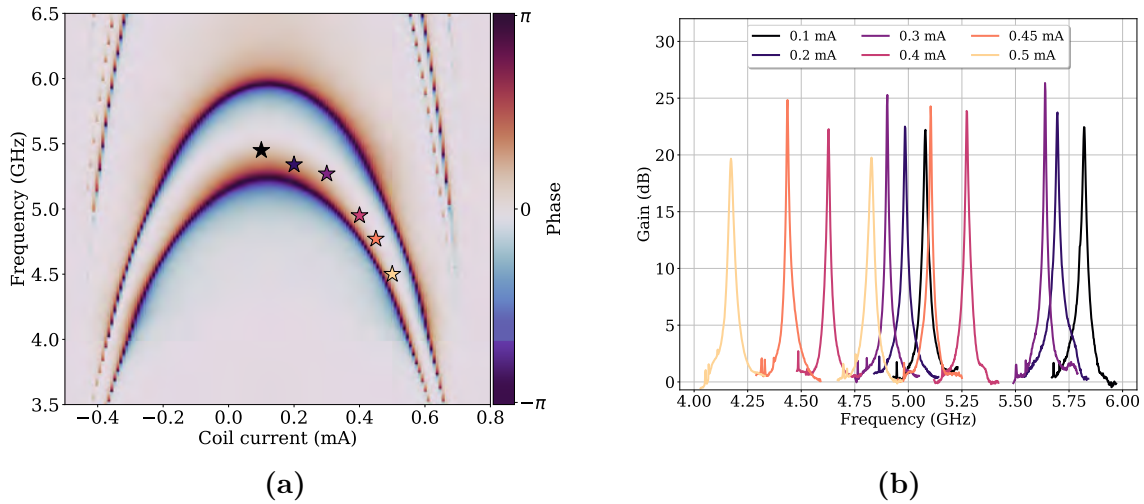


**Figure 5.1.2: DJJAA1: Flux tunability.** (a) Zoom-in of the flux map from Fig. 5.1.1a on the first dimer. The markers are placed at the frequency of pump tones used to achieve the gain response from (b) where the colors are matched. A total tunability of 1.6 GHz can be extracted.

For six different bias points in *DJJAA1*, we find pump parameters which give us a gain of approximately 20 dB as illustrated in Fig. 5.1.2. For each point, two Lorentzian shaped profiles emerge symmetrically around the respective pump frequency corresponding to the two modes from the dimer. The amplification appears without interruption in the region [4.2, 5.8] GHz, i.e. a total flux tunability of 1.6 GHz for the first dimer in *DJJAA1*. This value can be boosted by a few hundred MHz by fine tuning the pump parameters and the coil current. In general, the pump power at the output of the generator, required to achieve 20 dB gain, reduces with the mode frequencies, mainly because of the lower line attenuation at lower frequencies (see Fig. 4.3.2).

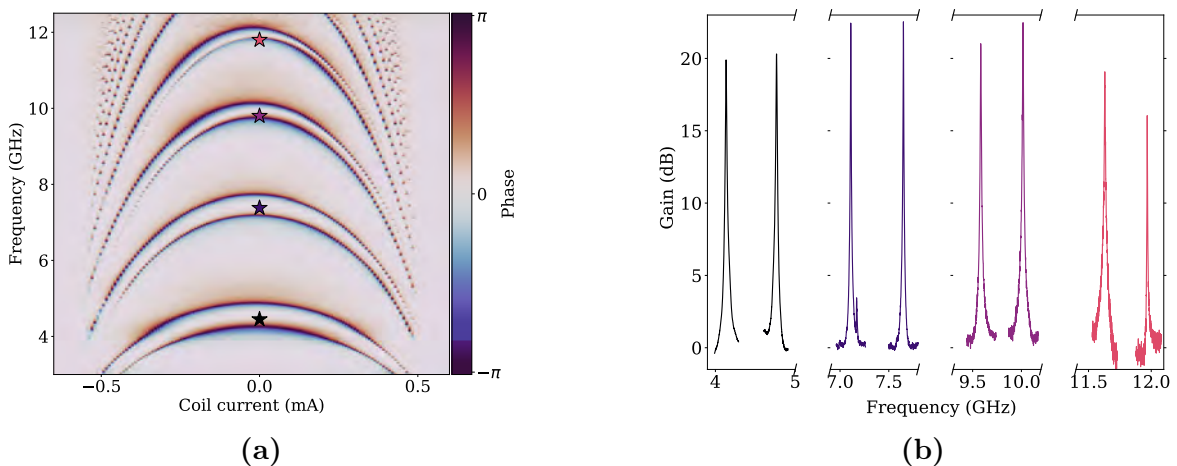


**Figure 5.1.3: DJJAA2: Gain at the sweet spot of different dimers.** The markers in the flux map (a) denote the frequency of the pump tone and the flux point used to achieve the response of (b). Their colors are matched. The power of the pump used to achieve the presented gain in the last dimer has been adjusted in order to obtain comparable amplification in both modes.

Another dimension we can exploit to achieve amplification at the desired frequency is the presence of several dimers. We show in Fig. 5.1.3 that a 20 dB gain is obtainable in all dimers of *DJAA2*. For the fourth dimer, the pump frequency was constant but two different powers were used to obtain the presented gain response. Since the higher mode in the fourth dimer appears almost at the edge of the working range of several used microwave devices, it needs higher power to overcome the losses and achieve the same gain.

## 5.2 Gain map

It can be observed in Fig. 5.1.2 and 5.1.3 that the pump frequency is detuned from the mean of the resonances. In fact, such a dynamical system is not straightforward to control because as the pump power is increased, the resonances shift to lower frequencies due to their self- and cross-Kerr non-linearity (as explained in Section 2.4) requiring adjustment of the pump frequency as well. The optimal pump parameters for amplification at a chosen frequency are such that maximum gain is achieved for minimum pump power.

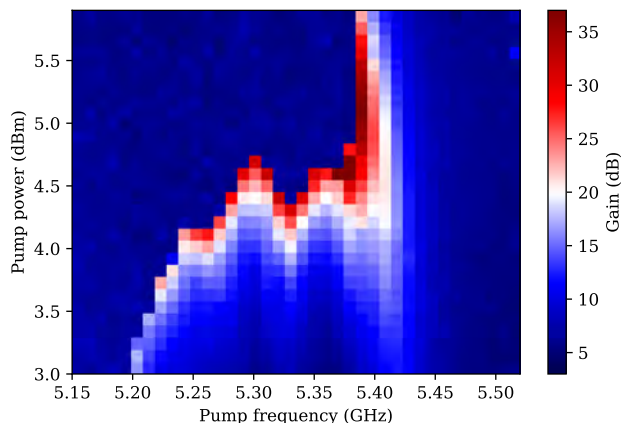


**Figure 5.2.1: DJAA1: Non-degenerate gain map at  $I_{coil} = 0$  mA.** The maximum non-degenerate gain is color-coded over a grid of the pump frequency and power. The colormap is chosen in a way to emphasize the range with achievable 20 dB with the white color.

An especially useful tool to find the optimal pump parameters is creating a gain map as the one in Fig. 5.2.1. In order to create this map for a single flux-bias point ( $I_{coil} = 0$  mA),  $S_{11}$  was measured with the pump frequency being fixed while the power was increased in steps of 0.1 dBm. Then the pump frequency was shifted by 10 MHz and the procedure was repeated. Each measurement with the pump on was followed by a calibration measurement in the same way. Then the highest point on either the left or right of the pump was extracted and its value was plotted in the map. Similar maps of the maxima positions can be found in App. F. To discover the overall optimal pump parameters for each frequency different flux points need to be investigated.

This map unveils the vast horizon of pump parameters which can achieve 20 dB gain. Several phases are distinguishable: stable for low powers in the range [5.29, 5.38] GHz where there is virtually no gain (barely visible in dark blue color), parametrically unstable

showing moderate to high gain in the light-blue ( $\gtrsim 10$  dB), white ( $\sim 20$  dB) and red ( $\lesssim 25$  dB) colored areas, and one-mode unstable in the noisy region below 5.38 GHz, where the maxima extracted from the spectra come from noise spikes, not from the gain profiles. These regimes are explained in details in Subsection 2.3.1. In fact, if we include the degenerate gain as well, we would acquire a similar phase diagram as in the Bose-Hubbard model (Fig. 2.3.3).

## 5.3 Gain-Bandwidth Product

It is a well-known fact that for amplifiers based on resonant circuits the bandwidth  $B$  decreases as the maximal power gain  $G_0$  (the amplitude of the Lorentzian gain profile in linear scale) grows, imposing a trade-off condition between the two:

$$\sqrt{G_0}B \underset{\gamma \rightarrow 0}{\approx} \kappa \quad (5.3.1)$$

Here  $\kappa$  is the external coupling rate and  $\gamma$  is the loss rate of the mode of interest.

Generally, the coupling rates vary between different resonances. Moreover, in the DJJAA or in other non-degenerate amplifier employing two modes, the effective coupling  $\bar{\kappa}_k$  is set by the decay rates of both modes [19, 61]

$$\bar{\kappa}_k = \frac{2\kappa_{k,1}\kappa_{k,2}}{\kappa_{k,1} + \kappa_{k,2}} \quad (5.3.2)$$

where  $\kappa_{k,m}$  are the rates at which lower ( $m = 1$ ) and higher ( $m = 2$ ) modes from the  $k$ -th dimer decay into the port. They can be extracted from the low power reflection measurements used for creating the flux maps in Fig. 5.1.1.

In order to measure the gain-bandwidth product, the device response is recorded while applying the pump with constant frequency and increasing power. The VNA measurements are calibrated in the usual manner used in this chapter. An example for the resulting gain profiles can be seen in Fig. 5.3.1a. The data is fitted with Lorentzian curves so one can extract the gain and the bandwidth, which we use to obtain the plot in Fig. 5.3.1b. For this figure the DJJAA1 was flux-biased at  $I_{coil} = 0.1$  mA, the plots in Fig. 5.3.1c and 5.3.1d are similarly attained when the amplifier is biased at 0 and 0.2 mA, respectively.

Although not presented here, previously produced samples[19] show that in general  $\kappa_{k,2} > \kappa_{k,1}$  which is evident also in every plot here since the gain-bandwidth product of the higher mode is superior to the one of mode 1. Moreover, the coupling rates reduce away from the sweet spot which would explain the fact that the greatest gain-bandwidth achieved on average corresponds to  $I_{coil} = 0.1$  mA which is the nearest to the sweet spot. Overall, the gain-bandwidth product is comparable but lower than the one extracted for similar devices of the type[19, 20, 62].

This limitation is one of the disadvantages of resonant parametric amplifiers. A way to enhance this product would be either to decrease the kinetic inductance of the SQUIDs or to increase the external coupling, which in both cases would result in higher bandwidths. Although there are clever ways like impedance engineering[63] to overcome this limitation, in transmission amplifiers[17] this constraint does not exist.

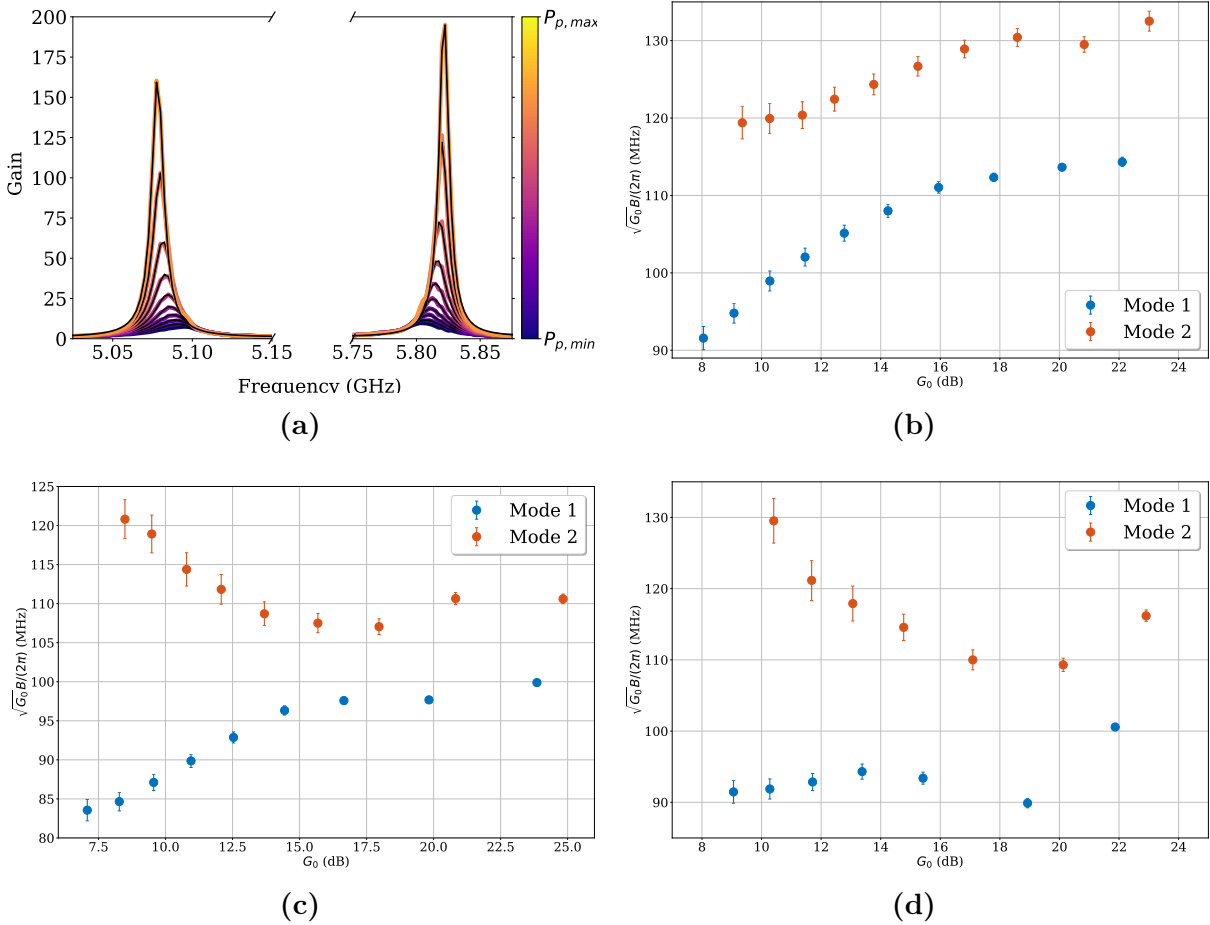


**Figure 5.3.1: DJJAA1: Gain-bandwidth product for three flux-bias points:** (a) and (b)  $I_{coil} = 0.1$  mA,  $f_p = 5.45$  GHz; (c)  $I_{coil} = 0$  mA,  $f_p = 5.32$  GHz and (d)  $I_{coil} = 0.2$  mA,  $f_p = 5.34$  GHz. In (a) the gain profiles are plotted in different colors depending on the pump strength. The gain and bandwidth for each curve are extracted from their Lorentzian fits (black) and then used to calculate the gain-bandwidth product as shown in (b) as a function of the maximum gain in decibels.

## 5.4 1-dB compression point

As already mentioned, the 1-dB compression point is the signal power at which the maximum gain reduces by 1 dB. There are two suspects for the origin of this phenomena: pump depletion and signal-induced frequency shift in the resonator. Usually since the pump tone is stronger than the signal one, we use the so-called stiff pump approximation in all derivations. However, this approximation is valid only when the signal is weak enough so it can be amplified without depleting the pump because of the photon conversion. Above a certain signal threshold, the pump cannot sustain the same conversion rates resulting in reduction of the gain.

The second mechanism responsible for the saturation is due to the inherent nonlinearity of the system. We already know that the self-Kerr coefficient makes the mode frequency dependant on its photon population. Therefore, if the signal is strong enough to populate the mode significantly, that would change the optimal pump conditions causing a decline in the gain.

In order to measure the saturation point of the three flux-bias points in *DJJAA1*, the pump strength and frequency were kept constant for each of them while the signal power was increased. Because of the high deviation from the set value in the digital attenuator, the signal power was only varied via the VNA while the digital attenuator was fixed, hence the few data points in Fig. 5.4.1. Each gain response was fitted with a Lorentzian curve in order to extract the amplitude  $G_0$ .

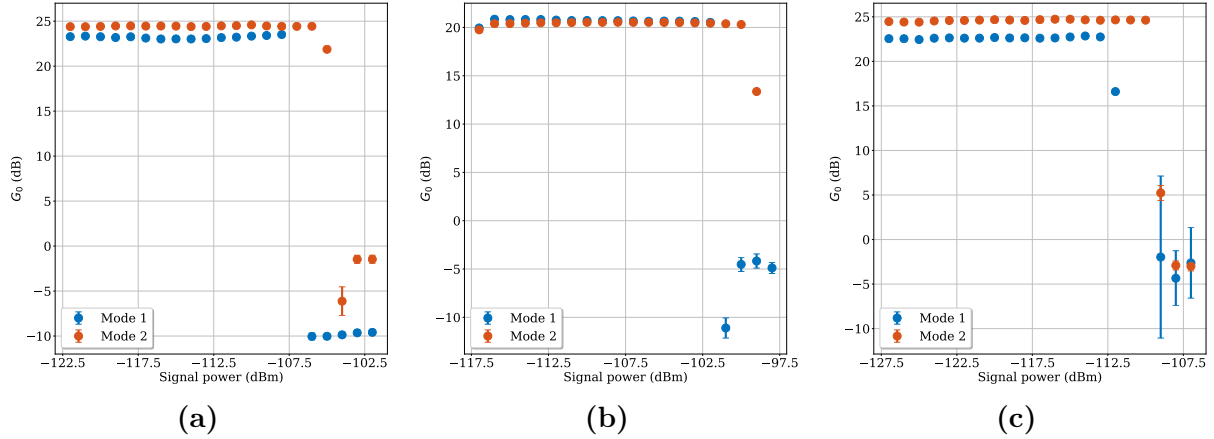


**Figure 5.4.1: DJJAA1: Saturation power.** (a)  $I_{coil} = 0$  mA,  $f_p = 5.32$  GHz,  $P_p = 4.25$  dBm; (b)  $I_{coil} = 0.1$  mA,  $f_p = 5.45$  GHz,  $P_p = 5$  dBm and (c)  $I_{coil} = 0.2$  mA,  $f_p = 5.34$  GHz,  $P_p = 4.75$  dBm. The maximum gain is plotted as a function of the signal power reaching the amplifier as previously calibrated (Fig. 4.3.2). The collapse of the gain is not well understood.

In all plots a similar behaviour can be observed, namely instead of gradually reducing, the gain drops abruptly. The negative values come from finite losses which are fitted automatically in the code. Since the saturation is an effect resulting from the overall population in the mode, it appears at higher signal powers for lower gains, which could justify the higher 1-dB compression point in Fig. 5.4.1b, compared to the others. However, to be conclusive further examination of the saturation power for a different gain at the same flux bias point is required. In spite of the similar gains in Fig. 5.4.1a and 5.4.1c, the drop for  $I_{coil} = 0.2$  mA appears at lower signal powers, which could be due to flux noise from the coil causing the resonances to shift away, rendering the pump parameters inefficient. The amplifier can be safely used without running into problems up to  $[-113 \pm 2, -102 \pm 2]$  dBm depending on the flux bias point, with the error coming from the additional attenuation between the amplifier and the switch, not included in the calibration from Fig. 4.3.2.

Although observed in other devices of the same type[19], the origin of the collapsing gain remains unresolved. If we refer to the gain map from Fig. 5.2.1 we can see that for most pump frequencies, the gain increases proportionally to the pump power until it suddenly disappears. Due to this sharp transition to the chaotic regime (multiple solutions), the saturation point is not well defined. Only from  $f_p \geq 5.39$  GHz once the maximum is reached, the gain smoothly diminishes, and we could expect to find a clear 1-dB compression point. However, the amplification with these pump parameters was not investigated.

## 5.5 Noise performance

The main reason for the wide usage of parametric amplifiers is their noise performance. While there are many ways to characterize this property, here we present two of them, namely noise visibility ratio (NVR) and input added photon number which was already mentioned earlier.

### 5.5.1 Noise visibility ratio

The noise visibility ratio (NVR) of a device is defined as the noise power in a spectrum analyzer at room temperature when the device is on versus off without any input signal applied. In our experiment, when the paramp is turned off, the noise spectrum is dominated by the HEMT. Once we apply the pump to the DJJAA, the noise incident on its input is amplified, overcoming the noise from the following amplification stages on the chain. By the definition the NVR can be quantified as

$$\Delta P = \frac{G_{DJJAA}T_{N,DJJAA} + T_{N,chain}}{T_{N,chain}}. \quad (5.5.1)$$

where we have employed Eq. 4.2.5 for multistage amplification chain and kept the notation the same.

The data for the NVR is taken by the spectrum analyser in parallel to the VNA measurements used to determine the gain-bandwidth product. Needless to mention, the VNA is off while the power spectrum is measured. The resulting spectra in linear scale (shown in logarithmic scale in Fig. 5.5.1a) are fitted as Lorentzian profiles and their maxima is plotted as a function of the gain in Fig. 5.5.1b for  $I_{coil} = 0.1$  mA, 5.5.1c and 5.5.1d flux-biased at 0 and 0.2 mA, respectively. If the gain is divided by the NVR (in linear scale), one could estimate the amount by which the SNR can be improved when the paramp is on.

For the three pairs of flux parameters yielding gain close to 20 dB (marked by diamonds in Fig. 5.5.1) we infer the added photon number. Combined with the noise temperature of the system without DJJAA extracted from the data in Fig. 4.3.1, the extracted added photon numbers are:  $\{2.14(1.45), 1.81(0.47)\}$  for  $I_{coil} = 0.1$  mA,  $\{2.38(1.1), 1.68(0.5)\}$  for  $I_{coil} = 0$  mA, and  $\{2.52(0.93), 1.87(0.49)\}$  for  $I_{coil} = 0.2$  mA where the first value always corresponds to the lower mode in the dimer. Consistently, the lower frequency mode is noisier than the higher. The values for all flux bias points overlap within the margin of error.

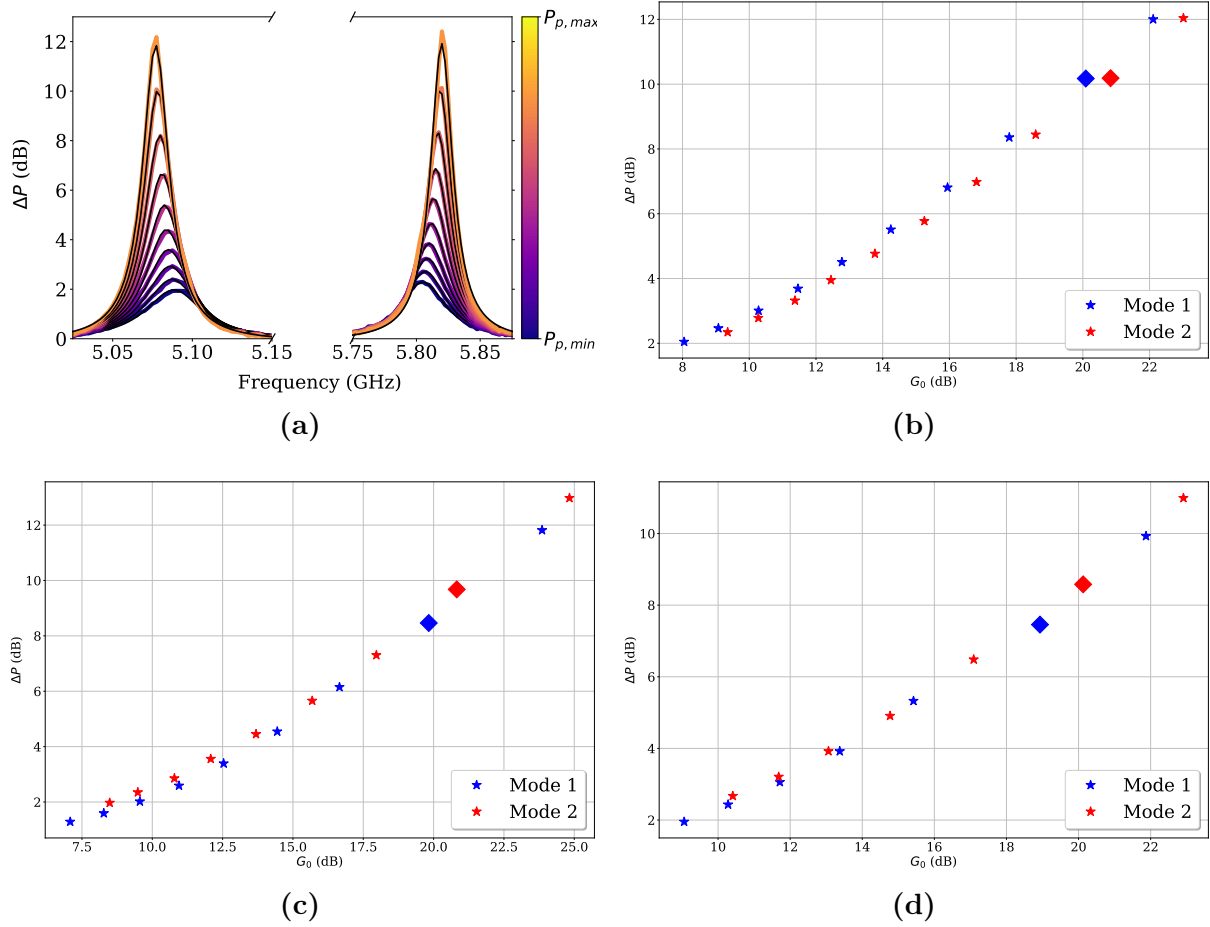


**Figure 5.5.1: DJJAA1: Noise rise:** (a) and (b)  $I_{coil} = 0.1$  mA,  $f_p = 5.45$  GHz; (c)  $I_{coil} = 0$  mA,  $f_p = 5.32$  GHz and (d)  $I_{coil} = 0.2$  mA,  $f_p = 5.34$  GHz. The normalized noise rise (a) is fitted with Lorentzian curves to extract the amplitude, plotted versus the respective gain in (b). The diamond-shaped points are further processed in the main text to extract their respective added noise numbers.

## 5.5.2 Added photon number

Although noise rise is a convenient and easy method to determine the noise performance of a device, it characterizes only the added noise at one point. While it can be expanded to include a bigger frequency range, with this method it is harder to consider deviations in the gain of the involved amplifiers. Instead, if we measure the input added noise, we can always directly calculate the SNR for any given input signal.

In order to do that, we implement another method which includes a set of four different measurements: PSD and  $S_{11}$  measurements with the parametric amplifier on and PSD and  $S_{11}$  measurements with the parametric amplifier off and flux-detuned to the point of full frustration. An example for such a raw data set can be found in Fig. 5.5.2. Additionally, the PSD with the hot load incident on the switch  $S_m(f, T_h)$  is taken and later used together with the aforementioned PSD measurement with the DJJAA off  $S_m(f, T_l)$  to characterize the amplification chain, assuming the amplifier and attenuators are all well thermalized.

Referring back to Eq. 4.2.5, with the additional PSD of the hot load we have

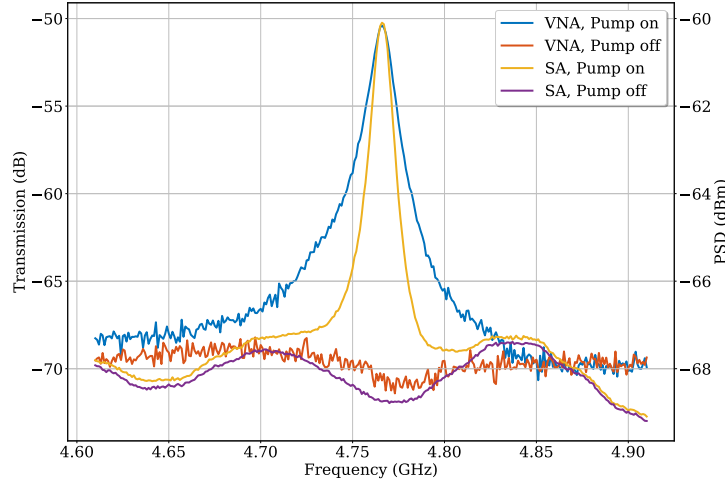


**Figure 5.5.2: Raw data for noise measurements.** As mentioned in the main text, four different measurements are taken (two with the VNA and two with the SA) for each mode in order to extract the added noise number within the amplification bandwidth. The additional PSD measurement of the hot load is not included in this plot.

calibrated the gain of the chain  $G_{chain}$ . Then from the VNA measurements the parametric amplifier gain  $G_{DJJAA}$  is extracted. Afterwards we eliminate the noise contribution from the chain  $k_B T_{N,chain}$  by subtracting the two noise power densities with the DJJAA on and off, leaving the noise spectral density from the parametric amplifier  $k_B T_{N,DJJAA}$  as the only unknown parameter. We previously made clear that the classical definition of the noise temperature is not well adapted for quantum objects. Therefore, to convert the result to photon number, we divide the PSD by  $hf$ , yielding the added photon number as a function of frequency. The averaging is done manually by repeating the procedure and taking the mean of the photon number at the end.

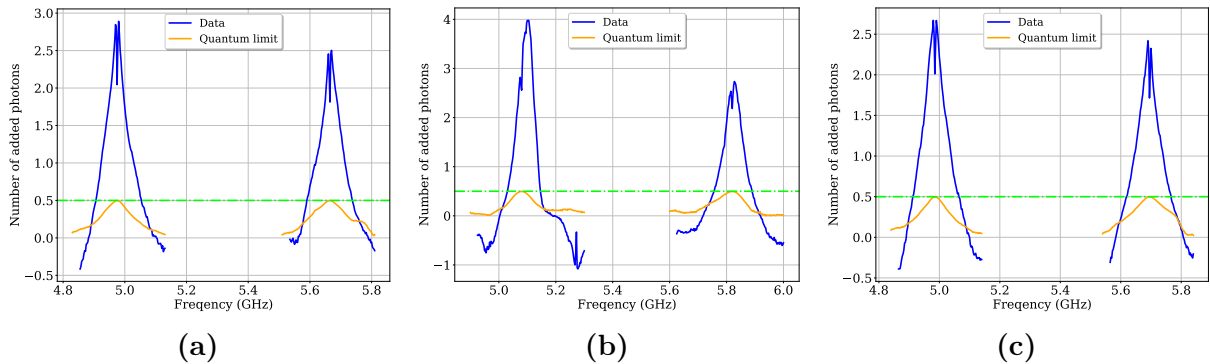


**Figure 5.5.3: DJJAA1: Added photon number at different flux-bias points:** (a)  $I_{coil} = 0$  mA,  $f_p = 5.32$  GHz,  $P_p = 4.25$  dBm; (b)  $I_{coil} = 0.1$  mA,  $f_p = 5.45$  GHz,  $P_p = 5$  dBm and (c)  $I_{coil} = 0.2$  mA,  $f_p = 5.34$  GHz,  $P_p = 4.75$  dBm. The added photon number is plotted against the frequency, together with the quantum limit expected for the measured gain. The green horizontal line marks the level of half a photon, which is the quantum limit for high gain.

For the same flux-bias points in *DJJAA1* the added photon number is extracted and plotted in Fig. 5.5.3. The expected quantum limit for the measured DJJAA gain is also shown after utilizing Eq. 2.1.7. In general, these results are higher than the values

inferred in the previous section. However, here the standard deviations are usually below 0.5 photons over the shown ranges. Within the margin of error, the results from both techniques overlap. We observe higher added photon number in the lower-frequency mode, which is consistent with the results from the NVR method.

Occasionally, the added photon number goes below zero. The source of this unphysical effect is the high sensitivity of this method: even a difference of 0.1 dBm in the background PSD could account for  $\pm 0.5$  added photons, with the sign depending on the sign of the deviation. Since outside of the band of our paramp the SNR is considerably smaller, any small change in the background, stemming from changes in the gain or saturation of the amplification chain, heating effects, etc., will be reflected on the results.

Furthermore, the same procedure is executed for the sweet spots in all *DJAA2* dimers in the range [3.5, 12.5] GHz and the results are presented in a similar manner in Fig. 5.5.4. Although missing in this figure, the last dimer was also studied and a similar plot presenting its noise properties can be found in Appendix F. In general, this amplifier seems to outperform *DJAA1* regarding added noise. Moreover, the two modes within one dimer are far more symmetric. Despite nearly doubling the averages, the signal-to-noise ratio deteriorates at higher frequencies because of the increasing line attenuation. However, the SNR is sufficient to determine that the added noise diminishes at higher dimer numbers.

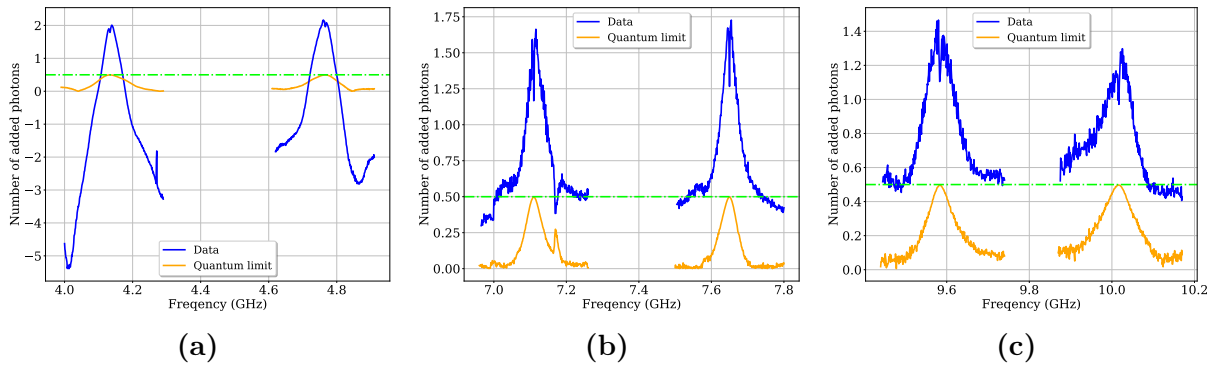


**Figure 5.5.4: DJAA2: Added photon number at the sweet spots of different dimers:** (a) dimer 1,  $f_p = 4.45$  GHz,  $P_p = 3.7$  dBm; (b) dimer 2,  $f_p = 7.38$  GHz,  $P_p = 7.8$  dBm, and (c) dimer 3,  $f_p = 9.8$  GHz,  $P_p = 8.1$  dBm. The added photon number and the quantum limit expected for the measured gain are plotted as a function of the frequency. The green horizontal line emphasises the level of half a photon. Due to the increasing attenuation, the signal becomes noisier at higher frequencies. In (b) the extra peak in the quantum limit results from improper gain calibration, which in turn causes the dip in the added photon number at that frequency.

## 5.6 Pump cancellation

The need for pump cancellation becomes evident in Fig. 5.5.4a, where the number reaches below  $-5$  added photons. This cannot be explained by fluctuations in the background. Another fundamental process takes place, namely saturation of an amplifier in the chain by the strong pump tone. If we send a copy of the pump tone out of phase with the one used for the signal amplification and combine them on the output of the paramp, a destructive interference takes place which would either completely or partially cancel the

strong pump, avoiding the saturation of the following amplification stages. For this reason we place an additional directional coupler where the coupled port is used for pumping the amplifier.

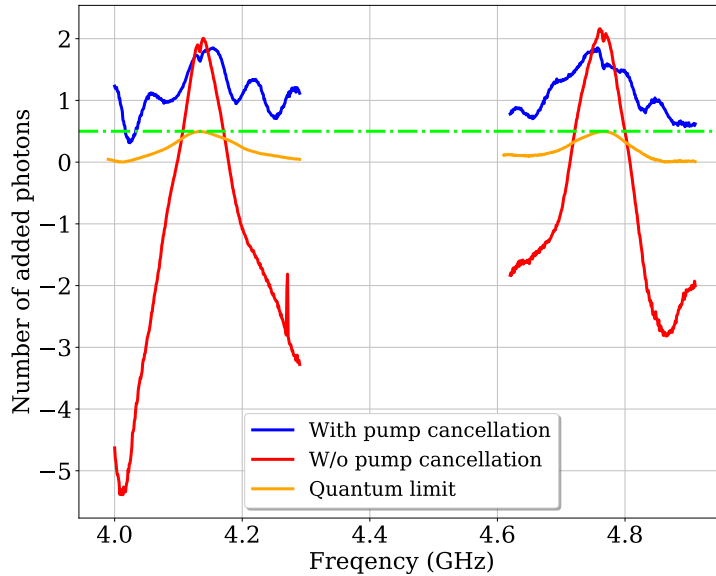


**Figure 5.6.1: DJJAA2: Comparison of the added photon number of the first dimer with and without pump cancellation.** Due to saturation in an amplifier in the chain, the added photon number becomes negative without taking care of the pump. If, on the other hand, the pump is partially cancelled, the photon number doesn't drop below zero. The quantum limit and the level of half a photon (green) are also presented.

Because of the nature of the attenuation, the amplifiers on the chain are easier to saturate at lower frequencies, explaining why the negative photon number is more visible in the first dimer. Therefore, we implemented the pump cancellation only for this dimer with the results shown in Fig. 5.6.1, together with the expected quantum limit. It is clear that suppressing the pump tone which reaches the amplifiers in the chain improves the quality of these measurements eliminating the unphysical negative values. Furthermore, both modes show decreased maximum number of added photons compared to the case without pump cancellation.

Due to the highly non-linear system we deal with, the phase shift and the attenuation on the pump cancellation tone need to be optimized for each pump power and frequency in order to achieve highest pump suppression for these particular pump parameters. This fact, combined with the time-consuming measurements of the added photon number, lead to the decision to only show the working principles of the scheme for the first dimer.

## 5.7 Attenuator heating

However, another effect takes place, which is also observed in Fig. 5.5.4b and 5.5.4c manifesting itself in the positive offset from zero outside the amplification bandwidth. Due to the high pump powers the attenuators on the main line connected to the coupled port of the directional coupler start emitting thermal radiation, thus raising the overall background when the pump is on. The thermal noise coming from the pump cancellation

line is further attenuated by the directional coupler inside the fridge, making it negligible compared to the contribution from the main line.

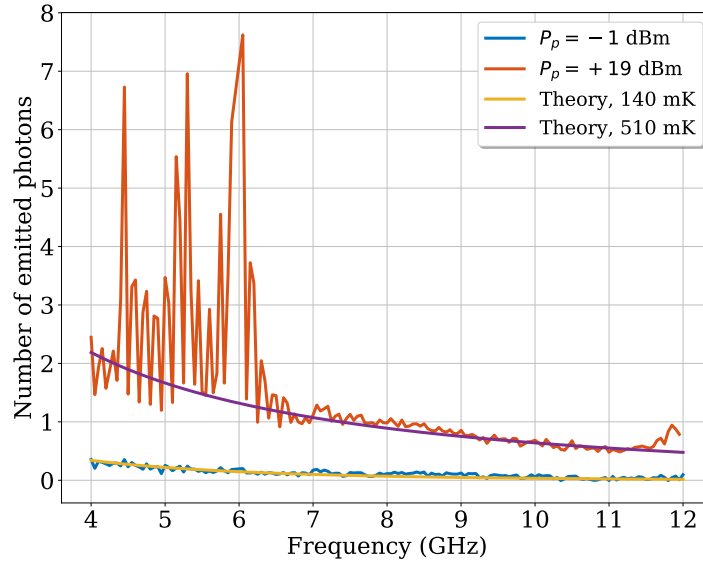


**Figure 5.7.1: Heating effects.** Purely thermal radiation as a function of the frequency is illustrated for two pump powers  $P_p = -1$  dBm and  $P_p = 19$  dBm at the microwave source output, while the frequency is constant  $f_p = 6$  GHz. Theoretical expectations respectively for  $T = 140$  mK and  $T = 510$  mK highly agree with the presented data. The noise around the pump frequency probably originates from the microwave generator.

To further investigate this effect, we connect the auxiliary input line without any sample on it and detect the noise power with the spectrum analyser while varying the pump power applied. The pump frequency is fixed at  $f_p = 6$  GHz. The power spectral densities we normalize by subtracting the background with the pump off leaving just the excess thermal radiation and no quantum contribution. The results for two pump powers are plotted in Fig. 5.7.1. The points in the close vicinity of the pump are removed for clarity. The noise around the pump frequency at the higher power trace comes probably from spurious modes from the microwave generator but this hypothesis wasn't confirmed by moving the pump to other frequencies.

In the plot one can see that a 20 dB difference in the pump power corresponds to already between half and two photons emitted by the attenuators on the line which translates in a 370 mK increase in temperature, according to the theoretical expectations, also plotted in Fig. 5.7.1. This effect degrades the overall signal-to-noise ratio. We see it mainly outside the amplification band in the higher background level. A possible solution would be implementing better matched and better thermalized attenuators[64].



# Chapter 6

## Conclusions and outlook

The main objective of this thesis was to fabricate and characterize low-noise, high-gain parametric amplifiers with high effective bandwidth which would greatly increase the signal-to-noise ratio in the existing experimental setups. These amplifiers, based on long dispersion-engineered Josephson junction arrays, were fabricated utilizing photolithography technology and, similarly to other devices of the same type[20, 19], they exhibit both degenerate and non-degenerate gain depending on the pump tone frequency.

In the first part, a recipe for in-house fabrication was developed from scratch. With the newly installed laser writer, a double-layer process was established for reliable fabrication of Josephson junctions. The basic recipe consists of several steps: optical lithography, aluminum film deposition, in situ argon milling and static oxidation. It has been shown that under the calibrated parameters, the native aluminum oxide layer is completely removed after three minutes forming a metallic contact between the two evaporated layers. The evaporation parameters were varied to determine the power-law dependence of the critical current density, a crucial parameter for the resonance frequencies of the circuit. Finally, the junction aging process was monitored over the span of more than three weeks, demonstrating age suppression approximately after a week with the amount of aging strongly depending on the junction size.

The biggest part of the fabrication was spent on combating problems, rather than the calibrations. The main issue that emerged regularly was inferior adhesion of the resist to the substrate. A precaution was taken to decelerate aging by changing the resist storage. Additional oxygen plasma cleaning step was incorporated before the first layer lithography, but this helped only temporarily. The final solution appeared to be an adhesion promoter which enforced changing almost all previously calibrated steps. Due to time concerns, the final devices were fabricated in KIT. However, repeating the process with the original recipe once the clean room dehumidifier is exchanged would be an interesting test to determine whether humidity was the sole reason behind these problems. Yet, if the sticking problems persist, changing the lithography to e.g. bilayer process, or switching completely to electron beam lithography would be the way to proceed.

Additionally, two of the fabricated devices were assembled and their non-degenerate operation was thoroughly tested. The high tunable range of the devices was demonstrated by obtaining gain exceeding 20 dB at four different dimers in *DJJA2*. Moreover, a 1.6 GHz flux tunability of the first dimer in *DJJA1* was deduced while keeping a moderate bandwidth of approximately 10 MHz. By exploiting the flux tunability of several dimers, if their tunable ranges overlap, the DJJAA frequency working range can be boosted to a value which successfully competes with any state-of-the-art transmission

parametric amplifier[14, 16]. The clear phase response of all dimers in *DJJAA2* makes it a good candidate to achieve tunability of several gigahertz. Similar devices based on resonant circuits covering almost the whole range 4 – 12 GHz have already been developed[65].

Finally, the noise performance of both amplifiers is comprehensively analyzed in two ways. On average, the maximum added noise in the first dimer of *DJJAA1* is 2.8 per unit bandwidth, with the lower frequency more being always noisier than the higher one. In *DJJAA2* we show that the noise reduces at higher dimer numbers and generally showing better noise performance than *DJJAA1* with up to 2.5 the quantum limit. A pump cancellation scheme was implemented, successfully overcoming the saturation from the following amplification stages. Due to the constant offset in the added photon number, the background was also investigated showing that under the influence of the pump, the attenuators heat up, thus rising the background radiation.

In summary, the amplifier concept was successfully implemented. While the fabrication was challenging with the laser writer technology, the design is flexible allowing easy manipulation of the parameters yielding predictable and reproducible results. An improvement of the devices by making them smoothly flux-tunable is possible if asymmetric SQUIDs are employed instead. Other changes like increasing the number of SQUIDs would be beneficial for the total working range of the device but would also inevitably complicate the fabrication. Some corrections in the PCB and the sample box design could diminish spurious modes to which the amplifier couples. As a last remark, the pump cancellation is easy and powerful technique to overcome the limitations of the measuring architecture. It revealed that great care needs to be taken to eliminate or reduce the heating effects which could influence also surrounding experiments in the fridge. Employing better thermalized attenuators could considerably improve the experimental setup.

# Bibliography

- [1] Richard P. Feynman. Simulating physics with computers. *International Journal of Theoretical Physics*, 21(6):467–488, Jun 1982.
- [2] F. Arute, K. Arya, R. Babbush, D. Bacon, J. C. Bardin, R. Barends, R. Biswas, S. Boixo, and *et al.* Quantum supremacy using a programmable superconducting processor. *Nature*, 574(7779):505–510, Oct 2019.
- [3] R. Albert. *Multiplication of microwave photons via inelastic Cooper pair tunneling*. PhD thesis, Université Grenoble Alpes, Nov 2019.
- [4] G. Arnold, M. Wulf, S. Barzanjeh, E. S. Redchenko, A. Rueda, W. J. Hease, F. Hassani, and J. M. Fink. Converting microwave and telecom photons with a silicon photonic nanomechanical interface. *Nature Communications*, 11(1):4460, Sep 2020.
- [5] C. M. Caves. Quantum limits on noise in linear amplifiers. *Phys. Rev. D*, 26:1817–1839, Oct 1982.
- [6] C. Eichler. *Experimental characterization of quantum microwave radiation and its entanglement with a superconducting qubit*. PhD thesis, ETH Zurich, 2013.
- [7] M. A. Castellanos-Beltran. *Development of a Josephson Parametric Amplifier for the Preparation and Detection of Non-classical States of Microwave Fields*. PhD thesis, University of Colorado, 2002.
- [8] M. A. Castellanos-Beltran and K. W. Lehnert. Widely tunable parametric amplifier based on a superconducting quantum interference device array resonator. *Applied Physics Letters*, 91(8):083509, Aug 2007.
- [9] M. A. Castellanos-Beltran, K. D. Irwin, G. C. Hilton, L. R. Vale, and K. W. Lehnert. Amplification and squeezing of quantum noise with a tunable Josephson metamaterial. *Nature Physics*, 4(12):929–931, Dec 2008.
- [10] N. Bergeal, F. Schackert, M. Metcalfe, R. Vijay, V. E. Manucharyan, L. Frunzio, D. E. Prober, R. J. Schoelkopf, S. M. Girvin, and M. H. Devoret. Phase-preserving amplification near the quantum limit with a Josephson ring modulator. *Nature*, 465(7294):64–68, May 2010.
- [11] R. Vijay, M. H. Devoret, and I. Siddiqi. Invited Review Article: The Josephson bifurcation amplifier. *Review of Scientific Instruments*, 80(11):111101, Nov 2009.
- [12] I. Siddiqi, R. Vijay, F. Pierre, C. M. Wilson, M. Metcalfe, C. Rigetti, L. Frunzio, and M. H. Devoret. Rf-driven josephson bifurcation amplifier for quantum measurement. *Phys. Rev. Lett.*, 93:207002, Nov 2004.

- 
- [13] B. E. A. Saleh and M. C. Teich. *Fundamentals of photonics; 2nd ed.* Wiley series in pure and applied optics. Wiley, New York, NY, 2007.
- [14] A. Miano and O. A. Mukhanov. Symmetric traveling wave parametric amplifier. *IEEE Transactions on Applied Superconductivity*, 29(5):1–6, 2019.
- [15] B. Ho Eom, P. K. Day, H. G. LeDuc, and J. Zmuidzinas. A wideband, low-noise superconducting amplifier with high dynamic range. *Nature Physics*, 8(8):623–627, Aug 2012.
- [16] L. Planat, A. Ranadive, R. Dassonneville, J. Puertas Martínez, S. Léger, C. Naud, O. Buisson, W. Hasch-Guichard, D. M. Basko, and N. Roch. Photonic-crystal josephson traveling-wave parametric amplifier. *Phys. Rev. X*, 10:021021, Apr 2020.
- [17] C. Macklin, K. O’Brien, D. Hover, M. E. Schwartz, V. Bolkhovskiy, X. Zhang, W. D. Oliver, and I. Siddiqi. A near-quantum-limited Josephson traveling-wave parametric amplifier. *Science*, 350(6258):307–310, 2015.
- [18] P. Winkel, I. Takmakov, D. Rieger, L. Planat, W. Hasch-Guichard, L. Grünhaupt, N. Maleeva, F. Foroughi, F. Henriques, K. Borisov, J. Ferrero, A. V. Ustinov, W. Wernsdorfer, N. Roch, and I. M. Pop. Nondegenerate parametric amplifiers based on dispersion-engineered josephson-junction arrays. *Phys. Rev. Applied*, 13:024015, Feb 2020.
- [19] P. Winkel. *Superconducting quantum circuits for hybrid architectures*. PhD thesis, Karlsruhe Institute of Technologies, 2020.
- [20] C. Eichler, Y. Salathe, J. Mlynek, S. Schmidt, and A. Wallraff. Quantum-limited amplification and entanglement in coupled nonlinear resonators. *Phys. Rev. Lett.*, 113:110502, Sep 2014.
- [21] K. Sliwa. *Improving the quality of Heisenberg back-action of qubit measurements made with parametric amplifiers*. PhD thesis, Yale University, 2016.
- [22] E. Tholén. *Intermodulation in microresonators for microwave amplification and nanoscale surface analysis*. PhD thesis, KTH, 2009.
- [23] A. Roy and M. Devoret. Introduction to parametric amplification of quantum signals with Josephson circuits. *Comptes Rendus Physique*, 17(7):740 – 755, 2016.
- [24] A. Roy and M. Devoret. Quantum-limited parametric amplification with josephson circuits in the regime of pump depletion. *Phys. Rev. B*, 98:045405, Jul 2018.
- [25] D. F. Walls and G. J. Milburn. *Quantum optics*. Springer-Verlag Berlin ; New York, springer study ed. edition, 1995.
- [26] B. Yurke, P.G. Kaminsky, R.E. Miller, E. Whittaker, A.D. Smith, A. Silver, and R. Simon. Observation of 4.2 k equilibrium noise squeezing via a josephson-parametric amplifier. *Magnetics, IEEE Transactions on*, 25:1371 – 1375, Apr 1989.
- [27] J. Bardeen, L. N. Cooper, and J. R. Schrieffer. Theory of superconductivity. *Phys. Rev.*, 108:1175–1204, Dec 1957.

- [28] M. H. Devoret. Quantum fluctuations in electrical circuits. In S. Reynaud, S. Giacobino, and J. Zinn-Justin, editors, *Quantum Fluctuations: Les Houches Session LXIII, June 27 - July 28, 1995*, chapter 10, pages 351–386. Elsevier, Amsterdam, 1997.
- [29] B.D. Josephson. Possible new effects in superconductive tunnelling. *Physics Letters*, 1(7):251 – 253, 1962.
- [30] U. Vool and M. Devoret. Introduction to quantum electromagnetic circuits. *International Journal of Circuit Theory and Applications*, 45(7):897–934, 2017.
- [31] A. Blais, A. L. Grimsmo, S. M. Girvin, and A. Wallraff. Circuit quantum electrodynamics. *arXiv e-prints (arXiv:2005.12667)*, May 2020.
- [32] M. D. Hutchings, J. B. Hertzberg, Y. Liu, N. T. Bronn, G. A. Keefe, Markus Brink, Jerry M. Chow, and B. L. T. Plourde. Tunable superconducting qubits with flux-independent coherence. *Phys. Rev. Applied*, 8:044003, Oct 2017.
- [33] J. Braumüller, L. Ding, A. P. Vepsäläinen, Y. Sung, M. Kjaergaard, T. Menke, R. Winik, D. Kim, B. M. Niedzielski, A. Melville, J. L. Yoder, C. F. Hirjibehedin, T. P. Orlando, S. Gustavsson, and W. D. Oliver. Characterizing and optimizing qubit coherence based on squid geometry. *Phys. Rev. Applied*, 13:054079, May 2020.
- [34] S. Boutin, D. M. Toyli, A. V. Venkatramani, A. W. Eddins, I. Siddiqi, and A. Blais. Effect of higher-order nonlinearities on amplification and squeezing in josephson parametric amplifiers. *Phys. Rev. Applied*, 8:054030, Nov 2017.
- [35] P. Krantz, M. Kjaergaard, F. Yan, T. P. Orlando, S. Gustavsson, and W. D. Oliver. A quantum engineer’s guide to superconducting qubits. *Applied Physics Reviews*, 6(2):021318, 2019.
- [36] C. W. Gardiner and M. J. Collett. Input and output in damped quantum systems: Quantum stochastic differential equations and the master equation. *Phys. Rev. A*, 31:3761–3774, Jun 1985.
- [37] B. Yurke and E. Buks. Performance of cavity-parametric amplifiers, employing kerr nonlinearities, in the presence of two-photon loss. *J. Lightwave Technol.*, 24(12):5054–5066, Dec 2006.
- [38] C. W. Gardiner and P. Zoller. *Quantum Noise - A Handbook of Markovian and Non-Markovian Quantum Stochastic Methods with Applications to Quantum Optics*. Springer, second edition, 2000.
- [39] D. Sarchi, I. Carusotto, M. Wouters, and V. Savona. Coherent dynamics and parametric instabilities of microcavity polaritons in double-well systems. *Phys. Rev. B*, 77:125324, Mar 2008.
- [40] Michael Tinkham. *Introduction to Superconductivity*. Dover Publications, 2 edition, Jun 2004.

- [41] N. Maleeva, L. Grünhaupt, T. Klein, F. Levy-Bertrand, O. Dupre, M. Calvo, F. Valenti, P. Winkel, F. Friedrich, W. Wernsdorfer, A. V. Ustinov, H. Rotzinger, A. Monfardini, M. V. Fistul, and I. M. Pop. Circuit quantum electrodynamics of granular aluminum resonators. *Nature Communications*, 9(1):3889, Sep 2018.
- [42] Yu. Krupko, V. D. Nguyen, T. Weißl, É. Dumur, J. Puertas, R. Dassonneville, C. Naud, F. W. J. Hekking, D. M. Basko, O. Buisson, N. Roch, and W. Hasch-Guichard. Kerr nonlinearity in a superconducting josephson metamaterial. *Phys. Rev. B*, 98:094516, Sep 2018.
- [43] T. Weißl, B. Küng, E. Dumur, A. K. Feofanov, I. Matei, C. Naud, O. Buisson, F. W. J. Hekking, and W. Guichard. Kerr coefficients of plasma resonances in josephson junction chains. *Phys. Rev. B*, 92:104508, Sep 2015.
- [44] P. R. Muppalla, O. Gargiulo, S. I. Mirzaei, B. Prasanna Venkatesh, M. L. Juan, L. Grünhaupt, I. M. Pop, and G. Kirchmair. Bistability in a mesoscopic josephson junction array resonator. *Phys. Rev. B*, 97:024518, Jan 2018.
- [45] P. R. Muppalla. *Josephson junction array resonators in the Mesoscopic regime: Design, Characterization and Application*. PhD thesis, University of Innsbruck, 2020.
- [46] N. A. Masluk, I. M. Pop, A. Kamal, Z. K. Mineev, and M. H. Devoret. Microwave characterization of josephson junction arrays: Implementing a low loss superinductance. *Phys. Rev. Lett.*, 109:137002, Sep 2012.
- [47] L. Planat, R. Dassonneville, J. P. Martínez, F. Foroughi, O. Buisson, W. Hasch-Guichard, C. Naud, R. Vijay, K. Murch, and N. Roch. Understanding the saturation power of josephson parametric amplifiers made from squid arrays. *Phys. Rev. Applied*, 11:034014, Mar 2019.
- [48] T. Yamamoto, K. Inomata, M. Watanabe, K. Matsuba, T. Miyazaki, W. D. Oliver, Y. Nakamura, and J. S. Tsai. Flux-driven Josephson parametric amplifier. *Applied Physics Letters*, 93(4):042510, Jul 2008.
- [49] T.J. Rinke, C. Koch, and MicroChemicals GmbH. *Photolithography: Basics of Microstructuring*. MicroChemicals, 2017.
- [50] Allresist. *Positive Photoresist for Lift-off AR-P 5300*, Jan 2018.
- [51] M. Madou. *Fundamentals of Microfabrication*. Boca Raton: CRC Press, 2007.
- [52] L. Grünhaupt, U. von Lüpke, D. Gusenkova, S. T. Skacel, N. Maleeva, S. Schlör, A. Bilmes, H. Rotzinger, A. V. Ustinov, M. Weides, and I. M. Pop. An argon ion beam milling process for native  $\text{AlO}_x$  layers enabling coherent superconducting contacts. *Applied Physics Letters*, 111(7):072601, Aug 2017.
- [53] J. M. Kreikebaum, K. P. O'Brien, A. Morvan, and I. Siddiqi. Improving wafer-scale josephson junction resistance variation in superconducting quantum coherent circuits. *Superconductor Science and Technology*, 33(6):06LT02, May 2020.
- [54] V. Ambegaokar and A. Baratoff. Tunneling between superconductors. *Phys. Rev. Lett.*, 10:486–489, Jun 1963.

- [55] S. Fritz, L. Radtke, R. Schneider, M. Luysberg, M. Weides, and D. Gerthsen. Structural and nanochemical properties of  $\text{AlO}_x$  layers in  $\text{Al}/\text{AlO}_x/\text{Al}$ -layer systems for Josephson junctions. *Phys. Rev. Materials*, 3:114805, Nov 2019.
- [56] A. W. Kleinsasser, R. E. Miller, and W. H. Mallison. Dependence of critical current density on oxygen exposure in  $\text{Nb}/\text{AlO}_x/\text{Nb}$  tunnel junctions. *IEEE Transactions on Applied Superconductivity*, 5(1):26–30, 1995.
- [57] I. M. Pop, T. Fournier, T. Crozes, F. Lecocq, I. Matei, B. Pannetier, O. Buisson, and W. Guichard. Fabrication of stable and reproducible submicron tunnel junctions. *Journal of Vacuum Science & Technology B, Nanotechnology and Microelectronics: Materials, Processing, Measurement, and Phenomena*, 30(1):010607, Jan 2012.
- [58] David M Pozar. *Microwave Engineering 3e*. Wiley, 2006.
- [59] Low Noise Factory. *LNF-LNC4\_16B s/n 1456Z 4-16 GHz Cryogenic Low Noise Amplifier*, Aug 2019.
- [60] Agile Microwave Technology Inc. *AMT-A0067 4 GHz to 12 GHz Broadband Low Noise Amplifier*, rev a edition.
- [61] A. A. Clerk, M. H. Devoret, S. M. Girvin, F. Marquardt, and R. J. Schoelkopf. Introduction to quantum noise, measurement, and amplification. *Rev. Mod. Phys.*, 82:1155–1208, Apr 2010.
- [62] I. Takmakov. Josephson parametric dimer based on quarter wavelength microstrip squid array resonators. Master’s thesis, Moscow State University, 2017.
- [63] T. Roy, S. Kundu, M. Chand, A. M. Vadiraj, A. Ranadive, N. Nehra, M. P. Patankar, J. Aumentado, A. A. Clerk, and R. Vijay. Broadband parametric amplification with impedance engineering: Beyond the gain-bandwidth product. *Applied Physics Letters*, 107(26):262601, Dec 2015.
- [64] J.-H. Yeh, Y. Huang, R. Zhang, S Premaratne, J. LeFebvre, F. C. Wellstood, and B. S. Palmer. Hot electron heatsinks for microwave attenuators below 100 mk. *Applied Physics Letters*, 114(15):152602, Apr 2019.
- [65] V. V. Sivak, S. Shankar, G. Liu, J. Aumentado, and M. H. Devoret. Josephson array-mode parametric amplifier. *Phys. Rev. Applied*, 13:024014, Feb 2020.
- [66] U. Vool. *Engineering Synthetic Quantum Operations*. PhD thesis, Yale University, 2017.
- [67] Allresist. *AR 300-80 new and HMDS adhesion promoter*, May 2019.
- [68] Allresist. *AR 300-26 and AR 300-35 buffered developers*, Oct 2019.
- [69] C. Tannous and J. Langlois. Classical noise, quantum noise and secure communication. *European Journal of Physics*, 37(1):013001, Nov 2015.
- [70] Y. Yamamoto. *Fundamentals of Noise Processes*. Cambridge University Press, Feb 2004.



# Appendix A

## Method of nodes

In this chapter, a recipe for finding the degrees of freedom (DOFs) in an electric circuit is presented. Electric elements arranged in a specific manner form the topology of the circuits and together with the external initial conditions outline the boundary conditions of the problem to be solved. Whether the electric network elements are linear or non-linear would determine the intricacy of finding the DOFs. The task starts with deriving the classical Lagrangian or Hamiltonian, diagonalizing one of them in order to find the independent eigenstates and promoting those to quantum variables with imposing uncertainty conditions. As from now, we follow the treatment from [30, 66].

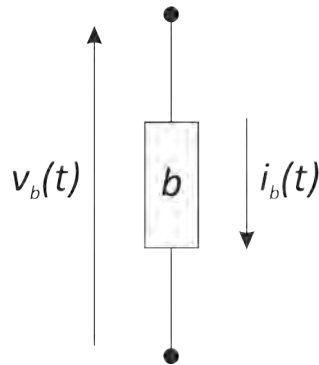


**Figure A.1.1: Branch and node representation.** Any dipolar circuit element can be replaced by a branch  $b$ . Each branch is surrounded by two nodes via which the connection to other branches is achieved. The sign convention of the voltage  $v_b(t)$  and current  $i_b(t)$  determine the sign of the power absorbed by the branch element (Eq. A.1.2). Figure adopted from [30].

We assume, without big loss in generality, that any electric circuit consists of dipolar elements, called branches  $b$ , and these elements are connected to each other via nodes as shown on Fig. A.1.1. Each branch is characterized by the voltage across it and the current flowing through it. They are connected to the underlying electromagnetic fields in the following way

$$v_b(t) = \int_{\text{start of } b}^{\text{end of } b} \vec{E}(\vec{x}, t) \cdot d\vec{l} \quad (\text{A.1.1a})$$

$$i_b(t) = \frac{1}{\mu_0} \oint_{\text{around } b} \vec{B}(\vec{x}, t) \cdot d\vec{l} \quad (\text{A.1.1b})$$

where  $\mu_0$  is the permeability of free space.

The path for the closed loop integral is in vacuum and encircling all field components. In the lumped-element approximation, which we are using, it is equivalent to integrating along a path surrounding the branch only since all fields are focused within the element. As a result, the current and voltage should not depend on the path taken for the integration, meaning the path for integration should not include components from other fields than the one in the integral.

The directions of the current and voltage vectors are chosen to be opposite, in order to define the energy absorbed by the element as a positive entity

$$E_b(t) = \int_{-\infty}^t v_b(t')i_b(t')dt' \quad (\text{A.1.2})$$

where the lower bound of the integral is set to a time sufficiently far in the past ( $-\infty$ ) when the system was at rest. Other common variables for describing the branch are flux and charge, obtained by integrating the voltage and current respectively

$$\Phi_b(t) = \int_{-\infty}^t v_b(t')dt' \quad (\text{A.1.3a})$$

$$Q_b(t) = \int_{-\infty}^t i_b(t')dt' \quad (\text{A.1.3b})$$

also considered as position and momentum coordinates in the nodes method.

By using Kirchhoff's first law, one can take into account external magnetic fields or electric biases

$$\sum_{\substack{\text{all } b \text{ joining} \\ \text{at node } n}} Q_b = Q_{ext}^n \quad (\text{A.1.4})$$

where  $Q_{ext}^n$  is the charge on node  $n$ . Generally, because of these conditions, the total number of independent DOFs is smaller than the branches composing the circuit. With this method we assign a flux coordinate to every node in the circuit. One can instead use the method of loops by assigning charges to the loops, and solve the problem via the second Kirchhoff's law. The final DOFs should be identical by converting to branch fluxes via

$$\Phi_b = \Phi_n - \Phi_{n'} \quad (\text{A.1.5})$$

for a branch  $b$  between nodes  $n$  and  $n'$ , where the direction determines the sign of the current.

We need to introduce some terminology for further use in this chapter. Let us define two specific groups of elements: capacitive and inductive. If the voltage across a branch  $v_b(t)$  is directly dependent only on the charge  $Q(t)$ , then this element is capacitive. On the other hand, if the current through the element  $i_b(t)$  is a function only of the flux  $\Phi(t)$ , then we call this unit inductive. The respective energies for the commonly used units in our setups are summarized in Table A.1.1. As of now, all nodes collecting branches of one type will be called *active*, while if the converging elements are mixed (capacitors and inductors) the nodes will be referred as *passive*. If we divide the system in two sub-networks of capacitances and inductances, we make sure that all nodes in the capacitive sub-network are passive, while in contrast the nodes in the inductive sub-network can be also active.

Element	Energy
Linear capacitor $C(Q) = C$	$\frac{Q^2}{2C}$
Linear inductor $L(\Phi) = L$	$\frac{\Phi^2}{2L}$
Josephson junction (Non-linear inductor) $L_J$	$-\frac{\phi_0^2}{L_J} \cos\left(\frac{\Phi}{\phi_0}\right)$

**Table A.1.1: Energies of the basic building blocks in circuit quantum electrodynamics.** The energies for a linear capacitor, linear inductor and Josephson junction are calculated from Eq. A.1.2. Constant offsets are excluded.

Proceeding with the task we choose the ground node with node flux zero from where the spanning tree is built. The ground node is always picked to be active. Notably, no matter what the choice for spanning tree is, the equations of motion will be the same despite the different energy expressions. However, as a rule of thumb, defining the tree only through capacitive sub-network simplifies the connection of the conjugate variable to the charge across the capacitors. At this moment, we are ready to build the capacitance and inverse inductance matrices with dimension  $(N \times N)$ , where the passive nodes are denoted with index 1 to  $P$  and the active nodes with  $P+1$  to  $N$ . For the inductance matrix  $\tilde{L}^{-1}$  all off-diagonal elements are  $-L_{ij}^{-1}$  corresponding to the inverse inductance connecting nodes  $i$  and  $j$ . If there is no inductance, which is the case for all passive nodes, these matrix elements are zero. The diagonal elements are the negated sum of all inductive contributions from the branches joining at this node.

The conductance matrix  $\tilde{C}$  is built in a similar way with the only difference that the off-diagonal elements are now  $-C_{ij}$ . We can now introduce a flux column vector  $\vec{\Phi}$  with components  $\Phi_i$ . The kinetic energy will be the sum of the contributions from all linear capacitive branches

$$E_{kin} = \sum_{\{i,j\}} \frac{C_{ij}}{2} (\Phi_i - \Phi_j)^2 \quad (\text{A.1.6})$$

while the potential energy is associated to all inductive branches

$$E_{pot} = \sum_{\{i,j\}} \frac{1}{2L_{ij}} (\Phi_i - \Phi_j)^2 \quad (\text{A.1.7})$$

where the sum runs through all branches. In the matrix representation, the Lagrangian can be written as

$$\mathcal{L} = E_{kin} - E_{pot} = \frac{1}{2} \dot{\vec{\Phi}}^T \tilde{\mathbf{C}} \dot{\vec{\Phi}} - \frac{1}{2} \vec{\Phi}^T \tilde{\mathbf{L}}^{-1} \vec{\Phi} \quad (\text{A.1.8})$$

where the matrices  $\tilde{\mathbf{C}}$  and  $\tilde{\mathbf{L}}^{-1}$  differ from the aforementioned capacitance and inverse inductance matrices in their dimension  $(N-1) \times (N-1)$  since the row and column corresponding to the ground node have been removed.

Finally, the equations of motion are found from the Euler-Lagrange equation

$$\frac{d}{dt} \frac{\partial \mathcal{L}}{\partial \dot{\Phi}_i} = \frac{\partial \mathcal{L}}{\partial \Phi_i} \quad (\text{A.1.9})$$

and the conjugate variable is the charge

$$Q_i = \frac{\partial \mathcal{L}}{\partial \dot{\Phi}_i} \quad (\text{A.1.10})$$

with the charge vector defined as  $\vec{Q} = \tilde{\mathbf{C}}\dot{\vec{\Phi}}$ . This treatment is universal as long as there are no loops in the circuit, otherwise the external fluxes need to be taken into account. It is important to mention that the offset charges on the nodes have been neglected for simplicity but they can influence immensely the circuit properties in the superconducting case.

For more insight, we look into two examples: the LC oscillator from Section 2.2 and a JJA with three junctions, depicted in Fig. 2.4.1. In the first case we have a node with flux  $\Phi$  and a ground reference node ( $\Phi = 0$ ). Therefore, we can directly derive the Lagrangian 2.2.3 with the help of Table A.1.1. The later example is more interesting, since it includes four nodes in total, with the boundary conditions  $\Phi_0 = \Phi_3 = 0$ . The Lagrangian in this case reads

$$\mathcal{L} = \frac{C_0}{2} (\dot{\Phi}_1^2 + \dot{\Phi}_2^2) + \frac{C_J}{2} \left[ \dot{\Phi}_1^2 + (\dot{\Phi}_2 - \dot{\Phi}_1)^2 + \dot{\Phi}_2^2 \right] - E_J [\cos(\phi_1) + \cos(\phi_2 - \phi_1) + \cos(\phi_2)] \quad (\text{A.1.11})$$

where we imposed the boundary conditions in the derivation. In the harmonic approximation (for small currents  $I \ll I_c$ ), we can approximate the non-linear element as a linear inductor  $E_J \cos(\phi_2 - \phi_1) \approx \frac{1}{2L_J}(\Phi_2 - \Phi_1)^2$  and write the Lagrangian in the matrix form from Eq. A.1.8 with the following matrices

$$\tilde{\mathbf{C}} = \begin{pmatrix} 2C_J + C_0 & -C_J \\ -C_J & 2C_J + C_0 \end{pmatrix} \quad (\text{A.1.12a})$$

$$\tilde{\mathbf{L}}^{-1} = \begin{pmatrix} \frac{2}{L_J} & -\frac{1}{L_J} \\ -\frac{1}{L_J} & \frac{2}{L_J} \end{pmatrix}. \quad (\text{A.1.12b})$$

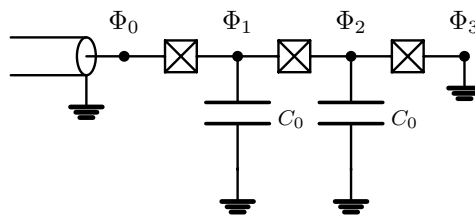


**Figure A.1.2: Josephson junction array with  $N = 3$ : Lumped-element representation.** Circuit diagram of a one-dimensional chain of three Josephson junctions coupled galvanically to a transmission line for controlling the system. The capacitance to ground  $C_0$  comes from the superconducting islands connecting the junctions.

# Appendix B

## Kerr coefficients

The self-Kerr  $K_{kk}$  and cross-Kerr coefficients in Eq. 2.4.11 and 2.4.17 can be extracted from the formula[42, 43]

$$K_{kl} = 2(2 - \delta_{kl}) \frac{\pi^4 \hbar E_J \eta_{kkl}}{\phi_0^4 C_J^2 \omega_k \omega_l}. \quad (\text{B.1.1})$$

where numerical factors  $\eta_{kkl}$  delineate wave function overlaps

$$\eta_{kkl} = C_J^2 \sum_{i=1}^N \left[ \left( \sum_{j=0}^N (\tilde{C}_{i,j}^{-1/2} - \tilde{C}_{i-1,j}^{-1/2}) \Psi_{j,k} \right)^2 \left( \sum_{j=0}^N (\tilde{C}_{i,j}^{-1/2} - \tilde{C}_{i-1,j}^{-1/2}) \Psi_{j,l} \right)^2 \right]. \quad (\text{B.1.2})$$

Here  $\Psi_{j,k}$  is the  $j$ -th element in the  $k$ -th eigenvector and  $\tilde{C}_{i,j}^{-1/2}$  is the entry at  $i$ -th row and  $j$ -th column in the matrix  $\tilde{C}^{-1/2}$ .

Note that, the capacitance matrices give rise to utterly different coefficients. To derive the Kerr coefficients for DJJAA, we use a symmetrized version of the flux eigenvectors. Otherwise, the jump experienced by the odd modes at the center causes numerical instabilities coming from the coefficients  $\eta_{kkl}$  from Eq. B.1.2.



# Appendix C

## Final recipes for DJJAA fabrication

<b>KIT</b>	
<b>Cleaning</b>	
No wet cleaning, blowing with nitrogen	
<b>Resist layer S1805</b>	
Spinning acceleration	500 rpm/s
Ramp	500 rpm for 5 s
Spinning speed	4500 rpm
Spinning time	60 s
Heat plate temperature	115 °C
Baking time	1 min
<b>Exposure</b>	
Dose	13 mW/cm <sup>2</sup>
Time	4 s
Wavelength	365 nm
Contact mode	hard
<b>Development MF-319: Layer 1</b>	
Time	30 s with swirling the liquid in the beaker
Stopping	distilled H <sub>2</sub> O, N <sub>2</sub> dry-blowing
<b>Development MF-319: Layer 2</b>	
Time	25 s less swirling the liquid in the beaker
Stopping	distilled H <sub>2</sub> O, N <sub>2</sub> dry-blowing

**Table C.1.1:** Two-layer photolithography process, optimized for DJJAA production on sapphire in the **KIT** clean room: Wafer preparation and lithography. Mask aligner *Karl Süss MA6* is used for the exposure. The difference in the development of the two layers comes from the *TMAH* in *MF-319* which etches *Al*.

<b>KIT</b>	
<b>Aluminium evaporation: Layer 1</b>	
Descum + Rot	$O_2/Ar$ (10/5) sccm, $V_{beam} = 200$ V, $I_{beam} = 10$ mA, $V_{acc} = 50$ V
Al evaporation + Rot	30 nm at rate 1 nm/s
<b>Lift-off</b>	
Solvent	NEP at 40 °C
Time	at least 2 hours
Ultrasonication	5 min at low power
Rinsing	Ethanol + $N_2$ dry-blowing
<b>Aluminium evaporation: Layer 2</b>	
$Ti$ gettering	2 min at rate 0.2 nm/s
Milling + Rot	$Ar$ (4 sccm), $t = 2$ min 30 s, $V_{beam} = 400$ V, $I_{beam} = 15$ mA, $V_{acc} = 40$ V
Static oxidation	$p = 10$ mbar, $t = 4 - 10$ min
Al evaporation + Rot	40 nm at rate 1 nm/s
<b>Silver backside metallization</b>	
Protection layer	Resist <i>S1818</i> Baking at 80 °C for 5 min Wiping the backside with acetone
$Ag$ deposition	Descum time 2 min 30 s $Ti$ gettering $Ti$ evaporation, 5 nm at 0.2 nm/s $Ag$ evaporation, 200 nm at 1 nm/s

**Table C.1.2:** Two-layer photolithography process, optimized for DJJAA production on sapphire in the **KIT** clean room: Metal deposition, lift-off and backside metallization.

<b>QNTZ</b>	
<b>Cleaning</b>	
Solvent cleaning	Ultrasonication in acetone, 1 min Isopropanol cleaning from the acetone Dry-blowing with nitrogen
RF plasma cleaning	$O_2$ (30 sccm), $p = 5$ Pa, $P = 100$ W, $t = 10$ min
<b>Adhesion promoter layer AR 300-80[67]</b>	
Spinning acceleration	1000 rpm/s
Spinning speed	4000 rpm
Spinning time	100 s
Heat plate temperature	105 °C
Baking time	2 min
Thermalization time	1 min 30 s
<b>Resist layer AR-P 5350</b>	
Preparation of resist	Taken out of the fridge ~ 30 min before exposure Stirred at 150 rpm until ~ 10 min before resist spinning
Spinning acceleration	1000 rpm/s
Spinning speed	4000 rpm
Spinning time	100 s
Heat plate temperature	105 °C
Baking time	4 min
<b>Exposure: Layer 1</b>	
Dose	60mJ/cm <sup>2</sup>
<b>Exposure: Layer 2</b>	
Dose	56mJ/cm <sup>2</sup>
<b>Development AR 300-35[68]</b>	
Dilution	1:2 with distilled $H_2O$
Time	1 min 5 s
Stopping	distilled $H_2O$ , several sequential beakers, $N_2$ dry-blowing

**Table C.1.3:** Two-layer photolithography process, optimized for DJJAA production on silicon in the QNTZ clean room: Wafer preparation and lithography.

<b>QNTZ</b>	
<b>Aluminium evaporation: Layer 1</b>	
Descum + Rot	$O_2/Ar$ (10/10 sccm), $V_{beam} = 200$ V, $I_{beam} = 10$ mA, $V_{acc} = 50$ V
<i>Ti</i> gettering	2 min at rate nm/s
<i>Al</i> evaporation + Rot	30 nm at rate 1 nm/s
<b>Lift-off</b>	
Solvent	Acetone at maximum 40 °C, several sequential beakers (room $t$ )
Time	minimum 2-3 hours
Ultrasonication*	$3 \times 30$ s in the different beakers at 135 kHz and 20% power
Rinsing	Isopropanol + $N_2$ dry-blowing
<b>Aluminium evaporation: Layer 2</b>	
<i>Ti</i> gettering	2 min at rate nm/s
Milling + Rot	$Ar$ (5 sccm), $t = 3$ min, $V_{beam} = 400$ V, $I_{beam} = 20$ mA, $V_{acc} = 80$ V
Static oxidation	$p = 30$ mbar, $t = 5$ min 30 s, $t_{rise} \approx 2$ min, $t_{fall} \approx 2$ min
<i>Al</i> evaporation + Rot	50 nm at rate 1 nm/s

**Table C.1.4:** Two-layer photolithography process, optimized for DJJAA production on silicon in the **QNTZ** clean room: Metal deposition of the first layer. The step marked with an asterisk (\*) applies only to the first layer.

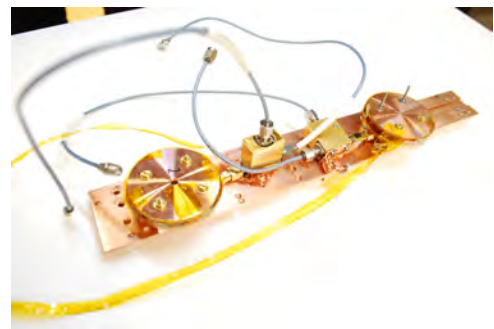
# Appendix D

## Setup details

The sample holder is produced out of copper because of its good thermal conductivity properties. A picture of the holder can be seen in Fig. D.1.1a. In the middle of the bottom part, there is a post where the PCB and the chip are glued and the former is also screwed to the holder. The dimensions of the inner cavity formed by the two halves are chosen in a way that all modes are outside of the measurement band. This design was also used for measurements of a bare transmission line, hence the two ports. Once the amplifiers are installed, everything from the full assembly (the sample box in Fig. D.1.3 and the coil body in Fig. D.1.4) is screwed to the T-beam through the four sides (Fig. D.1.1b). The T-beam, enclosed in a shielding can, is then mounted to the base plate of the refrigerator as shown in Fig. D.1.2.



(a)



(b)

**Figure D.1.1: Setup pictures.** (a) Sample holder, (b) *DJJAA1* and *DJJAA2* mounted on the T-beam.

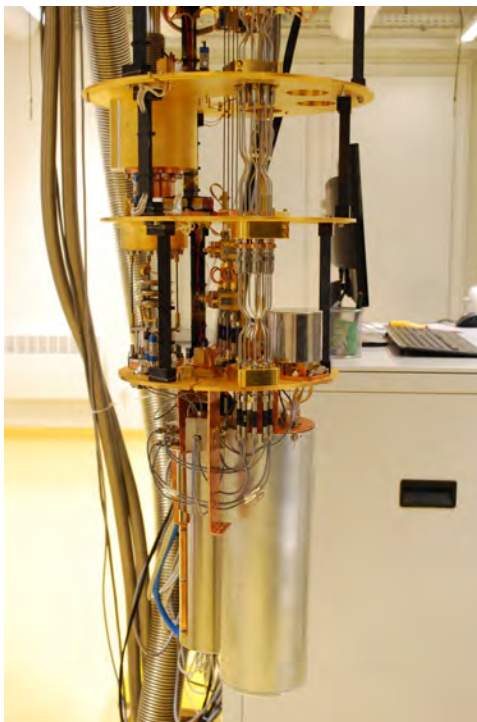
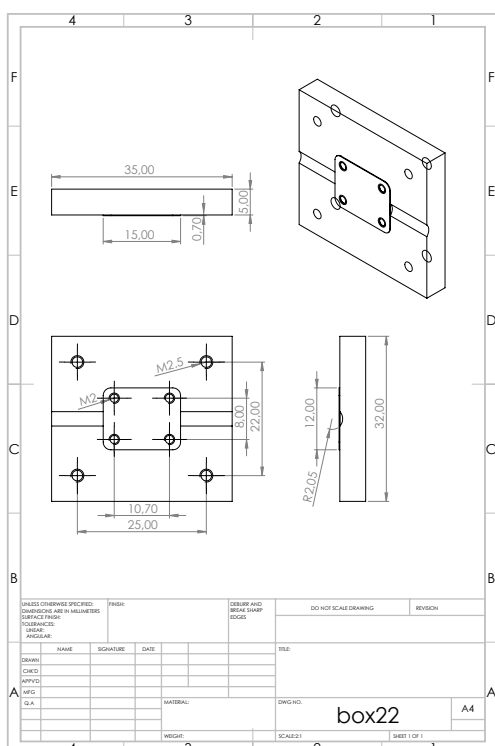
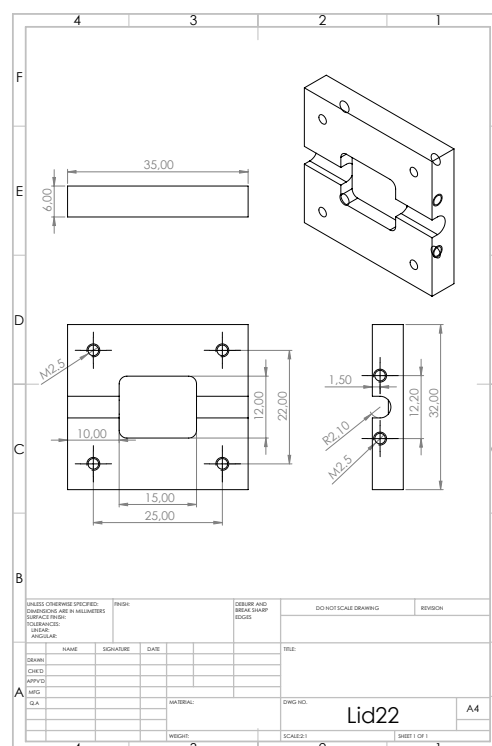


**Figure D.1.2: Dilution refrigerator.** Open dilution refrigerator with the samples installed in a shielding can attached to the base plate (silver-colored at the bottom).



(a)



(b)

**Figure D.1.3: SolidWorks drawing of the sample holder.** It includes the (a) lower and the (b) upper part of the sample holder. The dimensions are in mm.

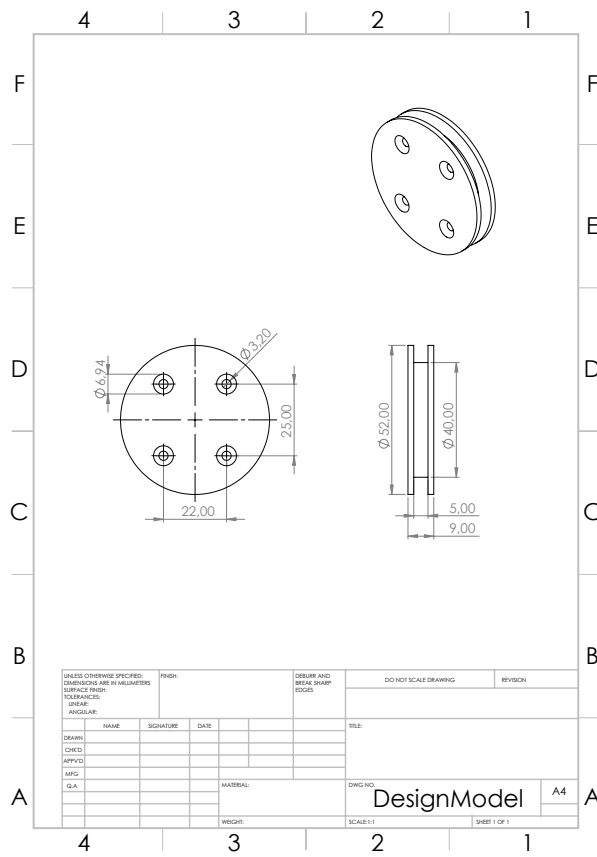


Figure D.1.4: *SolidWorks* drawing of the coil body. The dimensions are in mm.



# Appendix E

## Nyquist model: semi-infinite transmission line

This chapter is rewritten from [69]. Consider a lossless transmission line of length  $L$  with one open and one short termination. Introducing the capacitance  $c$  and inductance  $l$  per unit length, the Hamiltonian of the system can be written as

$$H(t) = \int_0^L \left( \frac{q^2(x,t)}{2c} + \frac{\phi^2(x,t)}{2l} \right) dx, \quad (\text{E.1.1})$$

where  $q(x,t)$  and  $\phi(x,t)$  represent the local charge and flux densities, respectively. If we make the variable change  $\theta(x,t) = \int_0^x q(x',t) dx'$ , the Hamiltonian can be rewritten in the following way

$$H(t) = \int_0^L \left[ \frac{1}{2c} \left( \frac{\partial \theta}{\partial x} \right)^2 + \frac{l}{2} \left( \frac{\partial \theta}{\partial t} \right)^2 \right] dx. \quad (\text{E.1.2})$$

Using Hamilton's equation of motion, we get a wave equation for  $\theta(x,t)$  with velocity  $v = 1/\sqrt{lc}$ . By imposing the boundary conditions  $\theta(0,t) = \theta(L,t) = 0$ , we solve the equation with the normal mode expansion, given by

$$\theta(x,t) = \sqrt{\frac{2}{L}} \sum_{n=1}^{\infty} b_n(t) \sin k_n x, \quad (\text{E.1.3})$$

with  $b_n$  being the mode amplitude and  $k_n = n\pi/L$  - the wavevector.

We jump directly to the second quantization of the system in order to obtain an expression for the voltage operator at the position of the short  $x = 0$ . We express the mode amplitude in terms of the creation and annihilation operators

$$\hat{b}_n(t) = \sqrt{\frac{\hbar c \omega_n}{2k_n^2}} (\hat{a}_n^\dagger(t) + \hat{a}_n(t)), \quad (\text{E.1.4})$$

where the frequency of the standing waves  $\omega_n = nv\pi/L$  has been introduced. Therefore, for the voltage we get the expression

$$\hat{V}(t) = \frac{1}{c} \frac{\partial \hat{\theta}(x,t)}{\partial x} \Big|_{x=0} = \sqrt{\frac{\hbar}{Lc}} \sum_{n=1}^{\infty} \sqrt{\omega_n} (e^{i\omega_n t} \hat{a}_n^\dagger(0) + e^{-i\omega_n t} \hat{a}_n^\dagger(0)). \quad (\text{E.1.5})$$

The spectral density is then obtained from the Fourier transform of the auto-correlation function of the voltage  $S_V(\omega) = \int_{-\infty}^{+\infty} e^{-i\omega\tau} \langle \hat{V}(t)\hat{V}(t+\tau) \rangle d\tau$ , giving the following equation

$$S_V(\omega) = \frac{2\pi}{Lc} \sum_{n=1}^{\infty} \hbar\omega_n [n(\omega_n)\delta(\omega + \omega_n) + (n(\omega_n) + 1)\delta(\omega - \omega_n)] \quad (\text{E.1.6})$$

where  $n(\omega) = \langle a_n^\dagger(0)a_n(0) \rangle = (e^{\hbar\omega/k_bT} - 1)^{-1}$  is the mean number of photons in a mode at energy  $\hbar\omega$  and temperature  $T$  governed by the Bose-Einstein distribution.

Taking the limit  $L \rightarrow \infty$  and converting the sum to an integral gives the final expression for the power spectral density of the voltage

$$S_V(\omega) = 2Z_c\hbar|\omega| \{n(|\omega|)\Theta(-\omega) + [n(|\omega|) + 1]\Theta(\omega)\}, \quad (\text{E.1.7})$$

where  $\Theta(\omega)$  is the Heaviside step function.

The asymmetry of the function in this quantum case is in contradiction to the classical counterpart. At negative frequencies, the resistor absorbs photons, while the positive frequency part is related to the stimulated ( $n(|\omega|)$  term) and spontaneous ( $+1$  term) emission from the element. Even at zero temperature, meaning  $n(|\omega|) = 0$ , the term responsible for spontaneous emission remains, meaning the vacuum can still absorb energy, a well known fact in quantum physics.

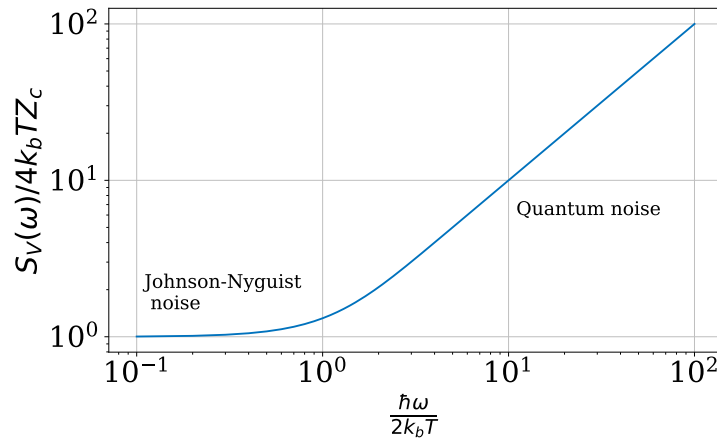


**Figure E.1.1: Generalized Nyquist noise.** The voltage noise spectrum of a semi-infinite transmission line including zero-point fluctuations reduces to the familiar classical Johnson-Nyquist noise or to quantum noise depending on the ratio  $\omega/T$ . Figure adopted from [70].

If we focus on the emission only, namely  $\omega > 0$ , we retrieve a more familiar equation

$$S_V(\omega) = \frac{2Z_c\hbar\omega}{1 - e^{-\hbar\omega/k_bT}}. \quad (\text{E.1.8})$$

Taking only the symmetric part of the voltage spectral density, we obtain an expression for the voltage spectral density from a purely dissipative element which we can measure

$$S_V(\omega) + S_V(-\omega) = 2Z_c\hbar\omega \coth \frac{\hbar\omega}{2k_bT}. \quad (\text{E.1.9})$$

---

Meanwhile, the asymmetric-in-frequency part of the noise is related to damping.

This equation, also known as generalized Nyquist noise, reduces to the classical Johnson-Nyquist noise  $S_V(\omega) = 4k_bT Z_c$  in the limit  $k_bT \gg \hbar\omega$ , or to the quantum noise  $S_V(\omega) = 2\hbar\omega Z_c$  in the low temperature limit  $k_bT \ll \hbar\omega$  as can be seen in Fig. E.1.1. Note that the classical noise can be directly measured while the quantum noise only manifests itself indirectly as e.g. photon shot noise. Finally, the conversion to power spectral density is executed by simply dividing the expressions by  $4Z_c$ .



# Appendix F

## Additional plots

### Flux tunability: magnitude response

Similarly to Fig. 5.1.1, from the same data we can extract the magnitude response of the amplifier as shown in Fig. F.1.1. Qualitatively, the information received from such a map is similar, but a feature missing in the phase response is the spurious coupling to the box mode around 4 GHz present in both amplifiers.

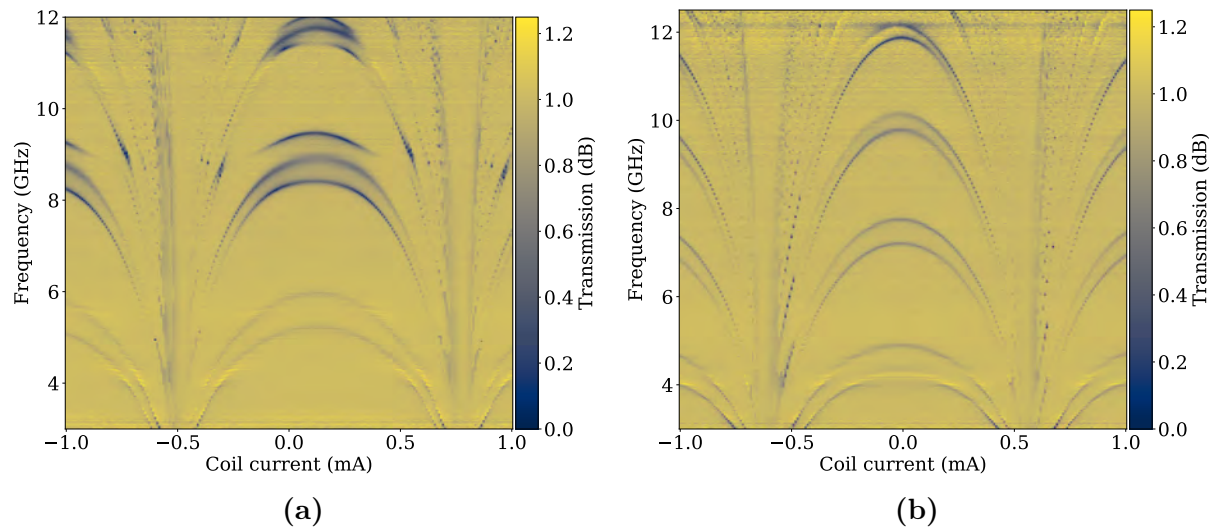


**Figure F.1.1: Flux maps in magnitude.** (a) *DJJAA1* with  $N = 1400$  and (b) *DJJAA2* with  $N = 1700$ .

### *DJJAA1*: Frequency maps for $I_{coil} = 0$ mA

From the data used for making the gain map in Fig. 5.2.1 we can also extract the frequencies where gain appears on both sides of the pump. The results are plotted in Fig. F.1.2. The effect we see is that in mode 1 (Fig. F.1.2a) the frequency where the gain appears decreases as the pump power is ramped up, while for mode 2 (Fig. F.1.2b) the frequency is proportional to the pump power. Meanwhile, the pump frequency has the same influence on both modes, meaning as we shift the pump frequency the gain frequencies follow in the same manner.

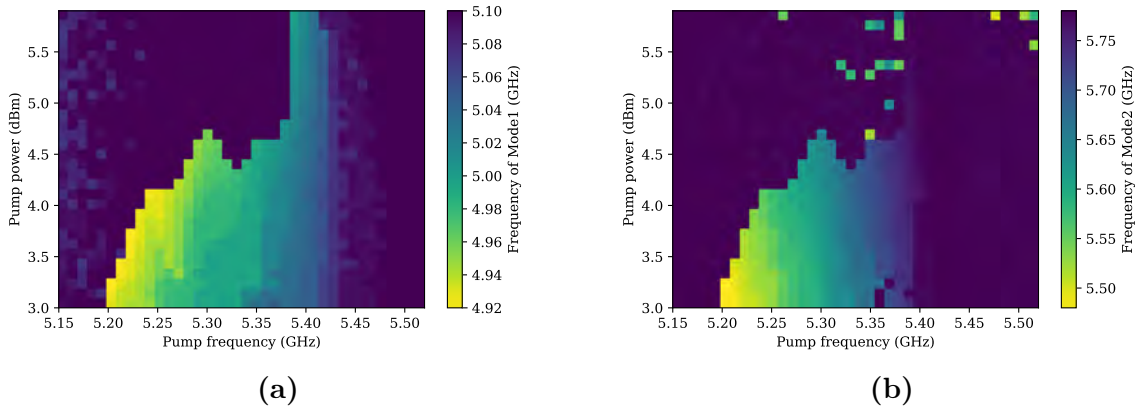


**Figure F.1.2: DJJAA1: Frequency maps of the gain for  $I_{coil} = 0$  mA.** The frequencies where non-degenerate gain appears as a function of the pump parameters. The two modes within the dimer are plotted separately in (a) the lower frequency mode and in (b) the higher frequency mode.

## *DJJAA2*: Noise performance of the fourth dimer

This dimer was the only one pumped with two different powers in order to achieve comparable gain in both modes. Because of the noisy results, the added photon number for the dimer 4 from *DJJAA2* is plotted in a semilogarithmic scale. The first contribution to the noise comes from the high attenuation at these frequencies, which are in close vicinity to the end of the working range of most microwave components, further enhancing this effect. Another reason for the noisy behavior of this dimer is the heating of the attenuators because of the strong pump as already discussed in Section 5.6.

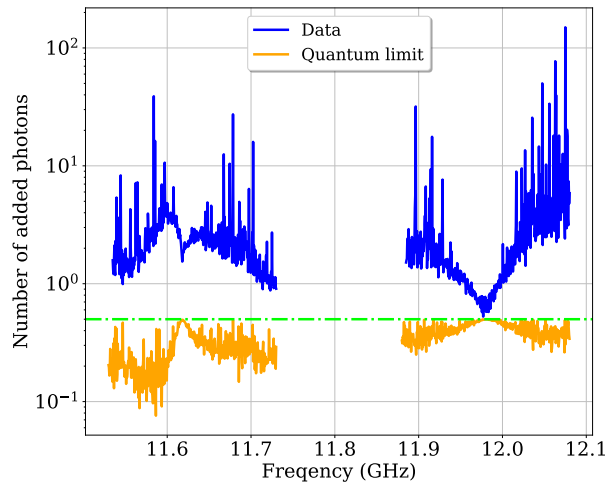


**Figure F.1.3: DJJAA2: Added photon number at the sweet spots of dimer 4.** The used pump parameters are  $f_p = 4.45$  GHz,  $P_{p,1} = 13.8$  dBm and  $P_{p,2} = 14.05$  dBm. The added photon number (blue) and the quantum limit (orange) expected for the measured gain are plotted as a function of the frequency. The green horizontal line emphasises the level of half a photon.